

IMAGING DOSES IN RADIATION THERAPY FROM
KILOVOLTAGE CONE-BEAM COMPUTED TOMOGRAPHY

By

DANIEL ELLIS HYER

A DISSERTATION PRESENTED TO THE GRADUATE SCHOOL
OF THE UNIVERSITY OF FLORIDA IN PARTIAL FULFILLMENT
OF THE REQUIREMENTS FOR THE DEGREE OF
DOCTOR OF PHILOSOPHY

UNIVERSITY OF FLORIDA

2010

© 2010 Daniel Ellis Hyer

To my family and loving fiancée – Mom, Dad, John and Laura

ACKNOWLEDGMENTS

First and foremost, I would like to thank my research advisor and the chair of my supervisory committee, David Hintenlang, for his advice and guidance during my graduate studies at the University of Florida. As my advisor, David played a large role in defining my research and was always able to offer ideas and suggestions; even at times when nothing seemed to be going right! Without his instruction and most importantly his friendship, my time as a graduate student would not have been nearly as enjoyable.

I would also like to thank each of the faculty members serving on my supervisory committee, including Wesley Bolch, Jonathan Li, and Hans van Oostrom. Their input and advice provided me with valuable guidance which helped keep my research focused and moving forward. I would also like to thank Chris Serago and Siyong Kim from Mayo Clinic in Jacksonville for the use of their equipment and working with me after hours to complete organ dose measurements. In addition, I would like to thank the staff in the Department of Nuclear and Radiological Engineering, for their help with everyday questions and concerns.

Finally, I would like to extend a special thanks to my family and friends. I would like to give thanks to my mom and dad for instilling in me the work ethic and values I needed to succeed in life. I would like to give thanks to my brother, John, for always believing in me and encouraging me in my academic endeavors. I would also like to give thanks to all of my fellow graduate student colleagues, especially Perry Johnson and Ryan Fisher, for being there when I needed advice or just wanted to hang out. Lastly, I want to thank Laura for her everlasting love, encouragement, and support.

TABLE OF CONTENTS

	<u>page</u>
ACKNOWLEDGMENTS	4
LIST OF TABLES	8
LIST OF FIGURES	9
ABSTRACT	11
CHAPTER	
1 INTRODUCTION	13
Cancer	13
Radiation Therapy	13
Need for Imaging in Radiation Therapy	16
Megavoltage Cone Beam Computed Tomography (MV-CBCT)	17
CT-on-Rails	17
Kilovoltage Cone Beam Computed Tomography (kV-CBCT)	18
Current State of Radiation Dosimetry in kV-CBCT	20
Objectives of this Research	28
2 CONSTRUCTION OF A 50 TH PERCENTILE ADULT MALE ANTHROPOMORPHIC PHANTOM.....	36
Introduction.....	36
Methods and Materials	38
Materials	38
Soft tissue-equivalent substitute (STES).....	39
Lung tissue-equivalent substitute (LTES).....	40
Bone tissue-equivalent substitute (BTES).....	40
Phantom Construction Methodology.....	41
Creating soft tissue molds	42
Introduction of soft tissue.....	43
Introduction of bone tissue.....	44
Phantom assembly.....	45
Introduction of lung tissue.....	45
Results.....	46
Materials	46
Soft tissue-equivalent substitute.....	46
Lung tissue-equivalent substitute	46
Bone tissue-equivalent substitute	46
Completed Phantom	46
Discussion.....	47
Conclusions.....	48

3	CONSTRUCTION AND CHARACTERIZATION OF A WATER-EQUIVALENT FIBER OPTIC COUPLED DOSIMETER FOR USE AT DIAGNOSTIC ENERGIES.....	54
	Introduction.....	54
	Methods and Materials	56
	FOC Dosimetry System.....	56
	PMT Control Program.....	58
	Exposure Measurements.....	59
	Energy Dependence.....	59
	Linearity	60
	Reproducibility.....	60
	Dosimeter Response versus Bend Radius	60
	Angular Dependence	61
	Results.....	61
	Energy Dependence.....	61
	Linearity	62
	Reproducibility.....	62
	Dosimeter Response versus Bend Radius	62
	Angular Dependence	63
	Discussion.....	63
	Conclusions.....	65
4	CHARACTERIZATION OF THE FIBER-OPTIC COUPLED DOSIMETER AT MEGAVOLTAGE ENERGIES	74
	Introduction.....	74
	Methods and Materials	76
	FOC Dosimetry System.....	76
	Dose Measurements.....	77
	Linearity	77
	Reproducibility.....	78
	Dose Rate Dependence.....	78
	Field Size Dependence	78
	Results.....	79
	Linearity	79
	Reproducibility.....	79
	Dose Rate Dependence.....	79
	Field Size Dependence	79
	Discussion.....	80
	Conclusion.....	84
5	AN ORGAN AND EFFECTIVE DOSE STUDY OF XVI [®] AND OBI [®] CONE-BEAM CT SYSTEMS	89
	Introduction.....	89
	Methods and Materials	90
	CBCT Systems Evaluated	90

Anthropomorphic Phantom	92
Dosimetry System	93
Calculation of Organ Doses.....	95
Calculation of Effective Dose	97
Image Quality	98
Results.....	99
Head.....	100
Chest.....	100
Pelvis	101
Discussion.....	101
Conclusions.....	105
6 ESTIMATION OF ORGAN DOSES FROM KILOVOLTAGE CONE-BEAM CT IMAGING USED DURING RADIOTHERAPY PATIENT POSITION VERIFICATION	117
Introduction.....	117
Methods and Materials	118
CBCT Systems Evaluated	118
Phantom Setup and Dosimetry	119
Cone Beam Dose Index (CBDI).....	119
ImPACT Dose Calculation.....	123
Results.....	124
Discussion.....	124
Conclusions.....	128
7 CONCLUSION.....	134
Results of this Work	134
Opportunities for Future Work and Development.....	135
Anthropomorphic Phantom Development.....	135
Fiber-optic Coupled (FOC) Dosimetry System.....	136
CBCT Dosimetry	137
Final Thoughts.....	138
LIST OF REFERENCES.....	139
BIOGRAPHICAL SKETCH	149

LIST OF TABLES

<u>Table</u>	<u>page</u>
1-1 Comparison of $CBDI_w$ and RANDO phantom measurements.....	31
1-2 Imaging doses from Elekta XVI and Varian OBI.....	31
1-3 Varian OBI organ doses measured in standard dose mode.....	32
2-1 ICRP 103 organs of interest for the calculation of effective dose and their associated weighting factors.....	49
3-1 Reproducibility of measurements with FOC dosimeter at kV energies	67
4-1 Reproducibility of measurements with FOC dosimeter at MV energies.....	85
4-2 Counts from signal and reference fibers as well as output factors normalized to a 10x10 cm field size from a 200 MU irradiation	85
4-3 Counts from each optical fiber with no scintillator during a 50 MU irradiation	85
4-4 Counts from signal and reference fibers from a 50 MU irradiation after passing through a 400 nm high pass filter	86
4-5 Counts from signal and reference fibers from a 50 MU irradiation free in air.....	86
5-1 Nominal technical settings and measured HVLs for each imaging protocol investigated	107
5-2 Organs investigated and number of measurement locations.....	108
5-3 Weight fractions of red bone marrow, A_i , and endosteum, E_i , for various locations of interest of the 50th percentile adult male hybrid phantom.	109
5-4 Organ and effective doses from the Elekta XVI CBCT system	110
5-5 Organ and effective doses from the Varian OBI CBCT system.....	111
5-6 Results of image quality tests for manufacturer installed protocols.....	112
6-1 Empirical ImPACT factors and normalized CBDI values for use with Equation 6-4.....	130
6-2 Measured CBDI values (in mGy_{air}) $\pm 1\sigma$	130
6-3 Measured organ doses, in mGy_{tissue} , taken from Chapter 5, along with organ dose estimates made using the ImPACT CT patient dose calculator, also in mGy_{tissue}	131
6-4 Organ dose conversion coefficients for each protocol.....	132

LIST OF FIGURES

<u>Figure</u>	<u>page</u>
1-1 Elekta Synergy linac with XVI CBCT system	33
1-2 Varian 23iX linac with OBI CBCT system	33
1-3 Head and body CTDI phantoms	34
1-4 Longitudinal dose profiles across a 26 cm imaging field in a CTDI body phantom	34
1-5 TLD measured doses (cGy) within RANDO pelvic phantom using OBI system	35
2-1 Completed 50 th percentile hybrid computational phantom	50
2-2 Axial image with segmented organs from the hybrid computational phantom	51
2-3 A finished bitmap image ready to be imported into the milling software	51
2-4 Finished soft tissue mold, ready to be poured with STES material	52
2-5 Completed axial slice with a) STES, b) LTES, and c) BTES	52
2-6 Torso of completed 50 th percentile physical phantom	53
3-1 Completed FOC dosimeter. Scintillating element at left and SMA connector at right	68
3-2 Close up of scintillating element end of dosimeter	68
3-3 New dosimeter design with reference fiber incorporated into FOC dosimeter assembly	69
3-4 FOC dosimetry system schematic	69
3-5 Screenshot of PMT control program GUI	70
3-6 Energy dependence of FOC dosimeter	71
3-7 Energy dependence of FOC dosimeter as a function of depth in soft tissue-equivalent material	71
3-8 Dose linearity of FOC dosimeter	72
3-9 Response of FOC dosimeter versus the bend radius of the optical fiber	72
3-10 Angular dependence of FOC dosimeter to an axial irradiation	73
3-11 Angular dependence of FOC dosimeter to a normal-to-axial irradiation	73

4-1	Radiation induced light in a silica optical fiber.	87
4-2	Dose linearity of FOC dosimeter	87
4-3	Response of FOC dosimeter versus dose rate in MU/min	88
5-1	Scanning configuration for each imaging protocol used	113
5-2	Schematic detailing the components of the dosimetry system	114
5-3	Axial slice of the physical phantom with an FOC dosimeter installed in the right kidney for dose measurements.....	115
5-4	Example of reconstructed images of CTP592 resolution phantom	115
5-5	Example of reconstructed images of CTP401 low contrast phantom.....	116
6-1	Dose profiles from XVI chest protocol as measured at the center and periphery of a CTDI body phantom	133

Abstract of Dissertation Presented to the Graduate School
of the University of Florida in Partial Fulfillment of the
Requirements for the Degree of Doctor of Philosophy

IMAGING DOSES IN RADIATION THERAPY FROM
KILOVOLTAGE CONE-BEAM COMPUTED TOMOGRAPHY

By

Daniel Ellis Hyer

May 2010

Chair: David E. Hintenlang
Major: Nuclear Engineering Sciences

Advances in radiation treatment delivery, such as intensity modulated radiation therapy (IMRT), have made it possible to deliver large doses of radiation with a high degree of conformity. While highly conformal treatments offers the advantage of sparing surrounding normal tissue, this benefit can only be realized if the patient is accurately positioned during each treatment fraction. The need to accurately position the patient has led to the development and use of gantry mounted kilovoltage cone-beam computed tomography (kV-CBCT) systems. These systems are used to acquire high resolution volumetric images of the patient which are then digitally registered with the planning CT dataset to confirm alignment of the patient on the treatment table.

While kV-CBCT is a very useful tool for aligning the patient prior to treatment, daily use in a high fraction therapy regimen results in a substantial radiation dose. In order to quantify the radiation dose associated with CBCT imaging, an anthropomorphic phantom representing a 50th percentile adult male and a fiber-optic coupled (FOC) dosimetry system were both constructed as part of this dissertation. These tools were then used to directly measure organ doses incurred during clinical protocols for the head, chest, and pelvis. For completeness, the dose delivered from both the X-ray Volumetric Imager (XVI, Elekta Oncology Systems, Crawley, UK) and the

On-Board Imager (OBI, Varian Medical Systems, Palo Alto, CA) were investigated. While this study provided a direct measure of organ doses for estimating risk to the patient, a practical method for estimating organ doses that could be performed with phantoms and dosimeters currently available at most clinics was also desired. To accomplish this goal, a 100 mm pencil ion chamber was used to measure the “cone beam dose index” (CBDI) inside standard CT dose index (CTDI) acrylic phantoms. A weighted CBDI (CBDI_w), similar to the weighted CT dose index (CTDI_w), was then calculated to represent the average dose in the acrylic phantom. By comparing this value to the measured organ doses, organ dose conversion coefficients were developed. These conversion coefficients allow specific organ doses to be estimated quickly and easily using readily available clinical equipment.

CHAPTER 1 INTRODUCTION

Cancer

Cancer refers to the group of diseases characterized by uncontrolled proliferation and spread of abnormal cells.¹ This uncontrolled proliferation commonly produces a mass of tissue called a malignant tumor. A malignant tumor may be contrasted with a non-cancerous benign tumor in that a malignancy is not self-limited in its growth, is capable of invading adjacent tissues, and may be capable of spreading to distant tissues (metastasizing), while a benign tumor has none of these properties.² If not controlled, the spread of cancerous cells to surrounding tissue or other parts of the body can result in death. In the United States alone, it is expected that nearly 1.5 million people will be diagnosed with cancer in 2009, resulting in approximately 560,000 deaths.³ This ranks cancer as the second most common cause of death in the United States, exceeded only by heart disease. Once diagnosed, cancer is typically treated by surgery, chemotherapy, hormone therapy, gene therapy, radiation therapy, or a combination of these therapies depending on the specific type, location, and stage of cancer. Radiation therapy, which is of interest for the purpose of this work, will be explored in the following sections.

Radiation Therapy

In radiation therapy (also called radiotherapy), high-energy ionizing radiation is used to damage the genetic material (DNA) of cancer cells and stop them from growing and dividing. This ultimately helps control the spread of cancer and shrinks the size of tumors. The most common form of radiation therapy is external beam treatment, which typically uses a linear accelerator to produce a beam of x-rays that can be directed at the treatment site. The energy of the x-rays used is on the order of millions of electron volts (MeV), therefore the linear accelerator is said to produce a megavoltage (MV) beam. The MV beam of radiation has several

favorable characteristics which make it valuable for use in treating tumors. First, MV photons have sufficient energy to painlessly reach deep inside the patient. Second, skin tissue is spared with MV radiation compared to lower energy kilovoltage (kV) radiation used in diagnostic procedures. This is because secondary electrons resulting from interactions with MV photons at the surface of the patient have sufficient energy to travel away from the surface of the patient and deposit their energy at a finite depth in the patient rather than locally at the skin. Radiation therapy can also be administered internally, by placing a small radioactive source within a body cavity in close proximity to the area being treated (intracavitary brachytherapy) or by implanting small radioactive seeds directly into the tissue to be treated (interstitial brachytherapy). Some forms of radiation therapy also include directly injecting a radioactive material into the bloodstream that has been attached to a compound which is preferentially absorbed by the organ to be treated. The remainder of this section focuses on the treatment of cancer using external beam radiotherapy, laying a foundation for future discussion about the details of accurately positioning the patient on the treatment table.

After diagnosis of the disease, a decision is typically made by the oncologist regarding which treatment modality(ies) will be used. If external beam radiotherapy is chosen, the first step is to develop a treatment plan. Modern treatment plans are based on computed tomography (CT) simulations, which are volumetric studies of the patient in the treatment position.⁴ Before performing the CT simulation, the geometry and extent of the tumor to be treated is determined from previous diagnostic scans used to diagnose the disease. Once determined, the patient is brought in and placed on the CT table where a reference treatment isocenter is selected with the aid of a scout film. At this time, the treatment isocenter is marked on the patient using skin tattoos to aid in future alignment of the patient on the treatment table. Small metal markers are

also temporarily placed at these reference isocenter positions to serve as reference markers that are visible on the subsequent CT images. A CT scan of the region to be treated is then acquired and transferred to a computer workstation equipped with treatment planning software. At this workstation, organs near the treatment volume which could be at risk for radiation damage, referred to as organs at risk, as well as the gross visible extent of the tumor, referred to as the gross tumor volume (GTV), are localized and contoured. A margin around the GTV is then created based on the type, location, and aggressiveness of the tumor. This additional margin is known as the clinical target volume (CTV) and accounts for microscopic extensions of the disease which cannot be seen on the images but must be treated with radiation the same as the visible tumor. The CTV may include surrounding lymph nodes that have tested positive as well. An additional margin on the order of 1 cm is then drawn around the CTV, known as the planning target volume (PTV). This additional margin accounts for patient set-up uncertainties, machine variations in delivering the radiation, and intra-treatment variations that cause the treatment volume to move such as breathing.⁵⁻⁷ As a consequence of creating the PTV, there may be some overlap between surrounding organs at risk and the treatment volume; ultimately restricting the dose that can be delivered to the target without causing normal tissue complications.^{8,9} However, if patient setup variations are reduced, then smaller margins can be used to create the PTV, resulting in a smaller treatment volume and potentially lowering the dose to surrounding organs at risk.¹⁰ In an attempt to more accurately and reproducibly align the patient at each treatment session, there has been a recent trend towards the use of traditional imaging modalities in the treatment room, which is the topic of the next section.

The final step in treatment planning is to determine the beam geometry and optimize the dose to the PTV using treatment planning software. The finished treatment plan is then exported

to a treatment console where it can be delivered to the patient. Treatment is typically delivered in discrete sessions, referred to as fractions, on an outpatient basis 5 days a week for several weeks. Fractions are used to exploit the differences in the ability of healthy cells to repair themselves following radiation damage while cancerous cells are not as efficient at repairing damage and subsequently die.¹¹

Need for Imaging in Radiation Therapy

Recent advances in radiation treatment delivery such as 3D conformal radiation therapy (3DCRT) and intensity modulated radiation therapy (IMRT) have made it possible to deliver large doses of radiation to target volumes with a high degree of conformity. This is particularly true for IMRT, where very tight margins around the target volume are possible along with very steep dose gradients outside of the target volume. While a highly conformal treatment offers the advantage of sparing surrounding normal tissue, this benefit can only be realized if the patient is accurately positioned during each treatment fraction.¹²⁻¹⁶ Traditionally, this is done in two steps: 1. The patient is aligned to the treatment isocenter using skin tattoos made during the CT simulation and 2. A pair of orthogonal portal images of the patient are taken using the MV treatment beam and an electronic portal imaging device (EPID).^{17, 18} These portal images are then compared to digitally reconstructed radiographs (DRRs) from the CT simulation to verify the patient and tumor's position at the time of treatment at a dose of 4-16 cGy per image pair.¹⁹ Unfortunately, the 2-D nature of projection images and the inherently low contrast of MV imaging limit the accuracy of this technique. Because soft tissue targets typically cannot be seen in the MV portal images, bony anatomy is often used as a surrogate landmark for target localization.²⁰⁻²² These shortcomings have led to the development of several other imaging modalities to verify patient setup based on soft tissue structures. These alternate imaging modalities are described in the following sections.

Megavoltage Cone Beam Computed Tomography (MV-CBCT)

As discussed above, verification of patient setup prior to treatment typically relies on the comparison of 2-D portal images to DRRs. However, this process does not make full use of the volumetric information available from treatment planning. Because both CT simulation and treatment planning generate and utilize 3-D datasets, the logical next step is to validate the patient's position in 3-D. Megavoltage cone-beam computed tomography (MV-CBCT) utilizes the megavoltage beam and the same EPID employed for portal imaging to acquire a series of low-dose 2D projections, with the patient dose reported to be in the range of 1-10 cGy.²³ These 2D projections are then used to reconstruct²⁴ a 3D volumetric data set that can be registered with the planning CT to determine if the patient is properly aligned with the machine isocenter. It should also be noted that this procedure is repeated at each treatment fraction, leading to an accumulation of dose on the order of a Gy or more to tissue in the imaging field. A recent clinical study has shown that MV-CBCT images provide adequate quality for the purpose of patient positioning based on implanted metal seeds, bony landmarks, and air cavities.²⁵ However, the limiting factor of MV images will always be the lack of soft tissue contrast and the ability to register with the planning CT based on soft tissue landmarks.²⁶

CT-on-Rails

The desire to achieve target localization with soft tissue contrast comparable to planning CT images has led to the development of "CT-on-rails" systems.^{27,28} These systems incorporate a diagnostic CT system into the treatment room that shares the same patient table with the linear accelerator. In a typical configuration, the patient table is rotated 180° between imaging and treatment. Once the patient is positioned on the table, the CT gantry is mobilized and slides on rails, passing over the patient while scanning (rather than the table moving like in typical diagnostic CT scans). The end result is a diagnostic quality CT image that can be registered with

the planning CT. The patient table is then rotated 180° towards the treatment gantry and the appropriate shifts are made to the patient table, as calculated from the image registration, to ensure that the patient is accurately aligned with the treatment isocenter. Imaging doses to the patient are on the order of 1-3 cGy, on par with a typical diagnostic CT exam.²³ While the CT-on-rails system provides arguably the best treatment room image quality possible, it is not without its own faults. The complexity, space requirements, and cost of such a system are the most obvious criticisms and have limited its popularity with very few units in use today.²⁹

Kilovoltage Cone Beam Computed Tomography (kV-CBCT)

Kilovoltage cone-beam computed tomography (kV-CBCT) combines the superior soft tissue contrast of a CT-on-rails system with the convenience of a MV-CBCT system. These systems consist of a kV generator and flat-panel detector mounted to the linac gantry using retractable arms and share a common axis of rotation with the treatment beam. This technology has gained popularity in recent years and two such systems are currently commercially available: the X-ray Volumetric Imager (XVI[®], Elekta Oncology Systems, Crawley, UK), seen in Figure 1-1, and the On-Board Imager (OBI[®], Varian Medical Systems, Palo Alto, CA), seen in Figure 1-2. Image acquisition is similar to MV-CBCT, with a number of 2D projections taken as beam rotates around the patient which are later reconstructed into a 3D volumetric data set. As a patient setup tool, a kV-CBCT scan is taken after the patient is aligned to the treatment isocenter using the skin tattoos and then digitally registered with the planning CT to verify the patient's position. The use of kV-CBCT yields much better image contrast over traditional MV portal images or MV-CBCT, permitting better localization of soft-tissue structures for improved patient setup accuracy. One recent publication has identified a positioning accuracy improvement, when compared to conventional MV portal images, of up to 3 mm for lung cancer patients with the use of kV-CBCT.³⁰ The improved patient setup accuracy at each treatment fraction allows complex

radiation treatments to be delivered safely and precisely, ultimately leading to improved tumor control and reduced treatment-related toxicity.³¹

While the dose from a single kV-CBCT is reported to be 1-10 cGy,²³ the repeated daily use for patient setup in a high fraction therapy regimen (~40 fractions) has been projected to lead to a total dose of up to 4 Gy³² to surrounding tissue. Unfortunately, unlike traditional MV portal images or MV-CBCT, the additional dose from daily kV-CBCT image guidance cannot be taken into account using current treatment planning software.³³ This is because the imaging dose from kV-CBCT is not radiobiologically equivalent to the MV dose from the treatment beam.³⁴ A value in the range of 2-4 has been suggested for the relative biological effectiveness (RBE) of kV versus MV radiation with chromosomal damage as the endpoint.³⁵ Another issue to consider is the volume of tissue irradiated by each modality. The dose from a kV-CBCT will be distributed through a much larger volume than a conventional MV portal image due to the increased field of view (FOV). The FOV for CBCT can be up to 52.4 cm in diameter and 26 cm long,³⁶ while MV portal images are typically limited to 20x20 cm projections.³⁷ This large FOV results in critical structures and normal tissue well outside of the treatment volume receiving an imaging dose at every fraction. This effect is further magnified by the fact that some organs near the treatment volume typically approach institution or protocol specific dose limits from the treatment beam alone. Therefore, when the extra dose from CBCT imaging is considered, institution or protocol specific organ dose limits, which are put in place to provide a balance between tumor control and normal tissue damage, may be exceeded. This is especially of concern for serial organs such as the spinal cord where the organ can be permanently damaged by an overdose of radiation.

Another concern regarding the daily use of kV-CBCT imaging for patient positioning is the increased risk of inducing a secondary cancer. According to Publication 60 from the

International Commission of Radiological Protection (ICRP), the probability of inducing a fatal cancer from a single radiographic exposure is 5×10^{-5} per mSv.³⁸ This value is based on a linear no-threshold model of radiation risk and is derived primarily from studies of atomic bomb survivors. A recent study reported that the effective dose from a single chest or pelvis kV-CBCT was approximately 23 mSv.³⁹ Using this value along with the risk of inducing a fatal cancer published in ICRP 60, a 35 fraction therapy regimen with daily kV-CBCT imaging has been suggested to induce an additional cancer risk of up to 4%.³⁹

For the reasons discussed above, it is important to quantify organ doses from kV-CBCT imaging in radiation therapy. In the following chapters of this dissertation, the tools necessary to perform this task are described and results are presented. However, before presenting this work, it is important to understand the current state of radiation dosimetry in kV-CBCT through an extensive literature review, presented in the next section. For simplicity, when the term CBCT is used in the remainder of this dissertation, it will refer to kV-CBCT unless otherwise noted.

Current State of Radiation Dosimetry in kV-CBCT

This section begins by presenting a brief history of fan-beam CT dosimetry in order to provide a background for the discussion of the current state of CBCT dosimetry. The standard for determining radiation dose in fan-beam CT is the multiple scan average dose (MSAD).⁴⁰ The MSAD represents the average dose along the longitudinal scan axis, as measured in a standardized cylindrical acrylic phantom, which includes the primary beam contribution as well as the dose attributable to scattered radiation emanating from all adjacent slices. The MSAD can be measured directly by taking a large series of axial CT scans of a phantom with a detector remaining in the center of the scan length and summing the dose contribution from each slice. In the early days of CT, the direct measurement of MSAD was very time consuming as multiple axial scans resulted in considerable x-ray tube heating which required additional time to be taken

between scans for cooling. This led to the development of the computed tomography dose index (CTDI), a nominally equivalent method of estimating MSAD that could be performed with a single axial scan.⁴¹ The equivalence of MSAD and CTDI requires that all contributions from the tails of the radiation dose profile be included in the CTDI dose measurement. The formal definition of CTDI is shown in Equation 1-1, where L is the nominal slice thickness, $D(z)$ is the longitudinal dose profile, and Z is the integration range.

$$CTDI = \frac{1}{L} \int_{-z/2}^{z/2} D(z) dz \quad (1-1)$$

For simplicity, the integral of the dose profile is typically measured by taking a single axial slice at the center of a 100 mm long ionization chamber, and this measurement is known as CTDI₁₀₀. By definition, CTDI₁₀₀ represents the MSAD at the center of a 100 mm scan and underestimates the MSAD for longer scan lengths. This is because the contributions from the tails of the radiation dose profile beyond the 100 mm integration range are not included. In order to reflect the variation of dose deposition at depth, CTDI₁₀₀ is measured at both central and peripheral locations within a specialized phantom. The phantoms used for CTDI measurements were standardized by the Food and Drug Administration (FDA) and consist of polymethylmethacrylate (PMMA) cylinders that are 15 cm in length and either 16 or 32 cm in diameter, representing an adult head and body, respectively.⁴² In the clinic, these phantoms are typically referred to as head and body CTDI phantoms. The phantoms have five holes along the longitudinal axis in which to place an ionization chamber: one in the center and four other peripheral locations 1 cm from the surface at 0°, 90°, 180°, and 270°. For clarification, both the head and body CTDI phantoms are shown in Figure 1-3. In an attempt to represent the average dose within the scan plane, the central as well as the average of the peripheral measurements are combined into the weighted CTDI (CTDI_w), as shown below in Equation 1-2.

$$\text{CTDI}_w = \frac{1}{3}\text{CTDI}_{100,\text{center}} + \frac{2}{3}\text{CTDI}_{100,\text{periphery}} \quad (1-2)$$

The advantage of CTDI_w is that it provides a single CT dose parameter to compare different imaging protocols and equipment. However, it is important to note that it is not intended to represent the dose to objects substantially different than the CTDI phantom in size, shape, or attenuation or when the 100 mm integration length omits a considerable fraction of the scatter tails.⁴³ Additionally, it is independent of the length of the scan and therefore does not represent the total energy deposited within the scan volume. Even with these shortfalls, this technique is still routinely employed in diagnostic radiology to provide an easily measured dose metric that can be used to compare different imaging protocols and equipment.

Initially, one may think that the methodology discussed above for measuring the MSAD could easily be extended to CBCT as a method of reporting radiation dose. However, this methodology is impractical for measuring radiation dose in CBCT because unlike fan-beam CT, CBCT is not a sequential, slice based technique. This means that there is not a need to consider the contribution of scattered radiation from adjacent slices contributing to the dose, which is what MSAD attempts to do. The measurement logic for CBCT simply reverts back to conventional dosimetry, where the radiation dose can be measured in a single axial rotation without worrying about collecting the entire dose profile to compensate for the contribution of scatter from adjacent slices, assuming a large enough phantom is used to produce scatter at the measurement point.⁴⁴ Unfortunately, there is not a widely accepted methodology for performing these dose measurements nor a standardized dose metric such as CTDI for use with CBCT at this time. However, several authors have begun investigating variations of CTDI for CBCT dosimetry as its use in radiation therapy continues to grow. The current state of CBCT dosimetry is reviewed in the remainder of this section.

The use of a variation of CTDI for dosimetry measurements in CBCT has been explored by Amer *et al.*⁴⁵ In this study, the continued use of a standard 100 mm pencil ionization chamber for CBCT dosimetry measurements is supported due to its widespread availability and because the large longitudinal beam width found in CBCT (up to 26 cm) easily exceeds its dimensions. Because the longitudinal beam width exceeds the pencil chamber dimensions, the author argues that dosimetry measurements made with the pencil chamber will provide a reasonable measure of the average dose across the central 100 mm of the FOV. During dose measurements, Amer *et al.* also recommends the addition of 15 cm of Plexiglass to each end of a standard CTDI head and body phantom in order to provide extra scatter medium for the primary beam. To differentiate this dose from CTDI, it was given the name of cone beam dose index (CBDI). Similar to $CTDI_w$, $CBDI_w$ is calculated by weighting the central and peripheral dose measurements as shown in Equation 1-2. Amer *et al.* also addresses the fact that the average dose across the central 100 mm of the FOV as measured by the pencil chamber will be less than the maximum dose at the center of the scan plane because the longitudinal dose profile is not completely flat and decreases away from the central axis due to less scattered radiation. To quantify how much the maximum dose is underestimated by using a pencil chamber, the author measures the longitudinal dose profile from an Elekta x-ray volumetric imaging (XVI) system in both central and peripheral locations of a CTDI phantom using a small 0.125 cm³ ionization chamber. Figure 1-4 shows the measured longitudinal dose profiles for the CTDI body phantom as well as the calculated weighted dose profile. Assuming symmetry of the dose profile shown in Figure 1-4, CBDI was calculated (instead of measured with an actual 100 mm ionization chamber) from the integration of the weighted dose profile across the central 100 mm of the FOV divided by the theoretical chamber length (100 mm). It was found that the average dose

across the central 100 mm of the dose profile underestimated the maximum dose by less than 5% for the 26 cm longitudinal beam width shown in Figure 1-4. The author also repeated these measurements without the additional scatter medium at each end of the CTDI body phantom and it was found that the measurements were lower by 31% and 8% at the center and periphery, respectively. This finding demonstrates the significant contribution of scattered radiation from beyond the length of a standard CTDI phantom when dealing with enlarged longitudinal dose profiles found in CBCT. Organ dose measurements were also made using a RANDO[®] (The Phantom Laboratory, Salem, NY) anthropomorphic phantom and thermoluminescent dosimeters (TLDs) for comparison to the measured $CBDI_w$ values. Table 1-1 summarizes both the $CBDI_w$ values as well as the measurements from the RANDO phantom. As can be seen, the $CBDI_w$ values are generally within 30% of the organ doses listed. The biggest advantage of this study was that the methodology and equipment is similar to what is used for CTDI measurements (with the exception of extra scatter medium at the ends of the CTDI phantoms). This means that performing these measurements would be feasible for most clinics as they already have the necessary equipment readily available. Therefore, the development and introduction of the quantity $CBDI_w$ provides a useful dose metric for CBCT imaging that can be used to compare different imaging protocols and systems between institutions.

A recent study by Song *et al.*⁴⁶ developed another variation of CTDI for dosimetry measurements in CBCT. Instead of using a standard 100 mm pencil chamber for dose measurements, a small 0.6 cm³ Farmer type ion chamber was chosen. This allows “point” measurements of the dose to be made rather than an average measurement over the central 100 mm of the FOV. For completeness, both the Elekta XVI and Varian OBI imaging systems were investigated. Similar to the previous study, the dose was measured at both central and peripheral

locations within cylindrical acrylic phantoms and these doses were weighted as shown in Equation 1-2. To avoid confusion with $CTDI_w$ or $CBDI_w$, it was suggested that this dose be called the weighted cone-beam CTDI ($CBCTDI_w$). It should be noted that the cylindrical acrylic phantoms used in this study were not standard CTDI phantoms as was used in the previous study; instead, they were custom phantoms 25 cm long and either 18 or 30 cm in diameter, representing an adult head and body, respectively. The phantoms also had only two axial holes in which to place an ionization chamber, one at the center and one at the periphery 2 cm from the surface. One concern with this phantom is that it may not be long enough to provide enough scatter medium for the primary beam and therefore the dose at the central scan plane may be underestimated. As previously mentioned, the Elekta XVI can have a nominal beam width of up to 26 cm, exceeding the length of the 25 cm acrylic phantom used in this study. Even so, dose measurements were made in the phantoms for all clinically relevant imaging procedures and a comparison between the two CBCT systems was made. Table 1-2 summarizes the measured doses for each system with manufacturer installed protocols. From Table 1-2, it is clear that the doses measured from the manufacturer installed OBI protocols tend to be higher than XVI protocols for scanning similar body parts. The first reason for this is rather obvious: the OBI unit uses a single setting for both head and body scanning procedures which has a higher kV and mAs than any of the XVI settings. The author also observed that the XVI had a greater half-value layer (HVL) than the OBI system at the same tube settings, suggesting that the beam from the XVI unit has greater filtration than the OBI unit. The lower HVL of the OBI system would be expected to result in an increased dose, even for similar mAs. Unfortunately, doses within an anthropomorphic phantom were not done in this study for comparison to the measured $CBCTDI_w$ values.

While the studies presented above investigated methods of adapting CTDI type measurements to CBCT, other authors have completely abandoned this idea in lieu of dose measurements performed exclusively in realistic anthropomorphic phantoms. These authors argue that dose measurements performed in CTDI phantoms should be taken with great caution to represent patient dose as humans are substantially different in size, shape, and attenuation from the acrylic phantoms used in these studies. Therefore, the use of realistic anthropomorphic phantoms is suggested to directly measure dose metrics that relate to patient risk such as organ dose.

Wen *et al.*³² recently investigated doses delivered by the Varian OBI system to prostate cancer patients receiving pelvic scans for treatment positioning using a RANDO anthropomorphic phantom of the pelvis along with TLDs. The RANDO phantom is commercially available and was originally developed for therapeutic applications at MV energies. One limitation of this phantom is that it is constructed in 2.5 cm thick axial slices allowing limited options for dosimeter placement when performing organ dose measurements. The study performed by Wen *et al.*, however, was not a thorough organ dose study, but simply a study of the dose distribution from CBCT as measured in a realistic anthropomorphic phantom. The measured doses within the phantom from a half-fan scan using the half bow-tie filter with technical settings of 125 kV and 1320 mAs are shown in Figure 1-5. As can be seen in Figure 1-5, tissue and bone doses on the left side of the patient were higher than on the right side. The reason for this asymmetry is twofold: (1) there is a 10 degree rotation overlap on the left lateral side between the start and stop positions of the scan and (2) gantry rotational speed slows near the end of the scan (on the left lateral side) but the dose rate stays constant. For a typical external beam prostate treatment of 42 fractions, the total dose to the left femoral head from daily

imaging could exceed 4 Gy. The author states that even after adding this dose to the femoral dose received from the treatment beam (approximately 34 Gy) at their institution, it is still below their institutional limit of 50 Gy. The institutional limit also states that the volume of either femoral head receiving 50 Gy should be kept below 10% which is also not exceeded by the addition of the imaging dose.

The most comprehensive CBCT organ dose study found in the literature today was recently published by Kan *et al.*³⁹ Organ dose measurements were performed using a RANDO female anthropomorphic phantom, with a minimum of two TLDs placed in each organ in order to determine average organ doses. All measurements were performed only for the Varian OBI system. Most of the 26 organs selected for dose measurements were based on recommendations by the International Commission on Radiation Protection (ICRP) Publication 60 for use in the determination of effective dose.³⁸ The organ doses were measured in two different modes, standard and low-dose mode, for three clinically relevant scan sites: head, chest, and pelvis. All CBCT scans were performed using between 650 and 700 projections with the following acquisition settings: 125 kV, 80 mA, 25 ms (standard mode) and 125 kV, 40 mA, 10 ms (low-dose mode) with a 150 cm source to imager distance. It is important to note that, at the time of this study, the manufacturer has recommended low-dose mode for use in quality assurance only. Table 1-3 summarizes the organ doses measured in standard dose mode as well as the effective dose for all three scan sites. The organ doses for low-dose mode are not shown but on average they were reduced by a factor of four to five compared to those measured using standard mode settings. This reduction in organ dose was as expected because the mAs for the normal dose mode were a factor of five higher than low-dose mode. As expected, the in-field organs received the highest radiation doses while organs out-of-field received very low doses due to scatter of the

primary beam. The author also studied the positioning accuracy for both normal dose and low-dose mode and found that there was no difference in positioning accuracy between the two acquisition modes when bony anatomy was used for registration with the planning CT.

In summary, a widely accepted methodology for reporting radiation dose from CBCT is not currently available in the literature. The first two studies discussed in this section perform dose measurements in cylindrical acrylic phantoms and introduced two similar competing quantities, CBDI and CBCTDI. Unfortunately, neither study makes an attempt to relate these quantities to patient doses of interest such as organ doses. The last two studies discussed perform dose measurements exclusively in anthropomorphic phantoms, but major changes to the factory installed clinical protocols since their publication makes much of the data outdated. Also, no attempt to relate these organ doses to easily measured cylindrical phantom dose measurements was made. Ultimately, it is desired to develop a method to estimate organ doses from a metric such as CBDI that can be easily measured using currently available clinical equipment. Reaching this goal is one of the objectives of this research, as discussed in the next section.

Objectives of this Research

The main goal of this research was to develop the tools and methods necessary to accurately quantify organ doses incurred by the patient during kilovoltage cone-beam CT imaging used in radiation therapy. To reach this goal, organ doses were first quantified from direct measurement within an anthropomorphic phantom using current manufacturer installed clinical protocols for the two commercially available CBCT systems (Elekta XVI and Varian OBI). The cone-beam dose index (CBDI) was also measured for the same clinical protocols using standard CTDI head and body phantoms along with a 100 mm pencil chamber. A ratio of measured organ doses to the weighted CBDI was then taken in order to develop organ dose conversion coefficients (ODCCs). These conversion coefficients allow organ doses to be

estimated quickly and easily without the need to repeat the time consuming anthropomorphic phantom organ dose measurements for future changes to the technical settings of scan protocols.

In order to complete these tasks in a timely and organized manner, they were broken up into 4 smaller projects, each of which is presented below.

1. The first project was to construct an anthropomorphic phantom for use in organ dose measurements. In order to best represent the human population, the phantom was constructed based on a dataset representing a 50th percentile adult male, as defined by the International Commission on Radiological Protection (ICRP) Report 89.⁴⁷ To accurately represent the dosimetric characteristics of a real human, three different tissue equivalent materials representing bone, lung, and soft tissue were incorporated into the construction process. To aid in dosimeter placement for organ dose measurements, organ locations were transferred onto the axial slices of the physical phantom using a permanent marker from printouts of the segmented dataset.
2. The need for a small dosimeter capable of anthropomorphic phantom absorbed dose measurements prompted the development and characterization of a new water-equivalent fiber optic coupled (FOC) dosimeter. The FOC architecture was chosen due to its small size (0.5 mm length and 2 mm diameter sensitive element) and ability to provide real-time dose information during irradiation. An array of 5 photomultiplier tubes (PMTs) and custom software was also developed to permit the simultaneous readout of multiple dosimeters. The dosimeters were fully characterized at diagnostic energies and offered excellent sensitivity, reproducibility, and dose linearity while exhibiting minimal angular and energy dependence.
3. Organ dose measurements, using the anthropomorphic phantom and FOC dosimetry system discussed above, were performed on the two CBCT systems currently available on medical linear accelerators, namely the X-ray Volumetric Imager (XVI[®], Elekta Oncology Systems, Crawley, UK) and the On-Board Imager (OBI[®], Varian Medical Systems, Palo Alto, CA). Organs chosen for investigation in this study were based on recommendations by ICRP report 103 for the calculation of effective dose.⁴⁸ For completeness, three different clinically relevant scan sites were investigated which included the head, chest, and pelvis. All scans were performed using current manufacturer installed clinical protocols and appropriate bow-tie filters. The measured organ doses were also used to calculate a reference male effective dose for each procedure. The effective dose is an important parameter because it provides a single value that permits a dosimetric comparison between different radiographic and nuclear medicine procedures. This information is expected to contribute greatly to the medical physics community because current organ dose data for CBCT imaging is very limited.
4. Due to the time consuming nature and requirement for specialized equipment involved with the direct measurement of organ doses, it was desired to develop a method for accurately estimating organ doses using dosimeters and phantoms currently found in most clinics. To accomplish this goal, the cone-beam dose index (CBDI) was measured using

standard CTDI head and body phantoms and a 100 mm pencil chamber. Organ dose conversion coefficients (ODCCs) were then developed by taking a ratio of previously measured organ doses and the weighted CTDI values measured using the same clinical protocols. These coefficients allow organ doses to be estimated from simple measurements of the weighted CTDI rather than repeating the time consuming anthropomorphic phantom measurements and accommodate future changes to the technical settings of the clinical protocols.

The following chapters of this dissertation are dedicated to the discussion of each of these projects in detail. Each chapter corresponds to a particular project outlined above and gives the background, methodology, and results obtained. An extra chapter on the characterization of the FOC dosimeter at MV energies has also been included as an extension of the work outlined in the second specific aim.

Table 1-1. Comparison of CBDI_w and RANDO phantom measurements (Adapted from: A. Amer, T. Marchant, J. Sykes, J. Czajka and C. Moore, "Imaging doses from the Elekta Synergy X-ray cone beam CT system," Br J Radiol **80**, 476-482 (2007), Tables 1 and 3, p. 479 and 480).

Site	Beam settings		Collimator	Phantom dimensions		CBDI _w [mGy]	Rando [mGy]	Position
	kV	mAs		Diam [cm]	Length [cm]			
Head	100	38	S20	16	29	1.6	1.3	Surface (Ant)
							1.2	Surface (Lat)
							1.3	Eye lens
Lung	120	152	S20	32	44	6	10	Surface (Ant)
							7.2	Surface (Lat)
							7.2	Heart
Pelvis	130	456	S20	32	44	25	34	Surface (Ant)
							23	Surface (Lat)
							21	Uterus

31

Table 1-2. Imaging doses from Elekta XVI and Varian OBI (Adapted from: W. Y. Song, S. Kamath, S. Ozawa, S. A. Ani, A. Chvetsov, N. Bhandare, J. R. Palta, C. Liu and J. G. Li, "A dose comparison study between XVI and OBI CBCT systems," Med Phys **35**, 480-486 (2008), Tables 2 and 3, p. 482).

Protocol	Beam settings		Collimator	Phantom dimensions		CBCTDI _w [mGy]	
	kV	mAs		Diam [cm]	Length [cm]		
XVI	Head and neck	100	36.1	S20	18	25	10
	Prostate	120	1028.8	M10	30	25	35
	Pelvis	120	643	M20	30	25	24
	Chest	120	643	L20	30	25	18
OBI	Full-fan	125	1260	Full bow-tie	18	25	83
	Half-fan	125	1260	Half bow-tie	30	25	54

Table 1-3. Varian OBI organ doses measured in standard dose mode (Adapted from: M. W. Kan, L. H. Leung, W. Wong and N. Lam, "Radiation dose from cone beam computed tomography for image-guided radiation therapy," *Int J Radiat Oncol Biol Phys* **70**, 272-279 (2008), Table 4, p. 275).

Tissue/organ	Mean absorbed dose (cGy)					
	Head scan		Chest scan		Pelvis scan	
Gonads (ovary)	0.02	± 0.01	0.06	± 0.01	3.75	± 0.31
Bone marrow (whole body)	0.8	± 2.91	3.04	± 3.23	2.03	± 2.06
Bone marrow (irradiated site)	5.89	± 0.78	6.89	± 0.46	4.22	± 0.33
Colon	0.05	± 0.02	0.35	± 0.07	5.43	± 0.18
Lung	0.57	± 0.31	5.34	± 1.77	0.08	± 0.02
Stomach	0.07	± 0.02	4.37	± 1.61	0.59	± 0.12
Bladder	0.02	± 0.01	0.07	± 0	5.29	± 0.82
Breast	0.21	± 0.05	4.69	± 0.18	0.12	± 0.04
Liver	0.07	± 0.02	3.87	± 1.76	0.63	± 0.14
Esophagus	3.81	± 4.43	3.59	± 2.57	0.08	± 0.04
Thyroid	11.1	± 1.19	0.79	± 0.07	0.04	± 0.01
Skin (whole body)	0.92	± 3.27	2.77	± 3.1	2.59	± 2.67
Skin (irradiated site)	6.66	± 1.19	6.44	± 0.95	5.43	± 1.37
Bone surface	0.8	± 2.91	3.04	± 3.23	2.03	± 2.06
Remainder organ						
Adrenals	0.05	± 0.01	1.22	± 0.08	1.05	± 0.07
Brain	4.8	± 0.69	0.08	± 0.02	0.03	± 0.01
Upper large intestine	0.05	± 0.01	1.41	± 0.01	1.17	± 0.06
Small intestine	0.04	± 0.01	0.31	± 0.02	6.23	± 0.29
Kidney	0.05	± 0.01	0.81	± 0.05	1.72	± 0.13
Muscle	0.08	± 2.91	3.04	± 3.23	2.03	± 2.06
Pancreas	0.04	± 0.01	0.83	± 0.01	1.9	± 0.12
Spleen	0.06	± 0.01	2.16	± 0.18	0.67	± 0.04
Thymus	11.1	± 1.19	0.79	± 0.07	0.04	± 0.01
Uterus	0.02	± 0.01	0.06	± 0.01	3.8	± 0.27
Other critical organ						
Rectum	0.02	± 0.01	0.05	± 0.01	3.99	± 0.27
Lens	6.22	± 0.49	0.13	± 0.01	0.04	± 0.02
Heart	0.2	± 0.04	6.72	± 0.55	0.17	± 0.03
Spinal cord	4.08	± 3.62	3.58	± 3.23	0.11	± 0.06
Effective dose (mSv)	10.3	± 0.46	23.6	± 0.35	22.7	± 0.29



Figure 1-1. Elekta Synergy linac with XVI CBCT system. XVI imaging system is shown in the horizontal plane with imaging detector at left and kV x-ray tube at right.



Figure 1-2. Varian 23iX linac with OBI CBCT system. OBI imaging system is shown in the horizontal plane with x-ray tube at left and imaging detector at right.

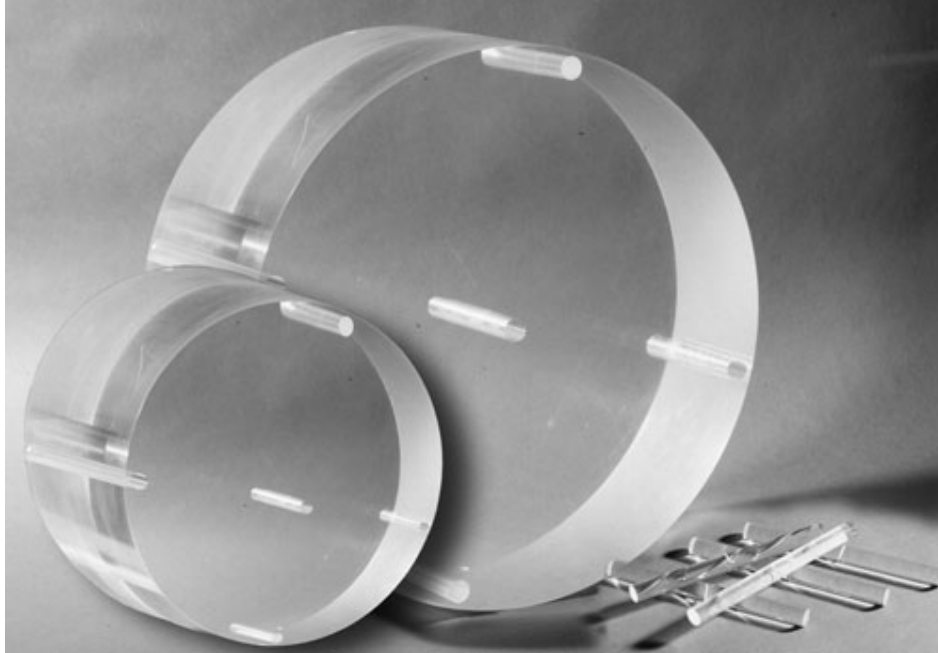


Figure 1-3. Head and body CTDI phantoms

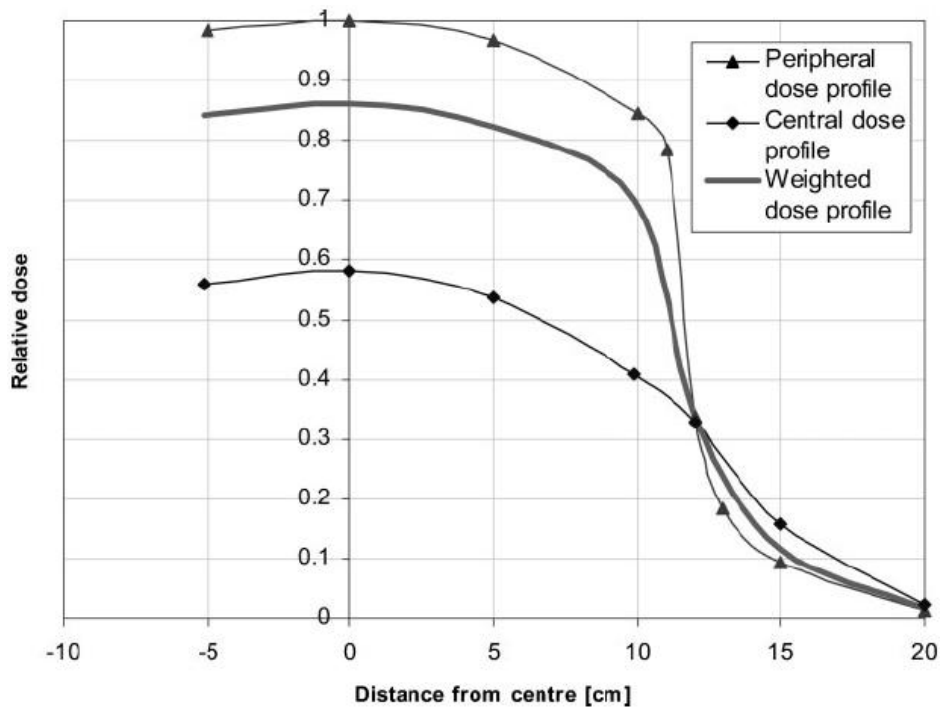


Figure 1-4. Longitudinal dose profiles across a 26 cm imaging field in a CTDI body phantom (Used with permission from: A. Amer, T. Marchant, J. Sykes, J. Czajka and C. Moore, "Imaging doses from the Elekta Synergy X-ray cone beam CT system," Br J Radiol **80**, 476-482 (2007), Figure 3, p. 479).

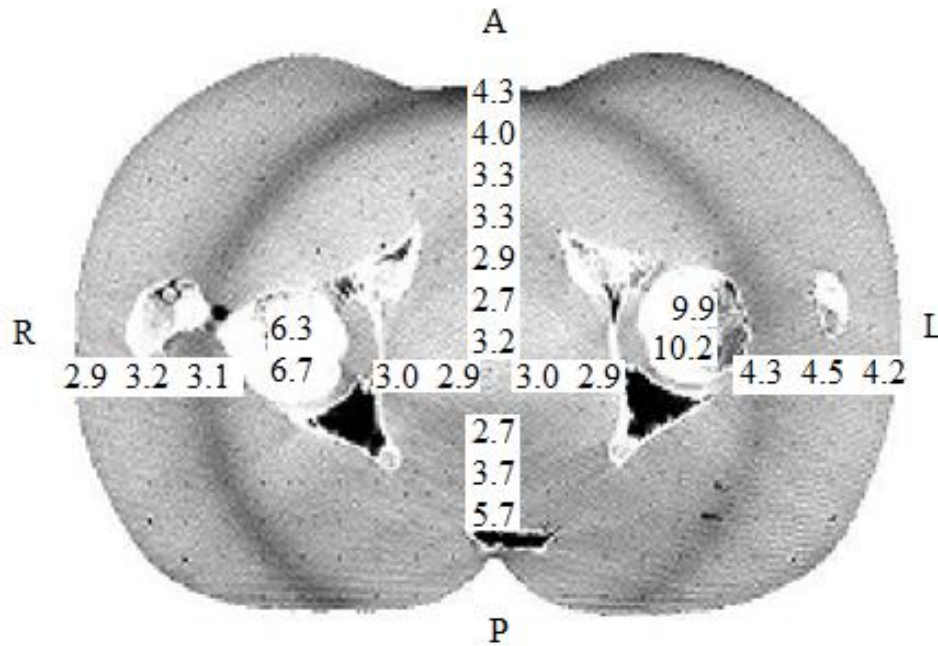


Figure 1-5. TLD measured doses (cGy) within RANDO pelvic phantom using OBI system (Used with permission from: N. Wen, H. Guan, R. Hammoud, D. Pradhan, T. Nurushev, S. Li and B. Movsas, "Dose delivered from Varian's CBCT to patients receiving IMRT for prostate cancer," *Phys Med Biol* **52**, 2267-2276 (2007), Figure 3, p. 2272)

CHAPTER 2 CONSTRUCTION OF A 50TH PERCENTILE ADULT MALE ANTHROPOMORPHIC PHANTOM

Introduction

Anthropomorphic phantoms constructed from tissue-equivalent materials have historically been used to provide a physical representation of the body's anatomy and attenuation characteristics for radiation dosimetry studies. Of particular interest for this study is the use of anthropomorphic phantoms for quantifying organ doses during CBCT imaging in radiation therapy; similar to previous studies performed by other authors in computed tomography (CT) and pediatric radiology.^{39, 49, 50} Performing organ dose measurements in physical phantoms offers a distinct advantage over computational methods because knowledge of the exact photon energy spectrum or irradiation geometry is not required. This is especially useful considering the increasing use of proprietary equipment and scanning techniques that are difficult to model such as bow-tie filters, automatic tube-current modulation in CT, and automatic exposure control (AEC) in fluoroscopy. Currently, the majority of organ dose studies in diagnostic imaging utilize commercially available anthropomorphic phantoms such as RANDO[®] (The Phantom Laboratory, Salem, NY) or ATOM[®] phantoms (Computerized Imaging Reference Systems, Inc, Norfolk, VA). In order to provide an accurate representation of the human anatomy, these commercially available phantoms typically use three tissue equivalent materials imitating bone, lung, and soft tissue. To allow access to organ locations for the placement of dosimeters, the RANDO[®] and ATOM[®] phantoms are assembled in axial slices 2.5 cm thick. Unfortunately, the widespread clinical use of these phantoms has been limited by their prohibitive costs.

To overcome this limitation, the methodology required to construct an inexpensive anthropomorphic phantom (as compared to commercially available phantoms) using readily available materials was recently developed at the University of Florida.⁵¹ Expanding upon

methods originally published by White *et al.*,^{52, 53} and later improved upon by Jones *et al.*,⁵⁴ the phantom was constructed using three tissue-equivalent materials: soft tissue-equivalent substitute (STES), lung tissue-equivalent substitute (LTES), and bone tissue-equivalent substitute (BTES). BTES is based on an epoxy resin which forms a hard plastic, as previously described by Jones *et al.*⁵⁴ STES and LTES are based on a new urethane mixture which forms a pliable compound as described by Fisher.⁵⁵ The urethane compound was chosen for ease in phantom construction, improved phantom durability, and easier accommodation of fiber optic coupled (FOC) dosimeters which will be discussed in later chapters.

The anthropomorphic phantom constructed for this study was unique in several aspects. First, it was based on a hybrid computational model representing a 50th percentile adult male.⁵⁶ In this context, hybrid refers to a cross between stylized and tomographic phantoms, exploiting the advantages of each. A hybrid phantom offers the scalability of a stylized phantom while maintaining the anthropomorphic characteristics of a tomographic phantom. The hybrid model originated from a tomographic dataset of a 36 year old Korean male (176 cm height, 73 kg weight). Using methods previously described by Lee *et al.*^{57, 58}, the tomographic dataset was imported into Rhinoceros computer software (McNeel North America, Seattle, WA) and transformed into non-uniform rational B-spline (NURBS) surfaces that could easily be manipulated. Modifications to the original dataset were done to match the anthropometric dimensions and organ masses of a 50th percentile adult male as defined by the International Commission on Radiological Protection (ICRP) Report 89 reference data.⁴⁷ The completed 50th percentile adult male hybrid computational phantom is shown in Figure 2-1. In order to construct the physical phantom from this data set, the hybrid computational phantom was first voxelized at a 2x2x5 mm resolution. The voxelized dataset was then imported into ImageJ computer software

(Version 1.34s, National Institute of Health, Bethesda, MD) and converted into 5 mm thick axial images. These axial images were then used as the blueprint from which to construct the physical phantom. The direct link between the computational and physical phantoms is one of the key advantages of this series; allowing the physical phantom to serve as an experimental validation for Monte Carlo codes. Additionally, the computational phantom can be used to determine point-to-organ dose scaling factors, allowing the calculation of average organ doses from simple point dose measurements made in the physical phantom.⁵⁹

In order to allow a greater variety of choices for dosimeter placement when performing internal dose measurements, the physical phantom was constructed and assembled in axial slices 5 mm thick. While the full-body data set includes 353 axial slices of this thickness, the lack of radiosensitive organs in the legs justified their exclusion from fabrication. As such, the physical phantom includes 193 axial slices, ranging from the crown of the head to mid-thigh. All internal organs in the phantom are modeled as soft tissue and therefore dosimeter placement for organ dose measurements is based solely on position of the segmented organs in the computational hybrid phantom. To aid in dosimeter placement, organ locations have been transferred onto each slice from full-scale axial printouts of the computational hybrid data set.

Methods and Materials

Materials

The tissue-equivalent substitutes used for this undertaking were developed with two goals in mind: 1. Similar physical properties to human tissue, such as density and attenuation coefficients, and 2. Ease of integration into the phantom manufacturing process. To meet these goals, a new urethane based STES and LTES were developed by Fisher.⁵⁵

The newly developed tissue-equivalent materials were evaluated by measuring the material density and attenuation properties. The attenuation coefficient of the STES was evaluated by

measuring the attenuation from multiple thicknesses of material using a narrow beam geometry generated by clinical radiographic unit. Additionally the Hounsfield Unit (HU) values were measured in the completed phantom using a Siemens Somatom Sensation 16-slice CT scanner operated at a tube voltage of 120 kVp and employing an mA modulated exposure control. The average HU was determined from the selected regions of interest (ROI) using areas of approximately 10 cm².

Density measurements of each sample were then taken utilizing Archimedes’s principle. A cured sample of each material was weighed on a scale with 0.001 gram precision to find the dry mass, m_{dry} , of each sample. The samples were then weighed submerged in a beaker of de-ionized water to find the wet mass, m_{wet} , of each sample. Using both these measurements, as well as the known density of the de-ionized water, $\rho_{\text{H}_2\text{O}}$, the density of each sample was calculated using Equation 2-1.

$$\rho_{\text{sample}} = \frac{m_{\text{dry}}}{\left[\frac{m_{\text{dry}} - m_{\text{wet}}}{\rho_{\text{H}_2\text{O}}} \right]} \quad (2-1)$$

Soft tissue-equivalent substitute (STES)

The new urethane based STES was designed to match the x-ray attenuation and density of human soft tissue within the diagnostic energy range (80-120 kVp). Specifically, the STES was designed to have a density similar to that of human soft tissue (1.04 g/cm³) and to achieve a target x-ray attenuation coefficient based on the ICRU-44 reference soft tissue composition.^{55, 60}

The commercially available, two-part urethane rubber compound “PMC 121/30 Dry”, (Smooth-On, Easton, PA), was combined with 2.8% by weight of powdered CaCO₃ (Fisher Scientific, Hanover Park, IL) to achieve these design goals. The calcium carbonate was added to the two parts of urethane and mixed with an electric mixer, with care being taken to ensure a

homogeneous mixture with no undissolved CaCO_3 . The durable, readily available urethane based compound was found to be easy to work with and did not suffer from phase separation problems frequently encountered with epoxy resin based STES. An additional advantage of the urethane based STES is the material's flexibility, which allows it to be easily removed from molds after curing.

Adipose tissue was not specifically modeled in the construction of the physical or computational phantoms. The distribution of subcutaneous as well as intra-abdominal adipose tissue was initially determined to be too complicated to directly model with a specific tissue equivalent material. Thus, the STES was developed to be a homogeneous soft tissue analog that comprises skeletal muscle as well as organs, connective tissue and adipose tissue.

Lung tissue-equivalent substitute (LTES)

A new LTES was designed by combining uncured urethane based STES, prepared as described above, along with poly-fil[®] polystyrene micro beads (Fairfield Processing, Danbury, CT) in a 10:1 ratio by weight. This LTES is very uniform and permits the fabrication of a range of tissue densities spanning those representative of various levels of inspiration. Since it does not rely on a tissue surfactant and foaming agent, the LTES is more uniform and reproducible than the method proposed by White et al.⁶¹ While the density of lung tissue can vary widely depending on the level of inspiration, patients undergoing diagnostic procedures are typically asked to hold their breath during the exposure. Therefore, a value of 0.33 g/cm^3 was chosen for the LTES, representing the density of a fully inspired lung.⁶⁰

Bone tissue-equivalent substitute (BTES)

The BTES used was the epoxy resin based material previously developed by Jones et al.⁵⁴ By mass, the mixture of the BTES is as follows: 36.4% Araldite GY6010 and 14.6% Jeffamine T-403 (Huntsman Corp., Woodlands, TX), as well as 25.5% Silicon Dioxide and 23.5% Calcium

Carbonate (Fisher Scientific, Hanover Park, IL). It was designed to represent a homogenous mixture of cortical and trabecular spongiosa (bone trabeculae and bone marrow). The BTES composition was adjusted to match the mass density, mass attenuation coefficients (μ/ρ), and mass energy absorption coefficients (μ_{en}/ρ) for those defined by the Oak Ridge National Laboratory (ORNL) stylized model series⁶² within the diagnostic photon energy range. The effective atomic number for the BTES (8.80) is very similar to that of the ORNL reference tissue (8.59), and it was shown that values of μ/ρ and μ_{en}/ρ for BTES had a maximum deviation from ORNL reference values of only a few percent.⁵⁴

Phantom Construction Methodology

Initially, the methodology described by Jones *et al.*⁶³ in the construction of a newborn phantom was to be used in the construction of the adult phantom series. This method involved several steps: preparing epoxy based soft tissue material in a vacuum chamber to eliminate air bubbles, pouring the material into a square mold, milling out the outer slice contour as well as appropriate voids for bone and lung tissue-equivalent material, and finally filling these voids with bone or lung tissue-equivalent material as required. However, the far greater number and size of slices required to construct an adult phantom, as compared to a newborn phantom, required many changes in the original construction methodology if a phantom was to be completed in a timely manner. To speed the construction process, an automatic machining system (VisionPro Version 7, Vision Engraving and Routing Systems, Phoenix AZ) was purchased for the purpose of creating soft tissue molds from axial images of the hybrid computational phantom. An example of an axial image with segmented organs from the hybrid computational phantom is shown in Figure 2-2. Once the phantom construction was initiated, problems were identified and overcome as they arose. The final means of production are detailed below.

Creating soft tissue molds

As previously mentioned, the physical phantom was constructed based on hybrid computational phantom of a 50th percentile adult male. The original tomographic data for this phantom came from a 36 year old Korean adult male (176 cm height, 73 kg weight). The exam was performed as part of a cancer screening protocol using a Siemens Somatom Emotion Duo PET/CT system with a slice resolution of 3mm. All scans were performed at full inspiration with an in-plane matrix size of 512x512 pixels. Organ segmentation was performed manually under supervision of a radiologist. While approximately 100 different tissues were segmented in the computational data set, only the organs needed for the calculation of effective dose (with exception of muscle and lymphatic nodes) were transferred to the physical phantoms. A list of these organs and their tissue weighting factors, as outlined in ICRP 103,⁴⁸ is shown in Table 2-1.

The first step in constructing the phantom was to convert the axial images from the computational data set into a form that could ultimately be read with the automated machining software. Using ImageJ software (Version 1.34s, National Institute of Health, Bethesda, MD), each segmented axial image was converted into a bitmap representing only soft tissue and voids (bone, lung, air). This was accomplished by segmenting bone, lung, and air to a single pixel value representing “voids,” while all remaining soft tissues were shaded with another single value representing soft tissue. Registration marks for assisting in phantom assembly and alignment were also added to each bitmap image at anterior and lateral positions. A finished bitmap image showing only soft tissue, voids, and registrations marks is shown in Figure 2-3. Once completed, the finished bitmaps were then imported into the VisionPro software. Each bitmap was adjusted to conform to the 256 value color range in the VisionPro software and vectorized in order to smooth the pixilated edges of the digital images. A speckle filter was used to eliminate tissue islands less than four pixels in area. Once these steps were complete,

engraving paths for all areas represented by the soft tissue pixel value were then created for each slice. Realizing that smaller diameter “end mill” bits allow finer details to be cut, a 1/8” diameter bit was selected for body engraving paths while a 1/16” diameter bit was chosen for engraving paths in more detailed regions of the head.

The engraving paths were used to mill soft tissue molds in a high density foam, which could then be filled with the soft tissue substitute. Foam blanks were fastened to the engraving table and single-pass engraving paths were set with depths resulting in 5 mm thick soft tissue slices. To create clean edges in each foam mold, a perimeter engraving path was first performed at a slow feed (0.6” per second), outlining the entire perimeter of the area to be cut. This was followed by a much faster rate fill engraving path (3” per second), which removed all foam material within the perimeter engraving path. Molds for each slice could be created in approximately ten minutes using this technique. A finished foam mold is shown in Figure 2-4.

After engraving was completed, the molds were checked to ensure that all areas to be filled with STES were connected to aid in future placement. In cases where an area to be filled with STES was surrounded by bone or lung, small grooves were cut in the mold with a razor blade in order to connect the soft tissue island to the main body of the slice. This is similar to a stencil where the center of the letter “O” must be joined with thin connectors to ensure proper orientation. Finally, the job time for each slice was recorded. The job time and feed rate was used to determine the approximate volume/weight of soft tissue equivalent material needed for each slice.

Introduction of soft tissue

Depending on how many soft tissue molds were being filled at a time, an appropriate amount of the urethane based STES was mixed and immediately poured into the soft tissue molds. This was done fairly rapidly (less than 30 minutes) as the STES began setting

immediately. The filled molds were covered with waxed paper and any trapped air pockets were relieved by making small slits in the waxed paper with a razor blade. A straight edge was then passed along the surface of the mold to remove any excess STES and force it out of the mold, allowing the slices to cure at the correct thickness (5 mm). After roughly three hours, the waxed paper was removed from the partially cured soft tissue slices. It is important to remove the waxed paper prior to the STES fully curing; otherwise, the STES would bond to the waxed paper and it could not be easily removed. After 24 hours, the soft tissue slice could be removed from the mold.

Introduction of bone tissue

The method of introducing bone into the soft tissue slices was analogous to that of Jones et al.⁶³ First, the bottom of each soft tissue slice was sealed using contact paper to prevent any uncured BTES from running under the slice. Any soft tissue island connectors were then removed using a razor blade. An appropriate amount of BTES was mixed to fill the voids in the soft tissue slices that were left for bone tissue. A heat gun was used to warm the BTES material in order to reduce its viscosity and make it easier to mix and pour. The BTES material was then placed in a pastry bag including a pastry tip (#12) and forced into the appropriate voids in the soft tissue slices, taking care to avoid creating any air pockets during the pouring. Air pockets that were trapped during bone insertion would typically rise to the surface, where they could be pierced and eliminated. Bone locations were slightly overfilled because it was found easier to remove excess bone than to add additional bone after curing. The segmented data set was referenced to avoid accidentally filling any voids intended to contain air. The BTES was allowed to cure for 48 hours. Finally, the contact paper masks were removed and the bone locations within each phantom slice were sanded flush with the soft tissue using a belt sander with an 80

grit belt. Figure 2-5 shows a completed slice which includes the STES, LTES, and BTES materials integrated into an axial slice of the phantom.

Phantom assembly

Once all the phantom slices were completed, the organs and locations of dosimetric importance were selected. Full-scale axial printouts of the segmented images were used to trace and label the organs of interest onto the physical phantom slice using a permanent marker (see Figure 2-5). Phantom slices containing locations of dosimetric interest were left unattached to a bordering slice in order to allow access for dosimeter insertion. All other slices were bonded to adjacent slices using commercially available wood glue. The glue was placed uniformly over all areas of a slice surface with the exception of air spaces. Wood glue has been found to behave radiologically similar to soft tissue at diagnostic energies.⁶³ Bonding slices of the phantom into sections permits easy disassembly/reassembly of selected portions of the completed phantom. During assembly, slices were aligned using registration marks and then glued together sequentially. After assembly was completed, excess wood glue and registration marks were removed with a razor blade.

Introduction of lung tissue

Rather than pouring the lung tissue into the each individual soft tissue slice, the LTES was introduced into the phantom after it had been glued together into sections. Each section requiring LTES was first prepared by masking off the bottom of the section with contact paper to prevent the lung tissue from escaping the voids. An adequate amount of LTES was then prepared and introduced into the voids. Unlike the STES, the LTES is not fluid and has a consistency similar to a light paste (i.e. cake frosting), therefore a wooden spoon was utilized to force the LTES into all of the corners of the lung void, working from the center of the lung and outwards towards the

perimeter. If a section was accidentally overfilled with LTES, the excess could easily be removed during introduction or sanded smooth later after curing.

Results

Materials

Soft tissue-equivalent substitute

The STES was empirically evaluated using an x-ray source (3.9 mm Al HVL at 80 kVp) to have an HVL of 25 mm at 80 kVp, and 29 mm at 120 kVp. The measured density was 1.04 g/cm³. The average HU for the STES material was found to be 9.8, at the lower end of the widely accepted range for human muscle (10-40 HU). However, the measured value is considered acceptable because STES represents a homogenized mixture of both muscle and adipose tissue, with the latter having a HU range of -50 to -100.

Lung tissue-equivalent substitute

The density of the LTES was measured to be 0.33 g/cm³, agreeing well with the targeted lung density at full inspiration. The average HU for the LTES material is -678.4, consistent with widely accepted HU values for lung, which range from -500 to -1000.

Bone tissue-equivalent substitute

The BTES has been previously characterized⁵⁴ and empirically evaluated to have an HVL of 9.8 mm at 80 kVp and 13.3 mm at 120 kVp. The BTES material had an average HU of 622. This result is consistent with widely accepted HU values of bone, which range from 400 to 1000.

Completed Phantom

The torso of the completed 50th percentile adult male phantom is shown in Figure 2-6. Although not pictured, the phantom also includes a pelvis section which extends to mid-thigh. Surface markings seen on all phantoms (black markings) refer to slice number and were used

during the assembly process to keep slices in order. Also, the arms can easily be removed for imaging procedures where they are usually placed out of the primary radiation field.

Discussion

The urethane based STES has numerous advantages over the epoxy resin based soft tissue substitute originally proposed by Jones et al.⁵⁴ First, it is much less viscous than the epoxy resin soft tissue substitute, making it easier to pour into the foam molds. Once cured, it is also easily removed from the foam molds; this is not the case with the epoxy resin materials which do not release from the molds cleanly. Additionally, it requires fewer modifying constituents than epoxy resin based tissue equivalents, and therefore retains better homogeneity. The urethane based STES remains pliable and strong when cured, while the epoxy resin soft tissue substitute is brittle when cured and can break under stress or when dropped. Because of these properties, the urethane based material is more durable and unlikely to be damaged with use. Finally, STES better accommodates the insertion of FOC dosimeters, only requiring a thin slit to be cut into the material to allow passage of the optical fiber that connect the active regions of the detector to a read-out device; this avoids any potential concerns about radiation streaming along machined dosimeter channels.⁶³

Creating molds resulting in a uniform 5 mm thick phantom slices proved more challenging than expected. Early on, molds would occasionally display a variation in cutting depth throughout the slice. The engraving system hardware and software was initially suspected and investigated. However, it was found that this variation in cutting depth was the result of the foam template bowing upwards and losing adhesion to the engraving table during the milling process. This problem was corrected by using additional tape to hold the foam blank in place as it was being milled and replacing the tape regularly to avoid loss of adhesion.

Conclusions

A unique methodology has been developed to construct anthropomorphic phantoms for use in dosimetry studies. While the value of this methodology has already been proven with the construction of this phantom, it should be noted that the same methodology could be applied to the construction of phantoms of all sizes and ages. In particular, our group plans to develop a family of phantoms that accurately represent patients of differing heights and weights. Future works also include the investigation of an adipose tissue-equivalent substitute which could be added to the existing phantoms, or included as an additional step in the construction of a new phantom, to represent subcutaneous fat in order to accurately model more obese patients.

While anthropomorphic phantoms have many potential applications, this particular phantom was created to quantify organ doses from cone-beam CT procedures. It is anticipated that other institutions could create their own phantoms for dosimetry studies by following the methodology presented here and using the described tissue equivalent materials for a total material cost of less than \$3500. However, equipment and labor costs must also be taken into consideration, with an initial equipment investment of approximately \$10000 and labor on the order of several hundred hours per phantom.

Table 2-1. ICRP 103 organs of interest for the calculation of effective dose and their associated weighting factors

Tissue	w_T
Bone-marrow (red), Colon, Lung, Stomach, Breast, Remainder tissues*	0.12
Gonads	0.08
Bladder, Oesophagus, Liver, Thyroid	0.04
Bone surface, Brain, Salivary glands, Skin	0.01

*Remainder tissues: Adrenals, Extrathoracic (ET) region, Gall bladder, Heart, Kidneys, Lymphatic nodes, Muscle, Oral mucosa, Pancreas, Prostate (male), Small intestine, Spleen, Thymus, Uterus/cervix (female).

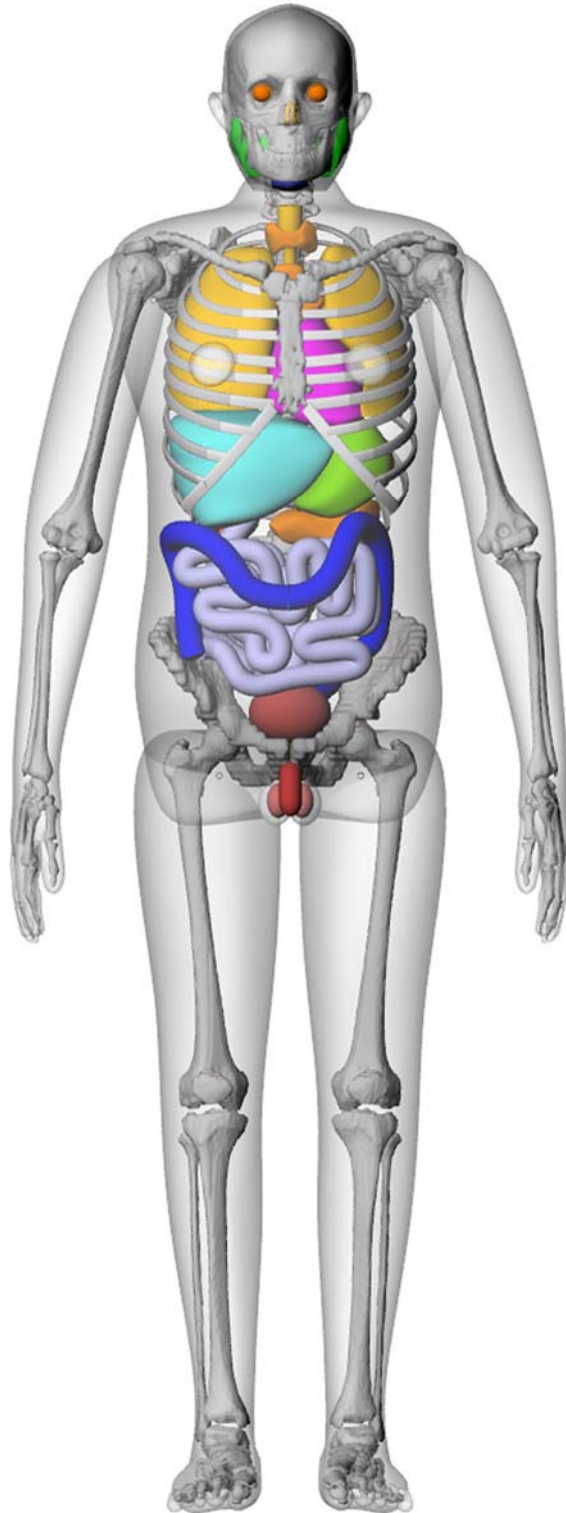


Figure 2-1. Completed 50th percentile hybrid computational phantom



Figure 2-2. Axial image with segmented organs from the hybrid computational phantom



Figure 2-3. A finished bitmap image ready to be imported into the milling software showing only soft tissue (grey) and voids (white). Anterior and lateral registrations marks were also added to aid in assembly.



Figure 2-4. Finished soft tissue mold, ready to be poured with STES material.

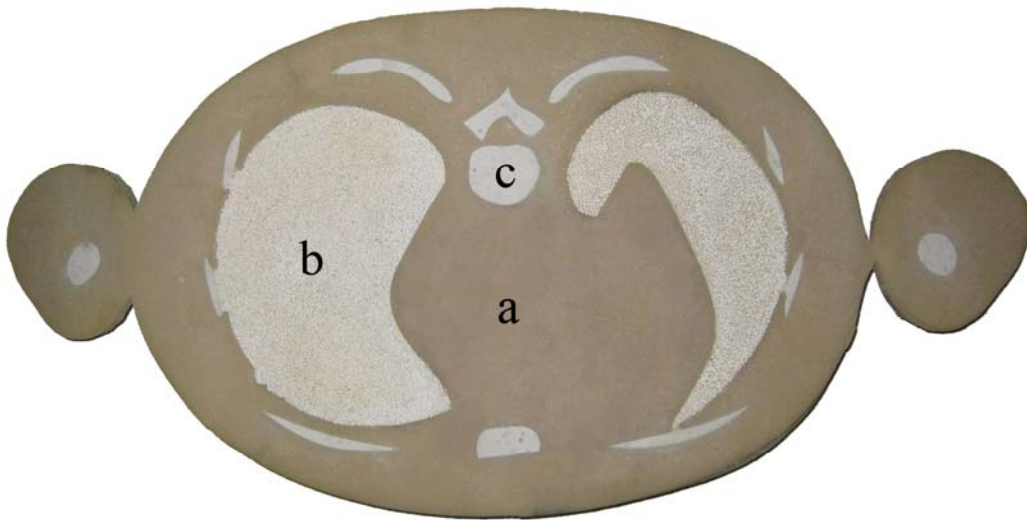


Figure 2-5. Completed axial slice with a) STES, b) LTES, and c) BTES



Figure 2-6. Torso of completed 50th percentile physical phantom

CHAPTER 3
CONSTRUCTION AND CHARACTERIZATION OF A WATER-EQUIVALENT FIBER
OPTIC COUPLED DOSIMETER FOR USE AT DIAGNOSTIC ENERGIES

Introduction

Interest in accurately quantifying the absorbed dose at diagnostic energies by performing in-phantom or in vivo dose measurements has prompted the development of a new fiber optic coupled (FOC) dosimeter. The FOC architecture was chosen due to its small size and ability to provide real-time dose information during irradiation. Other dosimeters commonly used at diagnostic energies, such as ionization chambers, thermoluminescent dosimeters (TLDs), or optically stimulated luminescent (OSL) dosimeters are either too large to incorporate into phantoms or require a time consuming reading process after irradiation to extract dose information. Additionally, TLDs have shown an angular dependence of up to 20%,⁶⁴ while OSLs have shown degradation with repeated exposures.⁶⁵ Metal-oxide field-effect transistors (MOSFETs) have also been investigated for use at diagnostic energies, but reproducibility variations as high as 15-30%⁶⁶ between measurements, along with metallic components which can lead to image artifacts, have limited their success. Lastly, diode detectors have been investigated but are too large for in-phantom measurements and suffer from an over-response to low energy photons when compared to an ion chamber and an angular dependence as great as 50%.⁶⁷ The over-response to low energy photons is of particular concern because low energy scatter inside a phantom could lead to inaccurate dose measurements when utilizing such a system for in-phantom dosimetry. It is important to note, however, that this characteristic is not unique to diode detectors. Any detector composed of high-Z materials, including TLDs, OSLs, and MOSFETS, will over-respond to low energy photons in the diagnostic spectra due to the strong atomic number dependence of radiation interactions (mainly photoelectric) at these energies.

FOC dosimeters, utilizing a variety of sensitive elements, have seen some success in both diagnostic and therapeutic applications. They overcome many of the shortfalls of other dosimeter systems by showing little angular dependence, no detectable performance degradation over time, high reproducibility, and real-time output while maintaining a small physical size that allows measurements with high spatial resolution. In diagnostic and mammographic applications, FOC dosimeters utilizing a copper-doped quartz sensitive element have been utilized, but calibration and reproducibility concerns remain.^{68, 69} In therapeutic applications, FOC dosimeters utilizing a water-equivalent plastic scintillator as the sensitive element have been used, along with gating or filters to eliminate the effects of Cerenkov radiation, for dose verification in several applications.^{70, 71}

This work extends the use of water-equivalent plastic scintillator based FOC dosimeters to diagnostic applications, where energies are low enough (less than 190 keV for silica) that the production of Cerenkov radiation in the optical fiber is not a concern.⁷² Plastic scintillation material was chosen as the sensitive element of the FOC dosimeter in this study for two primary reasons: an adequate light output to maintain a high signal-to-noise ratio and a water-equivalent effective-Z. The water-equivalent effective-Z prevents image artifacts and mimics the radiation interaction properties of soft tissue, eliminating the over-response to low energy photons and producing an energy dependence that allows for easy and effective calibration.

The FOC dosimeter was constructed by coupling a small cylindrical plastic scintillator, 500 μm in diameter and 2 mm in length, to a 2 meter long optical fiber, which acts as a light guide to transmit scintillation photons from the sensitive element to a photomultiplier tube (PMT). A serial port interface on the PMT permits real-time monitoring of dosimeter output via a custom computer program. To allow multiple FOC dosimeters to be monitored simultaneously,

an array of 5 PMTs was constructed. The end result of this work is a multichannel fiber optic coupled dosimetry system capable of accurately measuring in-phantom doses in the diagnostic energy range with real-time resolution.

Methods and Materials

FOC Dosimetry System

The sensitive element of the FOC dosimeter consists of a water-equivalent plastic scintillator (BCF-12, Saint-Gobain Crystals, Nemours, France) in the shape of a cylinder with a diameter of 500 μm and a length of 2 mm. The peak emission wavelength of the scintillating element is in the visible spectrum at 435 nm. To transmit the scintillation photons from the sensitive element to a photomultiplier tube (PMT), the scintillator was mechanically coupled to an unjacketed optical fiber (400-UV, Ocean Optics Inc., Dunedin, FL) with a diameter of 400 μm and a length of 2 m (referred to as the signal fiber) using a short piece (~ 1 cm) of heat shrink tubing. To maximize the number of scintillation photons reaching the PMT, the coupled end of both the scintillator and signal fiber were polished, as suggested by Ayotte et al.,⁷³ with progressively finer lapping films (12, 3, and 1 μm). The uncoupled end of the scintillator was similarly polished and then coated with a reflective paint (EJ-510, Eljen Technology, Sweetwater, TX) in order to prevent the escape of scintillation photons, effectively increasing the output of the sensitive element.⁷⁴ At the opposite end of the optical fiber, a female SMA 905 connector (SMA-490, Ocean Optics Inc., Dunedin, FL) was installed to enable the FOC dosimeter to be connected with a PMT. Lastly, the entire FOC dosimeter was wrapped in opaque heat shrink tubing to restrict ambient light and add strength to the assembly. A completed FOC dosimeter is shown in Figure 3-1 and a close up of the scintillating end of the dosimeter is shown in Figure 3-2.

While the majority of the light reaching the PMT is a result of photons released from the sensitive element of the FOC dosimeter, a fraction of the light is a result of the native fluorescence within the optical fiber itself.^{70, 75} The fluorescence of the optical fiber is commonly referred to as the stem effect, and if not accounted for can result in significant errors in dose measurements. In order to account for this effect, a reference fiber, consisting of a second optical fiber without a sensitive element, was also constructed. For the purposes of this study, the reference fiber was placed next to the signal fiber during all exposure measurements and the stem effect was measured and subtracted from the signal fiber. As used in this study, the reference fiber typically accounted for less than 10% of the total counts measured via the signal fiber. While the use of a reference fiber effectively accounts for the stem effect, it was found to be cumbersome when performing dose measurements. This problem was solved by incorporating the reference fiber into the same heat shrink tubing that houses the signal fiber; resulting in a smaller overall package. A completed dosimeter is shown in Figure 3-3.

To facilitate the simultaneous reading of multiple FOC dosimeters, an array of 5 photon counting PMTs (H7467, Hamamatsu Corporation, Bridgewater, NJ) was fabricated. The H7467 PMTs were chosen as they offer a spectral response from 300 to 650 nm with a peak efficiency at 420 nm, coinciding well with the wavelength of emission of the scintillating element. While only one FOC dosimeter was used for this study, the capability of reading multiple dosimeters simultaneously will greatly increase the speed of data collection for future work such as anthropomorphic phantom organ dose measurements. To limit the number of spurious pulses detected due to scattered x-rays reaching the PMTs and causing photocathode emissions, the box housing the PMT array was lined with 1/16" lead shielding. A male SMA optical fiber adapter (E5776-51, Hamamatsu Corporation, Bridgewater, NJ) was also fitted to each PMT to enable

connection with an FOC dosimeter. Counting data from each PMT was routed through a serial-to-USB hub (UPort 1610-8, Moxa Inc., Brea, CA) via RS-232 cables and subsequently transferred from the hub to a laptop computer via a USB cable. A custom MATLAB® (Mathworks Inc., Natick, MA) computer program, discussed in the next section, was developed to interface with the PMT array and provide real-time monitoring of dosimeter output. A simplified schematic of the entire FOC dosimetry system is shown in Figure 3-4. Components not shown include a 5 V DC power supply for the PMT modules and a 12 V DC power supply for the serial-to-USB hub.

PMT Control Program

The computer program developed to interface with the PMT array was written and tested in MATLAB Release 2007a. The purpose of the program was to establish a two-way connection with each PMT for the purpose of sending and receiving information such as instructions and counting data. To aid the end user in operating the computer program, a graphical user interface (GUI) was developed using the built in MATLAB “guide” tool. A screenshot of the finished GUI is shown in Figure 3-5. The GUI features buttons to start and stop counting, a button to save the counting data to a tab delimited text file, and a button to disconnect from the PMT array and close all serial port connections. Radio buttons to select which PMTs to initialize are also displayed along with text box that allows the user to manually enter an integration time for the PMTs. An integration time between 10 ms and 10 s can be entered depending on the desired time resolution for the experiment being conducted. Below the control buttons, the GUI graphically displays the output from each PMT in real-time along with a numerical display of counts per integration time and a running sum of the total counts. Through calibration, the total counts can be equated to dose and therefore the FOC dosimetry system operates as a relative dosimeter.

Exposure Measurements

Unless otherwise noted, the characterization of the FOC dosimeter was performed using a clinical x-ray tube with a measured half value layer of 5.76 mm of Al at 120 kVp and a fixed field size of 20x20 cm. All testing, except for the angular dependence which was done free-in-air, was performed with the dosimeter placed on top of a polymethylmethacrylate (PMMA) slab to provide a backscatter medium. All measurements were repeated 5 times to reduce statistical uncertainties and provide reproducibility metrics. A 15 cm³ pancake ion chamber and associated electrometer (chamber model 96035B, electrometer model 35050A, Keithley Instruments Inc., Cleveland, OH) were used to provide simultaneous exposure measurements.

It should be noted that all results reported in this study have been corrected for the stem effect with the use of a reference fiber. A calibration between the PMT used for the signal fiber and the PMT used for the reference fiber was also performed to eliminate the influence of sensitivity differences between the two PMTs.

Energy Dependence

The energy dependence of the FOC dosimeter was evaluated by incrementally increasing the tube potential from 40 to 120 kVp in 10 kVp increments while maintaining the current-time product constant at 50 mAs. The ion chamber was placed next to the FOC dosimeter and irradiated simultaneously to provide a reading of the air kerma from each exposure. These data were then used to plot the normalized dosimeter sensitivity, in counts/mGy, versus tube potential.

To evaluate the effect of varying beam quality as a function of tissue depth due to beam hardening and scattering, varying thicknesses of soft tissue-equivalent material⁵⁵ were placed on top of both the FOC dosimeter and ion chamber and exposures were taken at 120 kVp and 50 mAs with a fixed field size of 10x10 cm. These data were then used to create a plot of the

normalized dosimeter sensitivity, in counts/mGy, versus depth in the soft tissue-equivalent material.

Linearity

The linearity of the FOC dosimeter was evaluated by increasing the current-time product from 0.5 mAs to 160 mAs while keeping the tube potential constant at 120 kVp, yielding air kerma values ranging from 0.16 to 57.29 mGy. The current-time product was initially varied by holding the exposure time constant and adjusting the tube-current. Unfortunately, the entire dose range desired could not be achieved with a single exposure time setting, and therefore several different exposure times were utilized (20, 50, 100, 200, and 320 ms). By holding the exposure time constant when possible, the dose rate was effectively varied and therefore the results also indicate the dose rate linearity of the FOC dosimeter. A linear fit was applied to a plot of the FOC dosimeter's counts versus measured air kerma and the correlation coefficient was used to quantify the linearity of the dosimeter.

Reproducibility

The reproducibility of the FOC dosimeter was evaluated using the data from the linearity experiment. Because each measurement was repeated 5 times, the data provided an adequate sample from which to take average readings and standard deviation for different exposure levels of interest in diagnostic radiology. The coefficient of variation (COV) at each exposure level was calculated to quantify the dosimeters reproducibility.

Dosimeter Response versus Bend Radius

The change in response of the FOC dosimeter as the optical fiber was bent to various radii was also investigated. Technique settings were fixed at 120 kVp and 50 mAs. The dosimeter was first irradiated with the optical fiber straight to obtain a baseline value. The dosimeter was then irradiated with the optical fiber bent into a single loop 20 cm in radius at a distance of 40 cm

from the sensitive element of the dosimeter. Measurements were repeated with progressively smaller loop radii (10 cm, 7.5 cm, 4 cm, and 2.5 cm) to fully characterize the response of the dosimeter versus bend radius of the optical fiber.

Angular Dependence

The angular dependence of the FOC dosimeter was evaluated using a clinical computed tomography (CT) unit with a half value layer of 7.0 mm of Al at 120 kVp. Static shots at fixed tube angles were taken with technique settings of 120 kVp and 5 mAs. A CT unit was chosen for this testing because it provided an easy method of accurately obtaining the response of the dosimeter as a function of angle of incident radiation. The dosimeter was first placed at the isocenter of the unit free-in-air with the patient table out of the beam and irradiated axially (around the cylindrical axis of the dosimeter). Measurements were made at intervals of 30 degrees all the way around the dosimeter. The dosimeter was then turned and irradiated normal-to-axial where 0° corresponds to x-rays incident on the tip of the dosimeter and 180° corresponds to x-rays incident from the backside of the dosimeter. Again, measurements were made at intervals of 30 degrees.

Results

Energy Dependence

Figure 3-6 plots the normalized sensitivity of the FOC dosimeter, in counts/mGy, as a function of tube potential. The results were normalized to the measurement point at 120 kV for ease in comparison. As can be seen, the energy response is fairly linear and the sensitivity of the FOC dosimeter increases an average of 6.8 % per 10 kVp across the energy range shown.

Additionally, Figure 3-7 plots the normalized sensitivity of the FOC dosimeter, in counts/mGy, as a function of depth in soft tissue-equivalent material. The results were normalized to the surface measurement point, which corresponds to the 120 kV measurement

point in Figure 3-6, for ease in comparison. As the depth increases, the x-ray spectrum changes due to beam hardening and the addition of a scatter component. This effect causes the sensitivity of the dosimeter to vary due to its energy dependence. However, the variation is only 10% across the depth range investigated.

Linearity

Figure 3-8 plots the response of the FOC dosimeter, in counts, as a function of air kerma, in mGy. Error bars are not shown because they were too small to be displayed. A linear trend line was fitted to the data and the correlation coefficient was found to be 1.000. This result demonstrates that the FOC dosimeter has a very linear response over the exposure range of interest in diagnostic radiology.

Reproducibility

Table 3-1 summarizes the average readings and standard deviation, in counts, over the exposure range of interest commonly used in diagnostic radiology. The coefficient of variation was less than 1% for most exposure levels, demonstrating that the FOC dosimeter is capable of highly reproducible readings. As expected, the variation was slightly higher at low exposure levels due to less total counts and more fluctuations between readings. However, the coefficient of variation was only 3.64% for even the lowest exposure level (0.16 mGy).

Dosimeter Response versus Bend Radius

Figure 3-9 plots the response of the FOC dosimeter as the optical fiber was bent into a single circular loop with progressively smaller radii. The response was normalized to the measurement point in which the optical fiber was straight for ease of comparison. The response of the dosimeter remained relatively constant for large bend radii and did not decrease significantly (> 10%) until a small radius of 2.5 cm was obtained.

Angular Dependence

Figures 3-10 and 3-11 plot the response of the FOC dosimeter to an axial and normal-to-axial irradiation free-in-air, respectively. All data was normalized to a 0° axial irradiation for ease of comparison. For the normal-to-axial data, 0° corresponds to x-rays incident on the distal tip of the dosimeter and 180° corresponds to x-rays incident from the backside of the dosimeter (see schematic in Figure 3-11). As expected due to the cylindrical geometry, the response of the dosimeter showed little angular dependence to an axial irradiation, varying by less than 5% over an entire revolution. The response of the dosimeter to a normal-to-axial irradiation showed a reduction of 97% in the number of counts detected when the x-rays were incident through a narrow range of angles directly from the back of the dosimeter (180°). A slight reduction in recorded counts of approximately 12% was also seen when radiation was incident on the face of the dosimeter (0°).

Discussion

The FOC dosimeter showed excellent dose linearity and reproducibility when benchmarked against an ion chamber. Additionally, there was minimal reduction in dosimeter response as the optical coupling fiber connecting the scintillator to the PMT was bent into loops of decreasing radius. At a bend radius of 2.5 cm a significant reduction was seen, but such a tight bend radius is far beyond the range expected to be encountered with normal use of the FOC dosimetry system.

The FOC dosimeter exhibited positive energy dependence in the range of tube potentials evaluated (40-120 kVp). Initially, it was thought that energy or beam quality dependent calibration factors could be used to simply correct for this effect. However, it was later realized that when using the dosimeter for in-phantom dosimetry, depth-dependent correction factors may also be needed to account for the energy dependence of the dosimeter due to variations in beam

quality at increasing depths as a result of beam hardening and the addition of a scatter component. The need for depth-dependent correction factors was evaluated, as shown in Figure 3-7, and it was found that the sensitivity of the dosimeter varied by only 10% over the depth range investigated. Much of this variation occurred between the free-in-air measurement (depth = 0) and the first data point in tissue, suggesting that the dosimeter could be calibrated under only a few cm of scattering medium to minimize the effect of the dosimeters energy dependence for in-phantom dose measurements. It should be noted that specific irradiation geometries and conditions should be evaluated similarly in order to determine the extent to which changes in the beam energy spectrum could affect the dosimeter's calibration. Also, this issue is not unique to only the FOC dosimetry system, but applies to many dosimeters commonly used in diagnostic measurements (TLDs, OSLs, MOSFETs, and diodes for example); though the issue is seldom investigated or accounted for in the current literature.

The angular dependence of the FOC dosimeter was evaluated for both axial and normal-to-axial irradiation. Due to the cylindrical geometry of the dosimeter, little angular dependence was expected from an axial irradiation. Figure 3-10 demonstrates this result, showing that the dosimeter's response varied by less than 5% over an entire revolution. This small amount of variation can be attributed to the construction of the dosimeter, as it is technically difficult to ensure that the sensitive element is perfectly aligned with the optical fiber. Because angular dependence is a function of the alignment of the sensitive element, each dosimeter should be characterized prior to its initial clinical use. The response of the dosimeter to a normal-to-axial irradiation showed a reduction in counts of 97% when irradiated from the backside due to attenuation of x-rays by the optical fiber itself. Additionally, the response of the dosimeter dropped by 12% when radiation was incident on the distal tip of the dosimeter. This reduction is

attributable to the smaller solid angle provided by the cylindrical geometry of the sensitive element when viewed head on. The variations in detector response can be minimized in projection radiography with proper orientation of the dosimeter. In CT dosimetry, the effects of these variations will likely be averaged out for in-phantom measurements due to the rotation of the x-ray tube. In order to illustrate this point, the area under the curve shown in Figure 3-11 was found to be only 11% less than that of an ideal detector response with no angular dependence. In addition, the presence of scatter radiation has been found to reduce the effects of angular dependence in in-phantom dose measurements.⁷⁶

Conclusions

The FOC dosimeter described in this study offers immediate readout, excellent sensitivity, linear dose response, and high reproducibility in a physical package that is small enough to be used for in-phantom or in vivo dose measurements. Additionally, the FOC dosimeter showed no significant decrease in response as the optical fiber was bent for radii commonly seen during clinical use. Drawbacks of this dosimeter include positive energy dependence and a decrease in response for irradiations incident from the back of the dosimeter. However, the energy dependence is minimized by calibrating the dosimeter under several cm of material to account for changing beam quality with depth due to beam hardening and scattering. Variations in angular response can be minimized by proper orientation of the dosimeter in projection radiography and will be negligible for in-phantom measurements in CT imaging as variations will be reduced by the presence of scatter radiation and the rotation of the x-ray tube. Overall, the FOC dosimetry system provides rapid and accurate dose measurements applicable to a range of diagnostic imaging applications, with particular utility for in-phantom organ dose measurements. For the purposes of this research, the FOC dosimeter described above and the

anthropomorphic phantom described in Chapter 2 will be used to quantify organ doses from kilovoltage CBCT.

Table 3-1. Reproducibility of measurements with FOC dosimeter at kV energies

Air kerma (mGy)	Mean counts (net)	Standard deviation	COV (%)
0.16	1315	48	3.64%
0.30	2523	58	2.30%
0.60	4895	50	1.03%
1.46	11891	107	0.90%
2.85	22076	280	1.27%
5.76	45405	290	0.64%
8.91	67768	491	0.72%
17.96	135556	247	0.18%
35.81	270178	1046	0.39%
57.29	431655	2862	0.66%

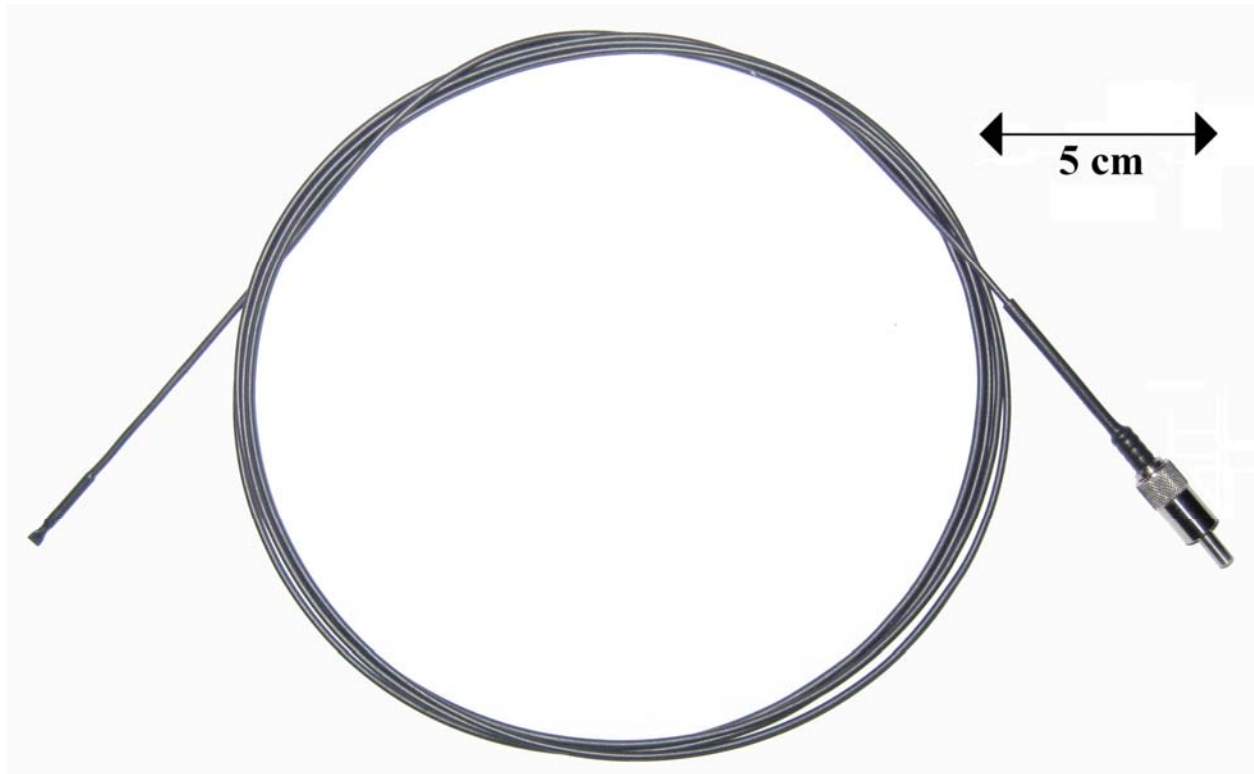


Figure 3-1. Completed FOC dosimeter. Scintillating element at left and SMA connector at right.



Figure 3-2. Close up of scintillating element end of dosimeter. Area of increased diameter at distal tip is due to underlying heat shrink tubing that was used to couple the scintillating element to the optical fiber. Exterior sheath of heat shrink tubing is crimped off at distal tip to prevent ambient light from entering assembly.

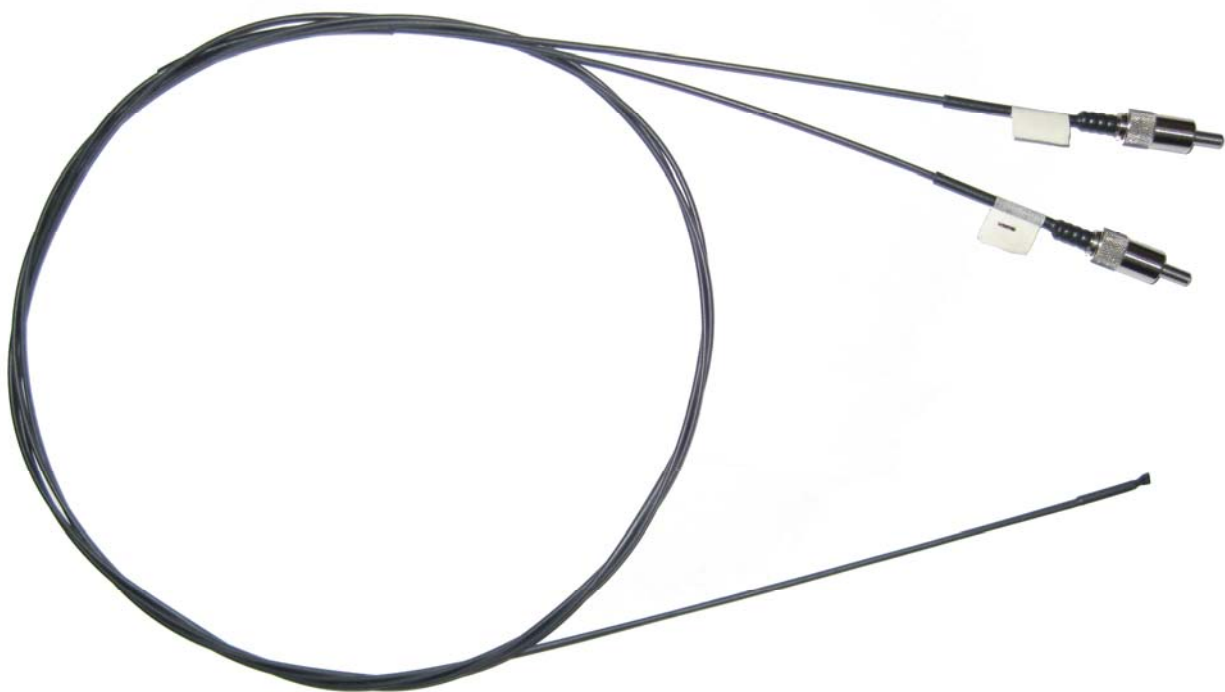


Figure 3-3. New dosimeter design with reference fiber incorporated into FOC dosimeter assembly.

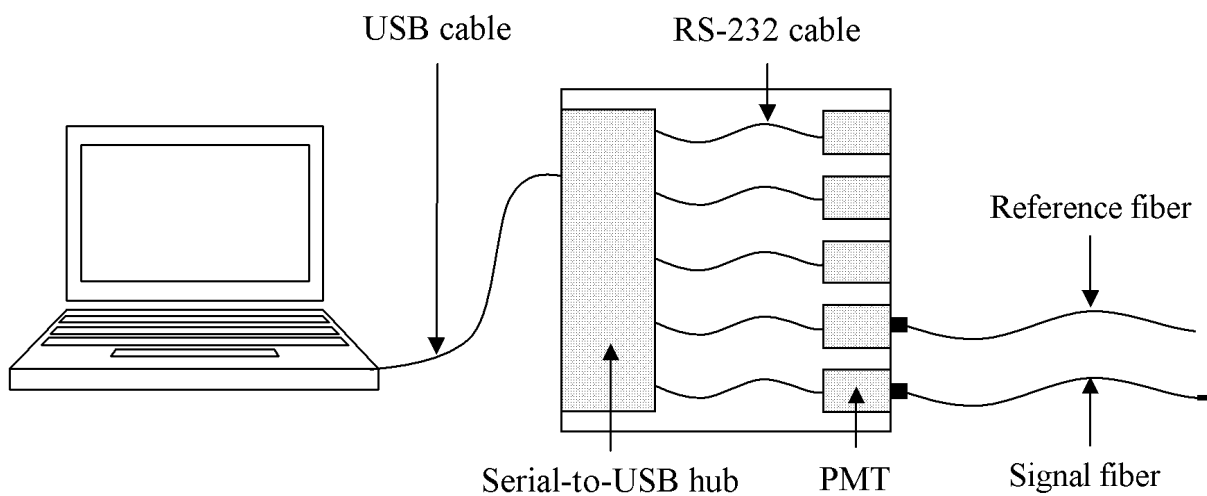


Figure 3-4. FOC dosimetry system schematic, power supplies for serial-to-USB hub and PMTs not shown.

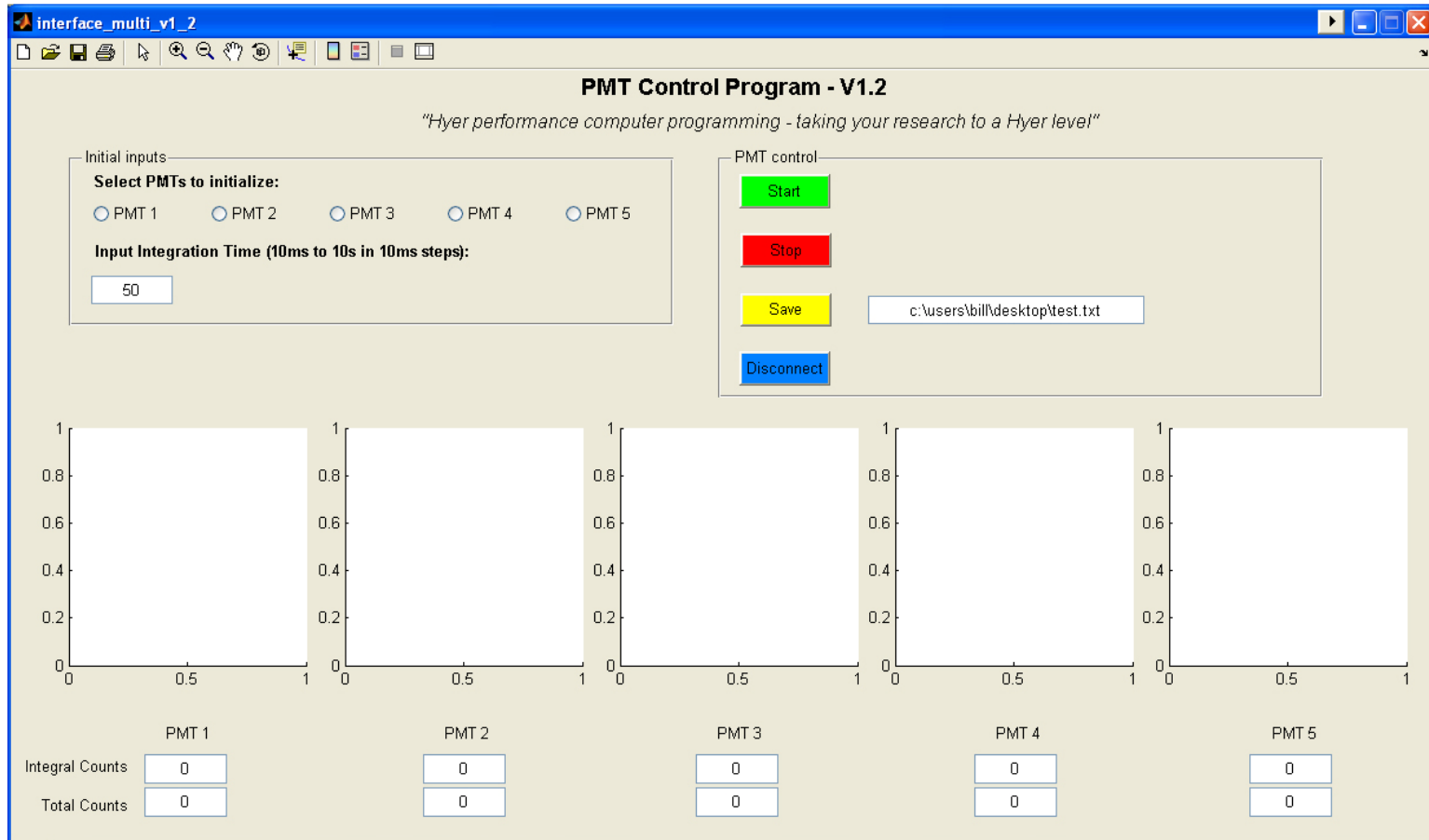


Figure 3-5. Screenshot of PMT control program GUI. Program allows user to select which PMTs to initialize, input an integration time, start and stop counting, save the counting data to a tab delimited text file, and disconnect from the PMT array which closes all serial port connections. Displays counting data from each PMT in real-time both graphically and numerically.

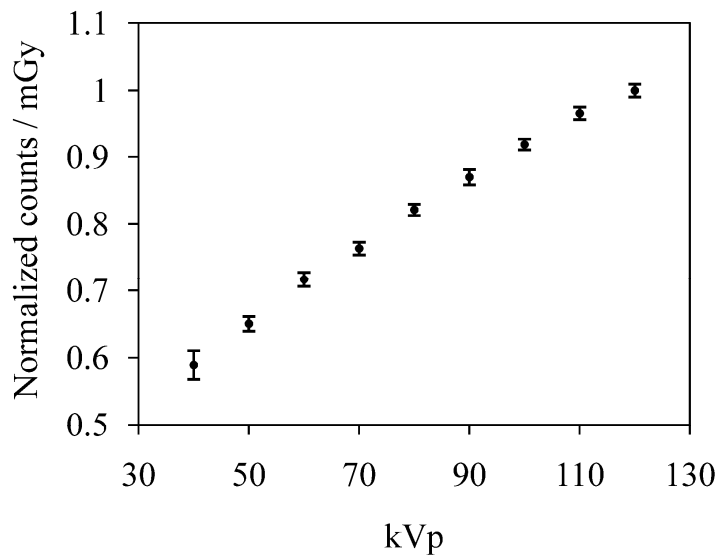


Figure 3-6. Energy dependence of FOC dosimeter. Data has been normalized to the data point at 120 kV. Error bars correspond to ± 1 standard deviation of the mean.

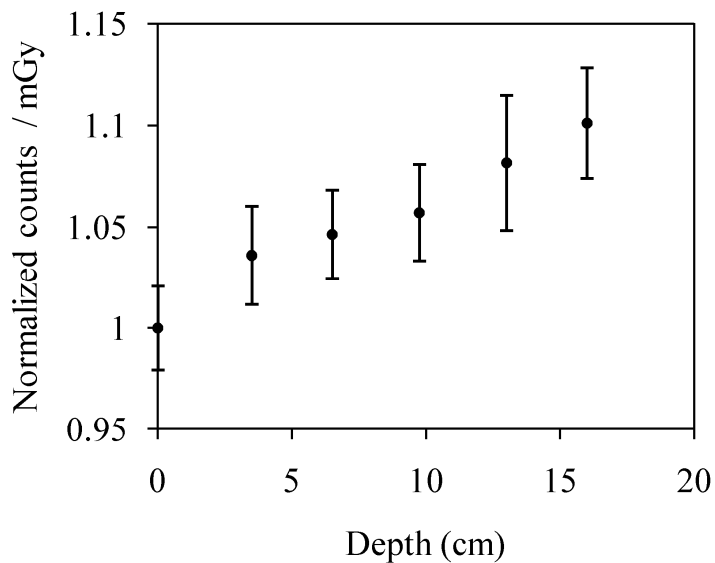


Figure 3-7. Energy dependence of FOC dosimeter as a function of depth in soft tissue-equivalent material. Data has been normalized to the surface measurement (depth = 0), which corresponds to the 120 kV measurement in Fig. 3. Error bars correspond to ± 1 standard deviation of the mean.

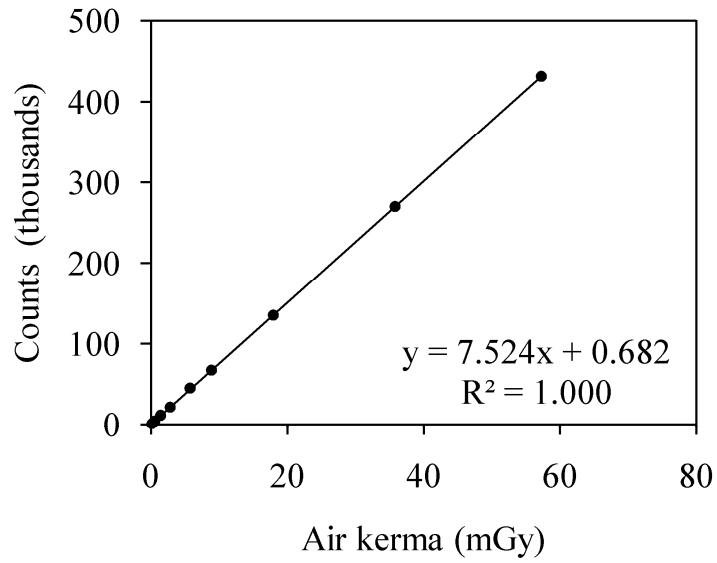


Figure 3-8. Dose linearity of FOC dosimeter.

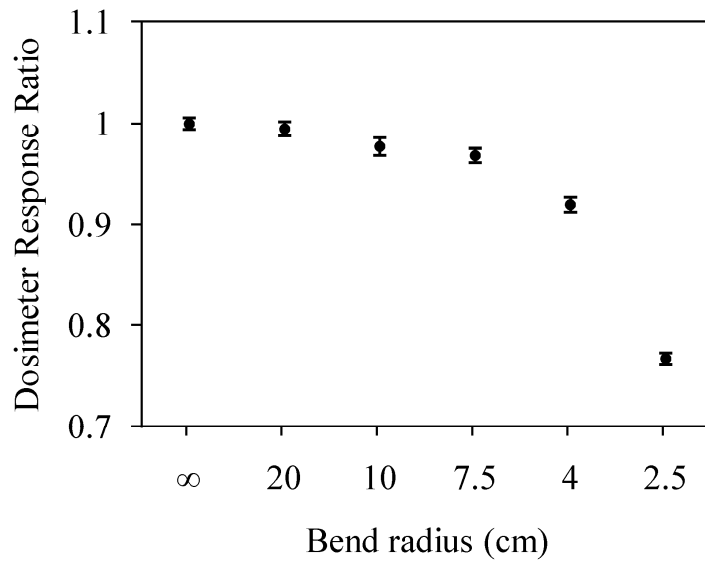


Figure 3-9. Response of FOC dosimeter versus the bend radius of the optical fiber. Data has been normalized to a bend radius of infinity. Error bars correspond to ± 1 standard deviation of the mean.

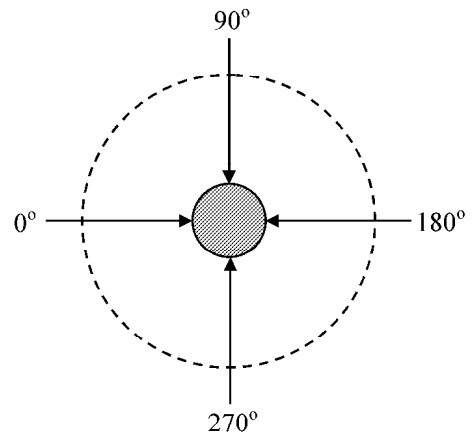
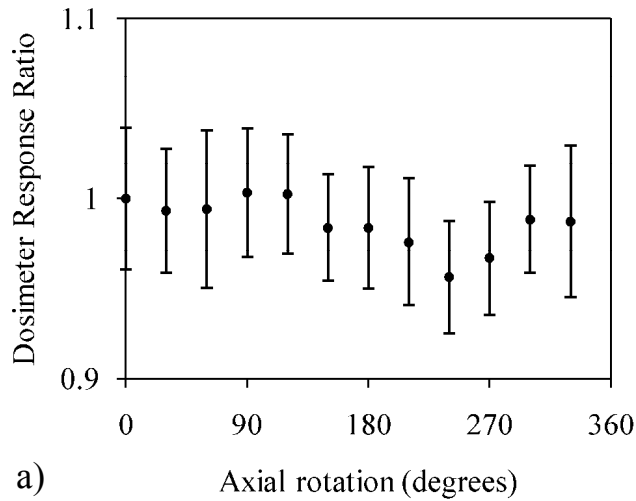


Figure 3-10. Angular dependence of FOC dosimeter to an axial irradiation. A) Response data has been normalized to a zero-degree axial angular response. Error bars correspond to ± 1 standard deviation of the mean. B) Experimental setup, shaded area represents a head on view of the sensitive element of the FOC dosimeter.

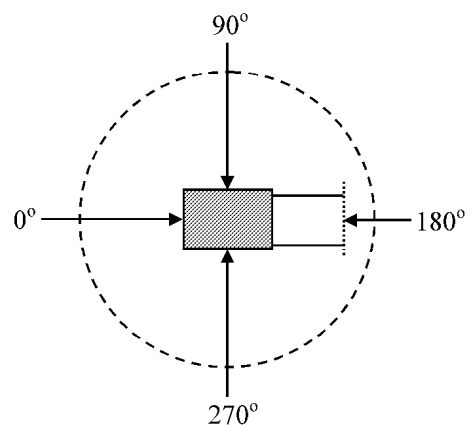
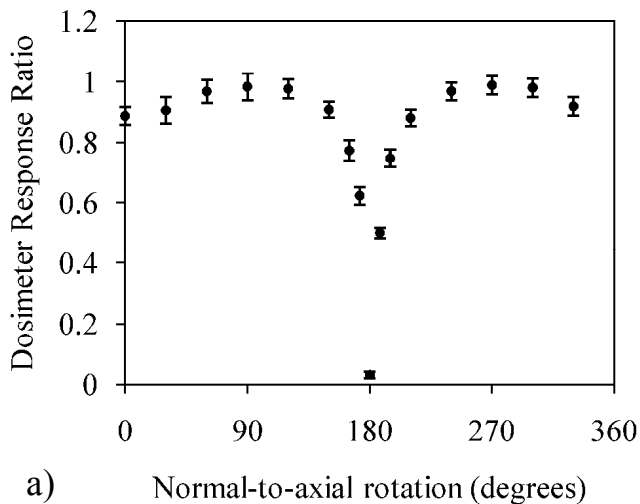


Figure 3-11. Angular dependence of FOC dosimeter to a normal-to-axial irradiation. A) Response data has been normalized to a zero-degree axial angular response. Error bars correspond to ± 1 standard deviation of the mean. B) Experimental setup, shaded area represents a side view of the sensitive element of the FOC dosimeter.

CHAPTER 4 CHARACTERIZATION OF THE FIBER-OPTIC COUPLED DOSIMETER AT MEGAVOLTAGE ENERGIES

Introduction

In the previous chapter, the fiber-optic coupled (FOC) dosimeter was characterized at diagnostic energies. The results from this study were very positive and a working version of the dosimeter and PMT array for dose measurements at diagnostic energies is now available. This was an important milestone as the remainder of this research relies on using the FOC dosimeter to perform organ dose measurements during kilovoltage cone-beam CT (CBCT) imaging.

With the characterization of the dosimeter completed at diagnostic energies, it was suggested that the response of the FOC dosimeter also be investigated at megavoltage (MV) photon energies typically used in radiation therapy. Interest in small point dosimeters for use in radiation therapy has grown in recent years as small radiation treatment fields for IMRT and radiosurgery have become more popular. For instance, in stereotactic radiosurgery, treatment fields as small as 1-3 cm in diameter are often used to deliver large doses of radiation to treat intracranial tumors.⁷⁷ In order to accurately plan these treatments, it is essential to develop a treatment plan with knowledge of the associated percent depth dose (PDD) curves and two-dimensional dose distributions in a water phantom. This information is typically obtained by direct measurement using a dosimeter such as an ionization chamber. The current gold standard for dosimetry measurements in radiation therapy is the 0.6 cc farmer type ion chamber. Unfortunately, for small field radiotherapy dosimetry, the active element of this chamber is too large and would be subject to partial volume effects. To overcome this issue, several different types of dosimeters have been developed, including small volume ion chambers, metal-oxide-semiconductor field effect transistors (MOSFETs), diamond detectors, radiographic films, and thermoluminescent detectors (TLDs). However, these dosimeters are not without their own

drawbacks. Small volume ion chambers can suffer from leakage current that can make up a substantial fraction of the signal thus affecting the accuracy of dosimetry measurements.⁷⁸ MOSFET detectors show significant angular dependence⁷⁹ and poor reproducibility for low dose fractions.⁸⁰ Diamond detectors suffer from dose-rate dependence⁸¹ while TLD and radiographic film measurements both require post-irradiation reading which makes online dose assessment impossible. The FOC dosimeter overcomes several of these issues with one of the smallest sensitive elements of any dosimeter, the ability to display real-time dose information, and minimal angular dependence due to a cylindrically symmetric sensitive element. Additionally, FOC dosimeters do not require corrections for changes in temperature, pressure, or humidity.⁸² The usual conversion of absorbed dose from one medium to another can also be avoided because the plastic scintillator material used in FOC dosimeters is water-equivalent.⁸³

Previous authors have characterized different variations of FOC dosimeters for dosimetry measurements at MV energies with some success.⁸⁴⁻⁸⁸ Several authors have even gone as far as building 2-dimensional arrays of FOC dosimeters for use in IMRT quality assurance (QA).^{71, 89} The plastic scintillator based FOC dosimeters are ideal for this application as their water-equivalence allows them to be placed in close proximity to each other for high spatial resolution measurements with minimal fluence perturbation. To date, none of the prototypes discussed in the literature have reached widespread clinical use. Nonetheless, the field of FOC dosimetry continues to move forward and grow to meet the needs of MV dosimetry in radiotherapy. This work presents on the characterization of the FOC dosimetry system first described in Chapter 3 using an MV photon beam produced by a medical linear accelerator.

Methods and Materials

FOC Dosimetry System

The dosimetry system used for this work was, for the most part, the same as that presented in Chapter 3. Previously, the box housing the PMT array was lined with 1/16" lead shielding to limit the number of spurious pulses detected due to scattered x-rays reaching the PMTs and causing photocathode emissions. However, at therapeutic photon energies, this shielding was not sufficient. Instead of adding additional shielding for this application, a decision was made to simply move the box out of the treatment room and into the console area. This meant that the optical fibers connecting the scintillator of each dosimeter to its respective PMT needed to be lengthened. After a quick survey of the linac vault, it was found that each dosimeter would have to be 15 m long to reach from the treatment table to the console area. While increasing the length of the optical fiber will undoubtedly result in attenuation of the light signal, previous experience from diagnostic exposures has shown that the light signal was already several orders of magnitude greater than the background signal. Therefore, the added attenuation of the light signal from a longer optical fiber was not really a concern.

The new dosimeter was constructed using the same materials previously described in Chapter 3 except that instead of a 2 m long optical fiber, a 15 m long optical fiber was used. To allow subtraction of the stem effect commonly seen in FOC dosimeters, a reference fiber was also included in the FOC dosimeter assembly. It is important to note that the stem effect at MV energies is much larger than at kV energies. This is mainly due to the fact that at these energies, secondary electrons have enough energy to produce Cerenkov radiation in the silica optical fibers.⁹⁰ Cerenkov radiation is produced when charged particles, such as secondary electrons, cross a transparent medium at a speed greater than the speed of light in that material. This causes the electric dipoles of nearby molecules to oscillate and emit visible light. This light was named

Cerenkov radiation after Pavel Cerenkov, the Nobel Prize winning scientist who first characterized this phenomenon. As shown in Figure 4-1, the Cerenkov radiation in a silica optical fiber is emitted in a broad spectrum with a $1/\lambda^3$ dependence. From this figure, it can be seen that the Cerenkov light spectrum stretches from approximately 200 to 700 nm, overlapping the scintillators emission peak at 435 nm (not shown). To overcome this issue, the measured light output of the reference fiber is subtracted from the measured light output of the signal fiber, leaving only the component of light from the scintillator itself. This method of handling the stem effect is known as background subtraction and has previously been exploited with success.⁹¹

Dose Measurements

Characterization of the FOC dosimeter at MV photon energies was carried out using an Elekta Synergy linear accelerator (Elekta Oncology Systems, Crawley, UK). An accelerating potential of 6 MV was selected for all tests as it is one of the most popular energies used in radiation therapy. The linac was calibrated to deliver 1 cGy per monitor unit (MU) at the depth of maximum dose in water (1.5 cm for 6 MV) with a 100 cm source-to-axis distance (SAD) and a 10x10 cm field. For simplicity, all measurements were performed at an SAD of 100 cm, depth of 10 cm in a solid water phantom, and a 10x10 field unless otherwise noted.

All results reported in this study have been corrected for the stem effect with the use of a reference fiber. A calibration between the PMT used for the signal fiber and the PMT used for the reference fiber was also performed to eliminate the influence of sensitivity differences between the two PMTs.

Linearity

The linearity of the FOC dosimeter as a function of total dose was evaluated by increasing machine output from 10 to 500 MU in finite increments while holding the energy constant at 6 MV. The dose rate was also held constant at approximately 565 MU/min for this experiment. To

reduce statistical uncertainties and provide reproducibility metrics, measurements were repeated 3 times. The stability of the FOC dosimetry system was also investigated by repeating these measurements several days later and comparing the results. These data were then used to create a plot of MU versus net counts from the dosimeter. A linear fit was applied to the data and the correlation coefficient was used to quantify the linearity of the dosimeter.

Reproducibility

The reproducibility of the FOC dosimeter was evaluated using the data from the linearity experiment. Because each measurement was repeated three times, the data provided an adequate sample from which to take average values and standard deviation for different dose levels used in radiation therapy. The coefficient of variation (COV) at each dose level was calculated to quantify the dosimeter's reproducibility.

Dose Rate Dependence

The dose rate dependence of the FOC dosimeter was investigated by delivering 50 MU at several different dose rates. Clinically relevant dose rates of approximately 68, 137, 277, and 565 MU/min were investigated. Data was then normalized to the dose rate at 565 MU/min for ease in comparison. A plot of normalized dosimeter response versus dose rate was created to show the variation in response of the dosimeter to changing dose rate.

Field Size Dependence

The ability of the FOC dosimeter to accurately measure output factors for different field sizes was also investigated. A fixed output of 200 MU was selected and delivered at a dose rate of approximately 565 MU/min. Measurements were repeated for field sizes of 3x3, 5x5, 10x10, and 15x15 cm. These data were then normalized to the reading at a 10x10 cm field size to represent the output factor for several common field sizes used in radiation therapy.

Results

Linearity

Figure 4-2 plots the response of the FOC dosimeter, in counts, versus the machine output in MU. Error bars are not shown because they are too small to be displayed. A linear trend line was fitted to the data and the correlation coefficient was found to be 1.000. This result demonstrated that the FOC dosimeter has a very linear response over the dose range of interest in radiation therapy.

Reproducibility

Table 4-1 summarizes the average readings and standard deviation, in counts, from the linearity experiment. The coefficient of variation was less than 3% for all measurements, with many readings showing a variation of less than 1%. As expected, the variation was slightly higher at low doses due to less total counts and more fluctuations between readings.

Dose Rate Dependence

Figure 4-3 plots the normalized response of the FOC dosimeter versus the dose rate in MU/min. The response was normalized to a dose rate of 565 MU/min for ease in comparison. The response of the dosimeter remained relatively constant with only a 4% variation across the clinical range of dose rates investigated. This result shows that the response of the dosimeter is fairly independent of dose rate and that dose rate specific calibration factors may be required for only the most demanding dosimetry measurements.

Field Size Dependence

Table 4-2 summarizes the output factors and net counts measured using the FOC dosimeter for field sizes of 3x3, 5x5, 10x10, and 15x15 cm. As can be seen, the net counts decreased with field size. This led to the output factor also decreasing with field size when normalized to a standard 10x10 field. This is opposite of the expected results, which is an increase in net counts

for larger field sizes due to the additional scatter along the central beam axis. Potential reasons for this discrepancy and methods to overcome this issue are discussed in the next section.

Discussion

The FOC dosimeter exhibited excellent dose linearity and reproducibility when exposed to 6 MV photons from a medical linear accelerator. Additionally, the response of the dosimeter was fairly independent of dose rate and varied by approximately only 4% over the range of dose rates investigated in this study. The angular dependence was not investigated as it was previously shown in Chapter 3 that there is very little variation during an axial irradiation due to the cylindrical geometry of the sensitive element. Lastly, the ability of the FOC dosimeter to measure output factors for different field sizes was investigated and very unusual results were observed. As the field size was increased, the net counts were observed to decrease as shown in Table 4-2. This result is the opposite of the expected response which is an increase in net counts due the additional scatter associated with a larger field size. Dose measurements performed with a calibrated ion chamber confirmed that the measured dose did indeed increase with increasing field size.

In an attempt to overcome this issue, several possible sources of error were investigated. At first, it was thought that the PMT used to measure the light output from the signal fiber and the PMT used to measure the light output from the reference fiber could possibly exhibit different spectral responses. To test this idea, the field size dependence experiment was repeated and the light output from both signal and reference fibers were measured individually using the same PMT. The results of this experiment indicated that the net counts still decreased with increasing field size, ruling out possible response differences between the PMTs.

Next, it was suspected that differences in radiation induced light output between the two optical fibers (signal and reference fibers) may be the cause for the observed discrepancy. To test

this idea, the scintillator was removed from the signal fiber and the field size dependence experiment was repeated. Again, all measurements were taken on the same PMT to rule out any response differences between the PMTs. A 50 MU exposure was delivered and the measurements were repeated 3 times to reduce statistical uncertainties. This experiment revealed that the radiation induced light output between the two optical fibers was nearly identical, as shown in Table 4-3. This result ruled out differences in radiation induced light between the two optical fibers as a potential source of error.

With the most obvious solutions ruled out, we began to consider other potential sources of error. Further examination of the data in Table 4-2 revealed that the counts from the reference fiber increased more quickly with field size than the counts from the signal fiber. After some thought, a potential cause for this phenomenon was discovered. Cerenkov light produced in the reference fiber that travels down the fiber in the opposite direction of the PMT would be efficiently reflected at the glass/air interface (index of refraction for glass ≈ 1.5) present at the end of the optical fiber and ultimately reach the PMT. However, light produced in the signal fiber that traveled down the fiber in the opposite direction of the PMT would not be as efficiently reflected at the glass/scintillator interface because the plastic scintillator ($n \approx 1.5$) has a similar index of refraction as the glass. Ultimately, this would account for more Cerenkov light reaching the PMT from the reference fiber than from the signal fiber as field size was increased and more Cerenkov light was produced. To test this idea, the signal and reference fibers were modified such that the interfaces at the end of the fibers were the same. This was done by attaching a scintillator to the end of both fibers. The scintillator attached to the signal fiber was made slightly longer than the reference fiber (5 mm compared 2.5 mm) so that the difference in signal between the two could be differentiated. To test this prototype, the field size dependence

experiment was repeated once again. Unfortunately, the difference in signal between the two fibers was very small. However, by repeating the measurements several times, we were able to determine a general trend and it was apparent that the net counts did indeed still decrease with increasing field size.

Finally, after ruling out all other possible causes for the observed discrepancy, it was assumed that the incident spectrum of light from the optical fiber was causing an unusual response from the PMT itself. Data from the manufacturer was obtained and it was found that the PMT was sensitive to light in the 300-600 nm range. From Figure 4-1, it can be seen that Cerenkov radiation is emitted throughout this range, but has the highest intensity at wavelengths shorter than 400 nm. Therefore, an optical filter was chosen to filter out these shorter wavelengths while still allowing the scintillation light (peak at 435 nm) to pass. It was hoped that by filtering out this unwanted light, the PMT would respond in a more predictable fashion. Therefore, a 400 nm high pass filter was chosen and installed at the PMT/optical fiber interface. Also, the scintillation element from the last experiment was removed from the reference fiber and the FOC dosimeter was returned to its original configuration. The field size experiment was repeated once again and data revealed that the net counts still decreased with increasing field size, as shown in Table 4-4. However, the filter did decrease the total counts registered by the PMT, indicating that the filter was indeed removing light from the spectrum.

As a last resort, the energy dependence of the scintillator was considered. As the field size is increased, the photon spectrum incident on the dosimeter placed in a phantom changes due to increased scatter. If the scintillator exhibits strong energy dependence, this small change in the energy spectrum with field size could lead to the observed discrepancy. In order to test this idea, the dosimeter was placed free in air where scatter would be negligible and the field size

dependence experiment was repeated. Even in the absence of scatter, the net counts still decreased with increasing field size, as shown in Table 4-5. This finding ruled out energy dependence as a cause for the observed discrepancy.

After all of these experiments, it can be concluded that the observed discrepancy during the field size dependence experiment was not a result of spectral response variations between different PMTs, differences in radiation induced light in the optical fibers, interface reflection differences, or energy dependence of the scintillator. While these causes have been ruled out, it is still unclear as to why the net counts decrease with increasing field size. Theoretically, the spectrum of light from both the reference and the signal fibers should be the same with exception of a photopeak in the signal fiber spectrum from the scintillator. A simple subtraction of the reference fiber from the signal fiber should then yield the counts only from the scintillator. One possible cause for the observed discrepancy is related to transient darkening of the optical fibers. In this case, the fiber's ability to transmit light is reduced when irradiated and the optical fiber effectively "darkens," ultimately reducing the number of scintillation photons reaching the PMT. Darkening of the optical fiber when irradiated would explain why the observed counts from the signal fiber do not increase as fast as the observed counts from the reference fiber when field size is increased. However, most authors have not observed this effect at doses and dose rates produced by medical linear accelerators. Another possible cause is related to the PMT not responding in the same fashion to the two different spectrums of light from the signal and reference fibers. Most authors overcome the latter issue by using a CCD camera to readout the FOC dosimeters. A CCD camera is ideal for this application as the different color channels of the camera can be used to characterize the spectrum of light and find the contribution from only the scintillator. This technique is known as chromatic filtering and has been used with success by

several authors.^{88, 91, 92} The CCD camera also offers a more cost effective solution for reading multiple dosimeters out simultaneously.

Conclusion

While the FOC dosimeter shows promise at MV energies, there are still some problems to be resolved. The dose linearity, reproducibility, and dose rate dependence of the FOC dosimeter at MV energies was investigated in this study and yielded very good results. The response of the dosimeter as field size was varied was also investigated and yielded peculiar results; specifically, the net counts of the dosimeter were seen to decrease with increasing field size, the exact opposite of the expected result. Several possibilities for this discrepancy were investigated to no avail. Further investigation is needed but may not be warranted as the next generation of the FOC dosimetry system is currently under development and includes a CCD camera rather than PMTs. This will allow techniques such as chromatic filtering to be used instead of just simple background subtraction to handle the Cerenkov radiation produced at MV energies. Therefore, further investigation into the characterization of the FOC dosimeter at MV energies is postponed until the CCD camera system is completed.

Table 4-1. Reproducibility of measurements with FOC dosimeter at MV energies

MU	Mean counts (net)	Standard deviation	COV (%)
10	12252	246	2.01%
20	21155	318	1.50%
30	30804	63	0.20%
40	39753	539	1.36%
50	48409	1425	2.94%
75	70766	1434	2.03%
100	93681	1802	1.92%
125	116243	1377	1.18%
150	140250	224	0.16%
175	161460	745	0.46%
200	186220	1706	0.92%
250	232168	1996	0.86%
300	276497	1390	0.50%
400	372379	1309	0.35%
500	465076	3437	0.74%

Table 4-2. Counts from signal and reference fibers as well as output factors normalized to a 10x10 cm field size from a 200 MU irradiation.

Field size (cm)	Signal fiber	Reference fiber	Net counts	Output factor
3x3	772623	428228	297132	1.223
5x5	788404	484552	261114	1.075
10x10	829559	545759	242975	1.000
15x15	854715	586919	228573	0.941

Table 4-3. Counts from each optical fiber with no scintillator during a 50 MU irradiation

Field size (cm)	Fiber 1		Fiber 2	
	Average	1 σ	Average	1 σ
3x3	99792	825	99390	61
5x5	106887	398	107048	244
10x10	119064	1278	120286	400
15x15	129393	3060	129836	855

Table 4-4. Counts from signal and reference fibers from a 50 MU irradiation after passing through a 400 nm high pass filter. Output factors normalized to a 10x10 cm field size.

Field size (cm)	Signal fiber	Reference fiber	Net counts	Output factor
3x3	136920	63680	73240	1.374
5x5	141923	77682	64241	1.205
10x10	152258	98955	53303	1.000
15x15	157796	111585	46211	0.867

Table 4-5. Counts from signal and reference fibers from a 50 MU irradiation free in air. Output factors normalized to a 10x10 cm field size.

Field size (cm)	Signal fiber	Reference fiber	Net counts	Output factor
3x3	135754	11426	46684	1.578
5x5	138586	18348	43642	1.286
10x10	149729	38170	34191	1.000
15x15	154300	53823	27343	0.873

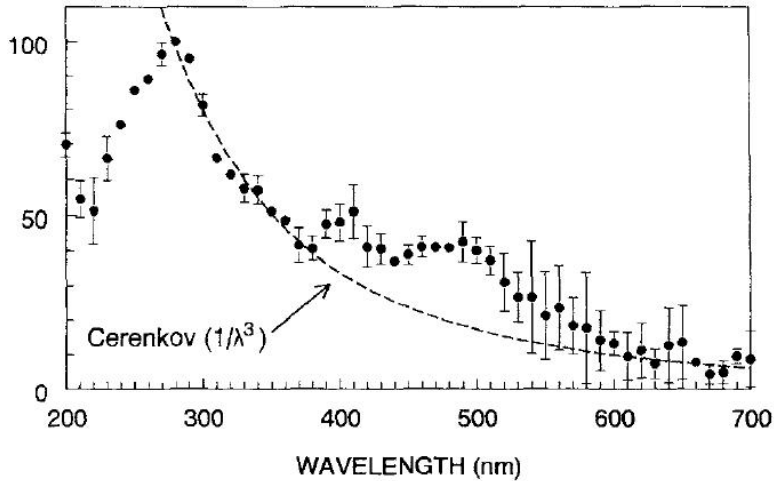


Figure 4-1. Radiation induced light in a silica optical fiber. The dashed line represents the theoretical Cerenkov spectrum. A weak luminescence signal due to impurities in the silica fiber begins at 380 nm and is superimposed on the Cerenkov light spectrum. (Used with permission from: M. R. Arnfield, "Radiation-induced light in optical fibers and plastic scintillators: Application to brachytherapy dosimetry," IEEE Trans Nucl Sci **43**, 2077-2084 (1996), Figure 1, p. 2078).

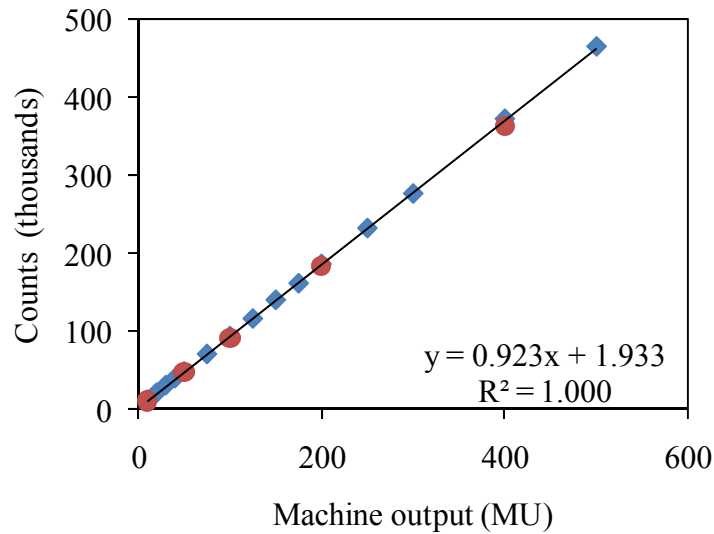


Figure 4-2. Dose linearity of FOC dosimeter. Blue squares represent data taken on day 1 and red circles represent data taken on day 2.

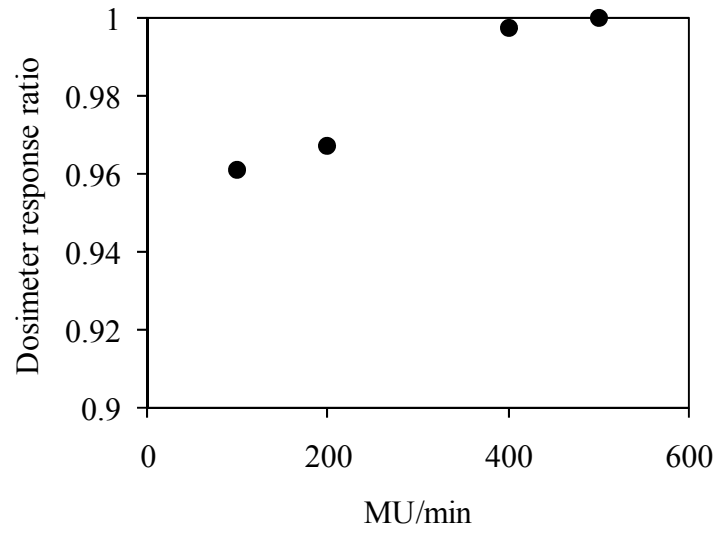


Figure 4-3. Response of FOC dosimeter versus dose rate in MU/min. Data has been normalized to a dose rate of 565 MU/min to aide in comparison.

CHAPTER 5 AN ORGAN AND EFFECTIVE DOSE STUDY OF XVI[®] AND OBI[®] CONE-BEAM CT SYSTEMS

Introduction

Advances in radiation treatment delivery, such as intensity-modulated radiation therapy (IMRT), have made it possible to deliver large doses of radiation to a treatment volume with a high degree of conformity. While a highly conformal treatment offers the advantage of sparing surrounding normal tissue, this benefit can only be realized if the patient is accurately positioned during each treatment session. The need to accurately position the patient has led to the development and use of gantry mounted kilovoltage cone-beam computed tomography (CBCT) systems.^{23, 93} These systems are used to acquire high resolution volumetric images at the time of treatment, which can then be digitally registered with the planning CT in order to determine the appropriate shifts of the treatment table required to accurately align the patient. To date, two such systems are commercially available, the X-ray Volumetric Imager (XVI[®], Elekta Oncology Systems, Crawley, UK) and the On-Board Imager (OBI[®], Varian Medical Systems, Palo Alto, CA).

While CBCT is a very useful tool for ensuring that a patient is properly aligned prior to treatment, daily use in a high fraction therapy regimen will result in an associated imaging radiation dose. In an effort to quantify the dose from CBCT, several authors have performed dose measurements in cylindrical acrylic phantoms, reporting measured doses as high as 10 cGy from a single scan.^{34, 45, 46, 94, 95} While these studies provide useful dose metrics for which to compare different imaging protocols and equipment, the reported doses should be taken with great caution as humans are substantially different in size, shape, and attenuation from the acrylic phantoms used in these studies.⁴¹ To more accurately quantify patient dose, several other authors have performed dose measurements within commercially available anthropomorphic

phantoms.^{32, 39, 96-98} The present study aims to build on these previous studies by performing a comprehensive set of organ dose measurements in an adult male anthropomorphic phantom for both the XVI and OBI CBCT systems using currently available manufacturer-installed protocols and software (Version 4.0 for the XVI and Version 1.4.13.0 for the OBI). Previous studies with the XVI did not include the use of a bow-tie filter (and associated protocols to account for the filter) and a recent software upgrade to the OBI has reduced the total tube-current time product used and now offers a half rotation scan for head protocols. These technical changes to imaging parameters are intended to reduce the patient dose from cone beam imaging, which is of increasing clinical significance with daily image acquisitions.

Organ doses were quantified for 26 organs using an anthropomorphic phantom. Most of the 26 organs were chosen based on recommendations by the International Commission on Radiological Protection (ICRP) Publication 103 for the evaluation of effective dose.⁴⁸ As is common in medical physics, the effective dose was adopted as a way to assess whole body dose for a specific patient and to compare different imaging protocols and equipment.⁹⁹ It is important to stress that because only a male phantom was used to derive the effective dose, and the weighting factors defined by the ICRP are sex averaged, the reader should be cautious if using this value in risk estimation models. In addition to the dosimetry measurements, a comparison of image quality for each of the factory-installed protocols was performed using a Catphan® 440 image quality phantom.

Methods and Materials

CBCT Systems Evaluated

This study evaluated dose delivered from both the Elekta XVI and Varian OBI CBCT systems. The two systems are similar in design with a kV x-ray source and flat-panel detector mounted to the gantry and sharing a common axis of rotation with the MV treatment beam. A

brief description of each system is presented in the following text; however, readers looking for a more complete description are referred to Song *et al.*⁴⁶

The XVI system utilizes an amorphous silicon/cesium iodide (aSi/CsI) flat-panel detector with a 1024x1024 array of 0.4 mm elements. The x-ray source is mounted to a retractable arm with a fixed source to isocenter distance of 100 cm and offers several different collimators and kV filter combinations which are interchangeable based on the desired volume to be scanned. For the head scan, a “head and neck” protocol was selected along with an S20 collimator, which yielded an axial field-of-view (FOV) of 27 cm, as shown in Figure 5-1(a), with a length of 26 cm along the longitudinal axis. Chest scans were performed with a “chest” protocol and an M20 collimator which yielded an axial FOV of 41 cm with a length of 26 cm. Pelvis scans were performed with a “prostate” protocol and an M10 collimator, which yielded an axial FOV of 41 cm with a length of 12.5 cm. In addition to changing the collimators for each protocol, the chest and pelvis scans also required that the detector panel be shifted orthogonal to the kV beam axis to achieve the increased FOV,¹⁰⁰ as shown in Figure 5-1(b). Additionally, a bow-tie filter (designation F1) was utilized for both the chest and pelvis scans.

The OBI system utilizes an amorphous silicon (aSi) flat-panel detector with a 2048x1536 array of 0.194 mm elements. The x-ray source for the OBI is mounted to a retractable arm with a variable source to isocenter distance of 80 to 100 cm. However, during this study, all measurements were performed with a fixed source to isocenter distance of 100 cm. The operation of the OBI unit is similar to the XVI unit, but offers only two different scan modes: full and half-fan. In the full-fan mode, a full bow-tie filter is used and the collimation is automatically adjusted by a set of dynamic jaws mounted to the x-ray source. The resulting FOV is 25 cm with a length of 18 cm, as shown in Figure 5-1(c). In the half-fan mode, the detector

panel is shifted orthogonal to the kV beam axis and a half bow-tie filter is used; resulting in a FOV of 45 cm with a length of 16 cm, as shown in Figure 5-1(d). The full-fan scan was used for head imaging due to its smaller FOV while the half-fan scan was reserved for chest and pelvis imaging.

For each machine, three clinically relevant scan sites were investigated: head, chest, and pelvis. Technical settings for each scan remained unchanged from the manufacturer-installed protocols currently used at our institutions. Table 5-1 summarizes the measured half-value layers (HVLs) in aluminum, as well as the relevant scan parameters used for each protocol. From this data, it can be seen that the manufacturers have selected widely varying technical settings, even for the same anatomical sites.

Anthropomorphic Phantom

The anthropomorphic phantom used in this study was based on a hybrid computational model representing a 50th percentile adult male. In this context, hybrid refers to a cross between stylized and tomographic phantoms, exploiting the advantages of each. A hybrid phantom offers the scalability of a stylized phantom while maintaining the anthropomorphic characteristics of a tomographic phantom. The hybrid model originated from a tomographic dataset of a 36-year-old Korean male (176 cm height, 73 kg weight). Using methods previously described by Lee *et al.*⁵⁷,⁵⁸, the tomographic dataset was imported into Rhinoceros computer software (McNeel North America, Seattle, WA) and transformed into non-uniform rational B-spline (NURBS) surfaces that could easily be manipulated. Modifications to the original dataset were done to match the anthropometric dimensions and organ masses of a 50th percentile adult male as defined by the International Commission on Radiological Protection (ICRP) Report 89 reference data.⁴⁷

Techniques previously described in Chapter 2 were used to construct the physical phantom from this hybrid dataset in 5 mm thick slices using three tissue-equivalent materials that mimic

the dosimetric characteristics of a real human body. These materials include soft tissue-equivalent substitute (STES), lung tissue-equivalent substitute (LTES), and bone tissue-equivalent substitute (BTES). While the hybrid dataset included over three-hundred 5 mm thick axial slices, the lack of radiosensitive organs in the legs justified their exclusion from fabrication. For this reason, the completed phantom includes approximately 200 slices, ranging from the crown of the head to mid-thigh. The torso of the completed phantom was previously shown in Figure 2-6. It should be noted that while the phantom is pictured with arms attached, the arms were not used during data acquisition as patients are typically positioned such that their arms are not in the radiation field during treatment. To hold the phantom together during imaging, a patient immobilization vacuum bag was utilized.

Dosimetry System

A fiber optic coupled (FOC) dosimetry system was used for all organ dose measurements in this study. Previously described in Chapter 3, the dosimeter consists of a water-equivalent plastic scintillator (BCF-12, Saint-Gobain Crystals, Nemours, France), 500 μm in diameter and 2 mm in length, coupled to a 400 μm diameter optical fiber that is 2 m in length (400-UV, Ocean Optics Inc., Dunedin, FL). The optical fiber acts as a light guide to transmit scintillation photons to a photomultiplier tube (PMT) (H7467, Hamamatsu Corporation, Bridgewater, NJ). A second optical fiber with no scintillator, referred to as the reference fiber, was also used to account for the stem effect commonly seen in FOC dosimeters as a result of the native fluorescence of the optical fiber itself.^{70, 72, 75} This reference fiber was integrated into the FOC dosimeter assembly using a single piece of heat shrink tubing which was bifurcated at its end to allow each fiber to be connected with its respective PMT. By using a reference fiber, the fluorescence of the optical fiber itself can be quantified and subtracted from the FOC dosimeter signal (which includes components from both the plastic scintillator and optical fiber fluorescence), thus leaving only

the signal from the scintillator. Coupling the optical fibers to the readout PMTs was achieved by installing a female SMA (SubMiniature version A) connector to each fiber and a male SMA connector on the face of each PMT. For clarification, a schematic detailing the components of the dosimetry system is shown in Figure 5-2. To increase the speed of data collection, a total of two FOC dosimeters were used in this study, requiring the use of four identical PMTs. To interface with this PMT array, a custom MATLAB (MathWorks Inc., Natick, MA) computer program was also developed.

Calibration of the FOC dosimeters, in net counts per unit air kerma, was performed at different depths in water using a calibrated (traceable to an accredited dosimetry laboratory) 15 cm³ pancake ion chamber and associated electrometer (chamber model 96035B, electrometer model 35050A, Keithley Instruments Inc., Cleveland, OH). The calibration was performed at several depths in order to account for the energy dependence of the dosimeter as the beam quality changes with depth due to beam hardening and the addition of a scatter component. Results indicated that the sensitivity of the dosimeter varied by approximately 5% across the depth range investigated (surface to 16 cm). Therefore, the calibration factor measured at a depth of 8 cm was chosen for all in-phantom dose measurements as it offered a compromise between the surface and deepest calibration factors relevant to the dimensions of the phantom and also minimized the uncertainty of the dose measurements due to the energy dependence of the dosimeter (i.e. ±2.5%). Using this calibration factor, the absorbed dose to soft tissue, D_{abs} , was calculated using Equation 5-1.

$$D_{\text{abs}} = \frac{C_{\text{net}}}{CF} \left[\left(\frac{\bar{\mu}_{\text{en}}}{\rho} \right)_{\text{air}}^{\text{soft tissue}} \right] \quad (5-1)$$

In the above equation, C_{net} is the net counts from the dosimeter, CF is the calibration factor measured at a depth of 8 cm in net counts per unit air kerma, and $\left(\frac{\bar{\mu}_{\text{en}}}{\rho}\right)_{\text{air}}^{\text{soft tissue}}$ is the ratio of average mass energy absorption coefficients of soft tissue to air at the measured HVL.¹⁰¹

The maximum uncertainty for in-phantom FOC dosimeter measurements was estimated to be approximately 4%. Contributing factors included: (1) energy dependence of ~2.5% as the beam quality varies within the phantom due to hardening and scatter; (2) angular dependence of ~2.5% averaged over an entire revolution from a normal-to-axial irradiation in a scatter medium; (3) reproducibility variation of ~1% for diagnostic level exposures; and (4) variation of ~1.5% in the dosimeters response depending on the bend radius of the optical fiber. The full characterization of the FOC dosimeter can be found in Chapter 3.

Calculation of Organ Doses

To achieve clinically relevant dose values, the anthropomorphic phantom was set up and imaged in a close approximation to a real patient for the particular anatomical region being treated. For head scans, the phantom was aligned with the center of the brain at isocenter of the treatment beam. For chest scans, the isocenter was placed in the center of the body at an axial plane near the center of the lungs. For pelvis scans, the center of the prostate was placed at isocenter. To ensure reproducible results, care was always taken to accurately position the phantom on each machine before beginning data acquisition.

To aid in the positioning of dosimeters, organ locations were transferred onto the phantom using a permanent marker from full-scale printouts of the hybrid dataset. Thin slits were cut into the axial slices of the phantom to allow placement of both the FOC dosimeters and passage of the optical fiber that connects the scintillator to the readout PMT (see Figure 5-3). For small organs, absorbed dose values obtained near the centroid of the organ were adopted as the organ

dose. For larger organs where dose gradients are a concern, the organ was equally subdivided and dosimeters were placed near the centroid of each of these subdivisions. The average reading from all dosimeters placed in the organ was then adopted as the average organ dose. Table 5-2 lists all of the organs investigated as well as the number of measurement locations used to evaluate the dose to each organ.

In order to calculate the average dose to the red bone marrow, weighting factors were applied to individual red bone marrow sites (a total of 19 points in 12 sites) based on their percent weight contribution to the total red bone marrow, as shown in Equation 5-2.

$$D_{\text{RBM}} = \sum_i D_{\text{abs},i} * A_i \quad (5-2)$$

In the above equation, $D_{\text{abs},i}$ is the absorbed dose to soft tissue at location i and A_i is the weight fraction of red bone marrow located at location i . The absorbed dose to soft tissue was used to approximate the dose to the red bone marrow because the mass energy-absorption coefficient for red bone marrow is within 5% of the mass energy-absorption coefficient for soft tissue at x-rays energies greater than 30 keV.¹⁰² Dose to the bone surface was calculated in a similar fashion using Equation 5-2, except A_i was replaced with E_i , the weight fraction of endosteum at location i . Table 5-3 shows weight fractions of red bone marrow and endosteum used for the bone sites investigated in this study, taken from the development of the hybrid computational phantom series.¹⁰³

The absorbed dose to lung tissue was calculated using Equation 5-3, where $\left(\frac{\bar{\mu}_{\text{en}}}{\rho}\right)_{\text{soft tissue}}^{\text{lung}}$ is the ratio of average mass energy absorption coefficients of lung tissue to soft tissue at the measured HVL.¹⁰¹

$$D_{\text{lung}} = D_{\text{abs}} \left[\left(\frac{\bar{\mu}_{\text{en}}}{\rho} \right)_{\text{soft tissue}}^{\text{lung}} \right] \quad (5-3)$$

The absorbed dose to skin (for the whole body) was calculated similarly using Equation 5-4, where $\left(\frac{\bar{\mu}_{\text{en}}}{\rho} \right)_{\text{soft tissue}}^{\text{skin}}$ is the ratio of average mass energy absorption coefficients of skin to soft tissue at the measured HVL¹⁰¹ and $\frac{A_{\text{irradiated}}}{A_{\text{total}}}$ is the ratio of irradiated skin area to the gross surface area of the entire phantom.

$$D_{\text{skin}} = D_{\text{abs}} * \frac{A_{\text{irradiated}}}{A_{\text{total}}} * \left[\left(\frac{\bar{\mu}_{\text{en}}}{\rho} \right)_{\text{soft tissue}}^{\text{skin}} \right] \quad (5-4)$$

The gross surface area of the phantom used in this study was estimated to be 1.83 m² using the computational model as a reference. The irradiated area was also estimated using the computational model as a reference and values of 0.12 m², 0.32 m², and 0.20 m² were used for the head, chest, and pelvis scans, respectively. The absorbed dose at the surface of the phantom was evaluated by placing two dosimeters in the primary field at the anterior and left lateral sides of the phantom and averaging the readings from these two dosimeters.

Calculation of Effective Dose

The measured organ doses along with weighting factors from the ICRP Publication 103 were used to calculate a reference male effective dose for each protocol. Equation 5-5 shows the formula recommended for evaluating the effective dose, where w_T is the tissue weighting factor and H_T is the equivalent dose for each organ. In this case, the equivalent dose is simply the organ dose multiplied by a radiation weighting factor of unity for x-rays.

$$E = \sum_T w_T H_T \quad (5-5)$$

As previously mentioned, only a male phantom was used to derive the effective dose and the weighting factors defined by the ICRP are sex averaged. Therefore, this value is not intended for use in risk estimation models based on effective dose but rather for comparing different imaging protocols and equipment presented in this study.

Similar to other authors conducting effective dose calculations from organ dose measurements within anthropomorphic phantoms, the doses to two remainder organs were not measured: lymphatic nodes and muscle.^{102, 104} This was due to the fact that these organs are distributed throughout the body making it technically difficult to obtain an average organ dose measurement. Additionally, both of these organs are included in the category of “remainder organs,” along with 11 other organs. As a result, the dose to these two organs does not contribute greatly to the overall effective dose. Therefore, the weighting factor for remainder organs was simply applied to the average dose to the other 11 remainder organs.

Image Quality

It should be emphasized that the doses reported in this study result from using technical imaging settings provided by the manufacturer as their installed default protocols. No attempt was made to compare doses at the same image quality, but rather at clinically relevant scan settings. Consequently, there may be differences between the image quality achieved by the different systems, which was also evaluated. A Catphan[®] 440 (The Phantom Laboratory, Salem, NY) image quality phantom was used to assess the image quality of each CBCT system as it is used clinically. Image quality was assessed using the following Catphan modules: CTP401 slice geometry and sensitometry module and CTP592 low and high contrast resolution module. The CTP592 module has a series of high resolution test patterns ranging from 5 through 15 lp/cm which were used for visual evaluation of spatial resolution. This module also includes a series of 0.5% low contrast targets for evaluating low-contrast detectability. Unfortunately, the 0.5% low

contrast targets were designed to evaluate fan-beam CT systems and are too demanding for CBCT image quality tests. As a result, they cannot be seen in the reconstructed CBCT images. For this reason, the CTP401 module was used as a substitute to compare the low contrast detectability of each CBCT system. This module includes five acrylic spheres of varying diameters (2, 4, 6, 8, and 10 mm diameter) that have approximately 3% contrast¹⁰⁵ and can be seen in the reconstructed images. By visually evaluating the smallest sphere that could be seen in the reconstructed images, the CTP401 module was effectively used to illustrate the differences in low contrast detectability between the two systems. The Catphan phantom was scanned using the same clinical protocols used during organ dose measurements. All images were reconstructed at a 5 mm slice width with a matrix size of 512x512 pixels.

Results

The measured organ and effective doses from the XVI and OBI are shown in Tables 5-4 and 5-5, respectively. The “whole body” bone marrow and bone surface doses were calculated as previously discussed while the “irradiated site” bone marrow and bone surface doses are an average of only the bone sites in the primary field. For head scans, this includes the cranium and cervical vertebrae; for chest scans, the proximal humerus, clavicles, scapula, ribs, sternum, and thoracic vertebrae; and for pelvis scans, the os coxae, sacrum, and proximal femur. The “irradiated site” skin dose is an average of the dose measured from the two dosimeters placed in the primary field on the anterior and left lateral surfaces of the phantom.

The results of the image quality tests are shown in Table 5-6. Resolution was evaluated by the smallest resolution test pattern that could be visualized and low contrast detectability was evaluated by the smallest acrylic sphere that could be visualized in the image quality phantom.

Head

The head scan covered the brain, salivary glands, extrathoracic region, oral mucosa, and parts of the esophagus. Of all the organs, the lens of the eye received the maximum dose of 1.07 mGy for the XVI, while the brain received the maximum dose of 3.01 mGy for the OBI. Image quality was assessed through visual evaluation of the reconstructed images of the Catphan phantom. The CTP592 resolution module was used to evaluate the spatial resolution. The 8 lp/cm pattern could be visually resolved in the OBI images while none of the test patterns could be resolved in the XVI images, the largest of which was 5 lp/cm. The CTP401 module was used to evaluate low contrast detectability, with only the largest of the acrylic spheres (10 mm diameter) being visible on the OBI images; none of the spheres were visible on the XVI images. The images from the OBI were also noticeably sharper than those from the XVI. This can be seen in Figures 5-4 and 5-5 which show an example of the reconstructed images of the CTP592 and CTP401 modules, respectively.

Chest

The chest scan covered the lungs, breast, heart, thymus, thyroid, and parts of the esophagus, liver, stomach and spleen. The thyroid received the maximum dose of 19.24 mGy for the XVI, while the breast received the maximum dose of 5.34 mGy for the OBI. Again, the OBI showed superior spatial resolution, with the 5 lp/cm pattern visible in the reconstructed images, while none of the resolution test patterns were visible on the XVI images. The OBI also showed better low contrast detectability with the 4 mm diameter acrylic sphere being visible on the OBI images; the 6 mm diameter acrylic sphere was the smallest that could be seen on the XVI images. The reconstructed OBI images again appeared sharper overall than the XVI images.

Pelvis

The pelvis scan covered the prostate, bladder, testes, and parts of the small intestine and colon. The testes received the maximum dose for both systems at 29 and 34.61 mGy for the XVI and OBI, respectively. The images for the pelvis protocol appeared very similar to those seen for the chest protocol, yielding similar results for resolution and low contrast detectability. The 5 lp/cm pattern could be resolved on the OBI images while none of the test patterns could be resolved on the XVI images. For low contrast detectability, the 4 mm diameter acrylic sphere was visible on the OBI images while the 6 mm diameter acrylic sphere was the smallest that could be seen on the XVI images. The reconstructed OBI images again appeared sharper overall than the XVI images.

Discussion

It is important to differentiate the data presented in the current study with that which can be found in current literature. Kan *et al.*³⁹ published an organ and effective dose study performed on the OBI using a female anthropomorphic phantom and TLDs. While the study provides useful dose information for the OBI, the recent release of OBI software version 1.14.13.0 includes new protocols which have not yet been investigated in the literature. Previous protocols for the OBI were all at a fixed tube voltage (125 kVp) and consisted of full rotation scans. The updated OBI protocols utilize body region specific tube voltages, with lower energies for less attenuating body regions. Tube voltages include 100 kV, 110 kV, and 125 kV for the head, chest, and pelvis, respectively. Additionally, the new head protocol for the OBI utilizes only a partial rotation rather than a full rotation for image acquisition. Lastly, the tube-current time product for all OBI protocols has been reduced substantially. All of these changes result in lower patient doses, with the dose to many organs being reduced by 50% or more from previously published works utilizing earlier versions of the manufacturer installed protocols.³⁹ For the XVI system, there

have been very few organ dose studies published in the literature.^{45, 98} Additionally, these studies report the dose to only a limited number of organs and they were performed before the release of software version 4.0, which included the introduction of new protocols and the use of bow-tie filters. While the tube-current time product has been increased with the use of the new protocols to account for the added filtration, results indicate that individual organ doses for the XVI have remained comparable to the limited studies in the literature.

An interesting similarity between the XVI and OBI is the fact that they both use partial rotation scans for their head protocols (200° and 204°, respectively). On the XVI, image acquisition begins at the anterior surface of the patient and rotates around the left lateral side of the head, finishing posteriorly (when the patient is placed in a supine position). On the OBI, image acquisition moves from left to right lateral (or vice-versa) while rotating around the posterior surface of the patient. Due to the choice of acquisition angles, superficial organs located on the anterior surface of the head are directly irradiated during image acquisition with the XVI but not with the OBI, resulting in comparatively higher doses to some organs for the XVI. For example, the dose to the lens of the eye on the XVI system was 52% higher than the dose to a centrally located organ such as the brain while on the OBI system the dose to the lens of the eye was approximately a factor of 5 less than the dose to the brain. This result suggests modifying the manufacturer installed head protocol on the XVI such that the x-ray tube rotates around the posterior side of the head where there are no critical organs rather than the anterior side of the head which has several superficial organs of interest.

The chest protocol for each system utilized a full rotation scan. However, the beam width for the XVI was larger than the OBI, 26 cm compared to 16 cm, resulting in higher doses to organs outside of the treatment volume. The thyroid was one such organ, which is included in the

larger field of view and subsequently received the highest dose of any organ during a chest scan from the XVI but was outside of the primary field on the OBI. Contributing to the thyroid dose on the XVI was also the fact that the outer body contour was smaller in this region, resulting in less attenuation of the primary beam as the tube rotated around the body. This finding suggests reducing the beam width of the XVI in future versions if the necessary information can be gained from a narrower beam width such as what is used on the OBI to avoid unnecessarily irradiating organs outside of the treatment volume. As expected, the breast received the highest dose on the OBI due to its anatomical location at the periphery of the body.

The pelvis scans for each system also utilized a full rotation. Interestingly, the OBI had organ doses similar to those measured using the XVI, even though the tube-current time product was approximately a factor of 2.4 smaller. This can be attributed to the fact that the OBI has a larger beam width (16 cm compared to 12.5), resulting in additional scattered radiation, as well as a lower HVL (see HVLs in Table 5-1). As reported by Song *et al.*,⁴⁶ the lower HVL of the OBI results in more dose being deposited per unit mAs than the XVI. Additionally, the testes were completely in the primary beam of the OBI but were only partially covered by the XVI beam because of its smaller beam width, resulting in a higher gonad dose for the OBI when compared to the XVI. Similar to the case with the chest scan, the larger beam width resulted in more organs outside of the treatment volume being irradiated and an increased scatter dose inside of the scan volume.

The effective dose for each scan is also shown at the bottom of Tables 5-4 and 5-5. The head scans for both the XVI and OBI had very low effective doses (0.04 and 0.12 mSv, respectively) due to the fact that the most of the organs in the primary field for a head scan have low weighting factors. The chest scan yielded effective doses of 7.15 and 1.82 mSv for the XVI

and OBI respectively. The higher effective dose for the XVI chest scan was due to its larger beam width, which covered more organs, and higher tube-current time product, which resulted in higher overall organ doses. The pelvis scan for each system had similar effective doses at 3.73 and 4.34 mSv for the XVI and OBI, respectively. As is evident from the data presented in this study, the effective dose for each protocol was small due to the limited number of organs involved in each scan. This is especially true for the pelvis scans, where both the gonads and prostate received doses greater than 25 mGy, but most other organs received little if any dose and therefore the effective dose was on the order of only 3-4 mSv. Therefore, organ doses are likely more meaningful for predicting future risk, such as organ specific disease, but the effective dose still offers a single number to compare the different protocols and equipment quickly and easily.

The image analysis performed in this study quantified the observed image quality for each system and imaging protocol; supplementing the extensive dosimetry measurements performed. Again, it is important to remember that the protocols selected for this study were those recommended by the manufacturer for clinical use. When first comparing the reconstructed OBI images to the XVI images, it was readily apparent that the XVI images were not as sharp and had more artifacts (streaking and rings). As mentioned in the results, the OBI outperformed the XVI in both observed resolution and low contrast detectability for all three protocols investigated, but also delivered higher doses for two of the three protocols. However, this increased image quality did not always come at the cost of higher dose, with the chest protocol for the OBI actually yielding lower dose and better image quality.

Data presented in this study shows that daily use of CBCT for patient positioning will deliver a substantial imaging dose to organs in the primary imaging field. It should be noted that

when used for daily position verification, the organ doses listed in Tables 5-4 and 5-5 must be multiplied by the total number of fractions, which can be as high as 30-40. This results in organ doses exceeding 1 Gy in some cases, such as the testes, indicating that the dose from daily CBCT imaging in a high fraction therapy regimen should be taken into consideration during the treatment planning process.

Conclusions

A comprehensive set of organ dose measurements were performed using an anthropomorphic phantom and fiber-optic coupled dosimetry system for the two commercially available kilovoltage CBCT systems (Elekta XVI and Varian OBI). The systems were evaluated by performing organ dose and image quality measurements for three clinically relevant scan sites (head, chest, and pelvis) using the latest manufacturer installed clinical protocols. Organ dose measurements demonstrated that the XVI yielded higher doses for a chest scan while the OBI yielded higher doses for both head and pelvis scans. The dosimetric differences between these two CBCT systems are magnified over the course of a fractionated treatment with daily imaging. Specifically, the XVI chest scan delivers a dose 30 cGy higher to the lung than the OBI chest scan during a 30 fraction regimen. For head and pelvis scans, the OBI delivers a dose 6.9 cGy higher to the brain and 16.8 cGy higher to the gonads, respectively, over the course of a 30 fraction regimen. Image quality measurements demonstrated that the OBI provided superior image quality, with both better spatial resolution and low contrast detectability when using default clinical protocols. Results also showed a decrease in organ dose for the OBI when compared to previous studies which used an earlier version of the manufacturer installed clinical protocols. The new XVI protocols yielded doses similar to previously published work, despite an increase in tube-current time product and the use of bow-tie filters. In summary, the organ doses reported in this study provide practitioners a useful measure of absorbed dose from the latest

manufacturer installed CBCT imaging protocols to weigh the added benefit of improved patient positioning against the additional radiation dose of using CBCT imaging.

Table 5-1. Nominal technical settings and measured HVLs for each imaging protocol investigated. On the XVI, F0 is the designation for no filter and F1 is the designation for a full bow-tie filter. For acquisition angle, cw means clockwise and ccw means counter-clockwise as viewed from the patient table.

Scan site	XVI			OBI		
	Head	Chest	Pelvis	Head	Chest	Pelvis
kV collimator	S20	M20	M10	-	-	-
kV filter	F0	F1	F1	Full bow-tie	Half bow-tie	Half bow-tie
kVp	100	120	120	100	110	125
mA	10	40	64	20	20	80
ms/projection	10	40	40	20	20	13
# of projections	361	643	643	360	655	655
Total mAs	36.1	1028.8	1646.1	145	262	680
Measured HVL (mm Al)	5.9	8.9	8.9	5.4	5.7	6.4
Acquisition angle	350°-190° cw	273°-269° cw	273°-269° cw	88°-292° cw/ccw	88°-92° cw/ccw	88°-92° cw/ccw
Acquisition time	~70 s	~120 s	~120 s	~30 s	~60 s	~60 s
Axial field of view (cm)	27	41	41	25	45	45
Long. field of view (cm)	26	26	12.5	18	16	16

Table 5-2. Organs investigated and number of measurement locations.

Tissue/organ	Measurement points
Brain	4
Salivary glands	6
Thyroid	1
Esophagus	6
Lung	8
Breast	2
Liver	4
Stomach	4
Colon	10
Bladder	1
Gonads (testes)	2
Bone marrow	19
Bone surface	19
Skin	2
Remainder organs	
Extrathoracic region	4
Oral mucosa	1
Thymus	1
Heart	1
Spleen	2
Adrenals	2
Gall bladder	1
Kidneys	2
Pancreas	1
Small intestine	6
Prostate	1
Other organs	
Lens	2

Table 5-3. Weight fractions of red bone marrow, A_i , and endosteum, E_i , for various locations of interest of the 50th percentile adult male hybrid phantom.

Location	A_i	E_i
Cranium	0.049	0.118
Cervical vertebrae	0.032	0.021
Humerus-proximal	0.031	0.027
Clavicles	0.011	0.007
Scapula	0.091	0.070
Ribs	0.102	0.042
Sternum	0.026	0.010
Thoracic vertebrae	0.130	0.048
Lumbar vertebrae	0.130	0.054
Os coxae	0.265	0.173
Sacrum	0.081	0.037
Femur-proximal	0.045	0.065

Table 5-4. Organ and effective doses from the Elekta XVI CBCT system.

Tissue/organ	Measured organ doses (mGy)		
	Head scan	Chest scan	Pelvis scan
Brain	0.70	0.49	-
Salivary glands	0.78	1.86	-
Thyroid	0.05	19.24	-
Esophagus	0.02	13.56	-
Lung	0.01	14.29	0.02
Breast	-	16.80	-
Liver	-	6.58	0.19
Stomach	-	4.68	0.23
Colon	-	0.40	2.04
Bladder	-	0.03	15.67
Gonads (testes)	-	-	29.00
Bone marrow (whole body)	0.07	5.14	1.05
Bone marrow (irradiated site)	0.80	12.42	5.50
Bone surface (whole body)	0.11	2.59	1.17
Bone surface (irradiated site)	0.80	12.42	5.50
Skin (whole body)	0.09	2.62	3.07
Skin (irradiated site)	1.34	14.92	27.88
Remainder organs			
Extrathoracic region	0.60	5.21	-
Oral mucosa	0.69	1.34	-
Thymus	0.01	14.29	-
Heart	-	13.87	0.10
Spleen	-	7.17	0.20
Adrenals	-	3.76	0.23
Gall bladder	-	1.83	0.28
Kidneys	-	1.20	0.31
Pancreas	-	1.21	0.33
Small intestine	-	0.28	1.06
Prostate	-	-	27.63
Other organs			
Lens	1.07	0.52	-
Effective dose (mSv)	0.04	7.15	3.73

Table 5-5. Organ and effective doses from the Varian OBI CBCT system.

Tissue/organ	Measured organ doses (mGy)		
	Head scan	Chest scan	Pelvis scan
Brain	3.01	0.14	-
Salivary glands	2.42	0.30	-
Thyroid	-	2.38	-
Esophagus	0.01	3.23	-
Lung	-	4.31	0.01
Breast	-	5.34	-
Liver	-	0.97	0.28
Stomach	-	0.74	0.30
Colon	-	-	3.26
Bladder	-	-	15.30
Gonads (testes)	-	-	34.61
Bone marrow (whole body)	0.28	1.29	1.14
Bone marrow (irradiated site)	3.45	3.27	5.77
Bone surface (whole body)	0.47	0.63	1.14
Bone surface (irradiated site)	3.45	3.27	5.77
Skin (whole body)	0.16	1.03	3.05
Skin (irradiated site)	2.39	5.85	27.77
Remainder organs			
Extrathoracic region	1.06	0.85	-
Oral mucosa	1.39	0.38	-
Thymus	-	4.83	-
Heart	-	4.50	0.08
Spleen	-	0.93	0.28
Adrenals	-	0.65	0.34
Gall bladder	-	0.14	0.52
Kidneys	-	0.08	0.59
Pancreas	-	0.06	0.52
Small intestine	-	-	1.72
Prostate	-	-	27.25
Other organs			
Lens	0.59	0.15	-
Effective dose (mSv)	0.12	1.82	4.34

Table 5-6. Results of image quality tests for manufacturer installed protocols. Resolution was evaluated by the smallest pattern that could be visually resolved in the CTP592 module and detectability was evaluated by the smallest acrylic sphere that could be visually resolved in the CTP401 module.

	Head		Chest		Pelvis	
	XVI	OBI	XVI	OBI	XVI	OBI
Resolution	> 5 lp/cm	8 lp/cm	>5 lp/cm	5 lp/cm	>5 lp/cm	5 lp/cm
Detectability	> 10 mm	10 mm	6 mm	4 mm	6 mm	4 mm

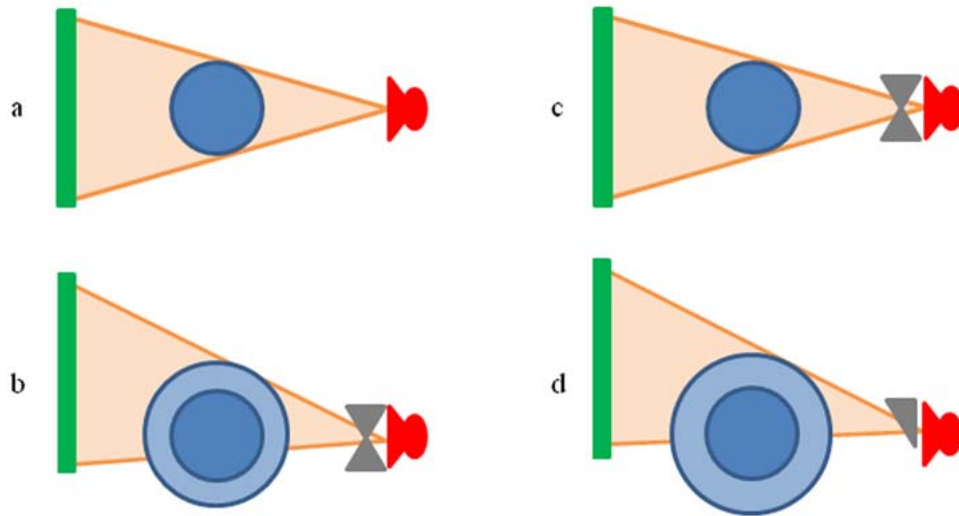


Figure 5-1. Scanning configuration for each imaging protocol used. As seen, the collimation was changed and the detector panel was shifted orthogonal to the kV beam axis when a larger FOV was required. (a) XVI head scan, no bow-tie filter, imaging panel centered, 27 cm FOV, (b) XVI chest and pelvis scan, bow-tie filter, imaging panel shifted, 41 cm FOV, (c) OBI head scan, bow-tie filter, imaging panel centered, 25 cm FOV, and (d) OBI chest and pelvis scan, half bow-tie filter, imaging panel shifted, 45 cm FOV.

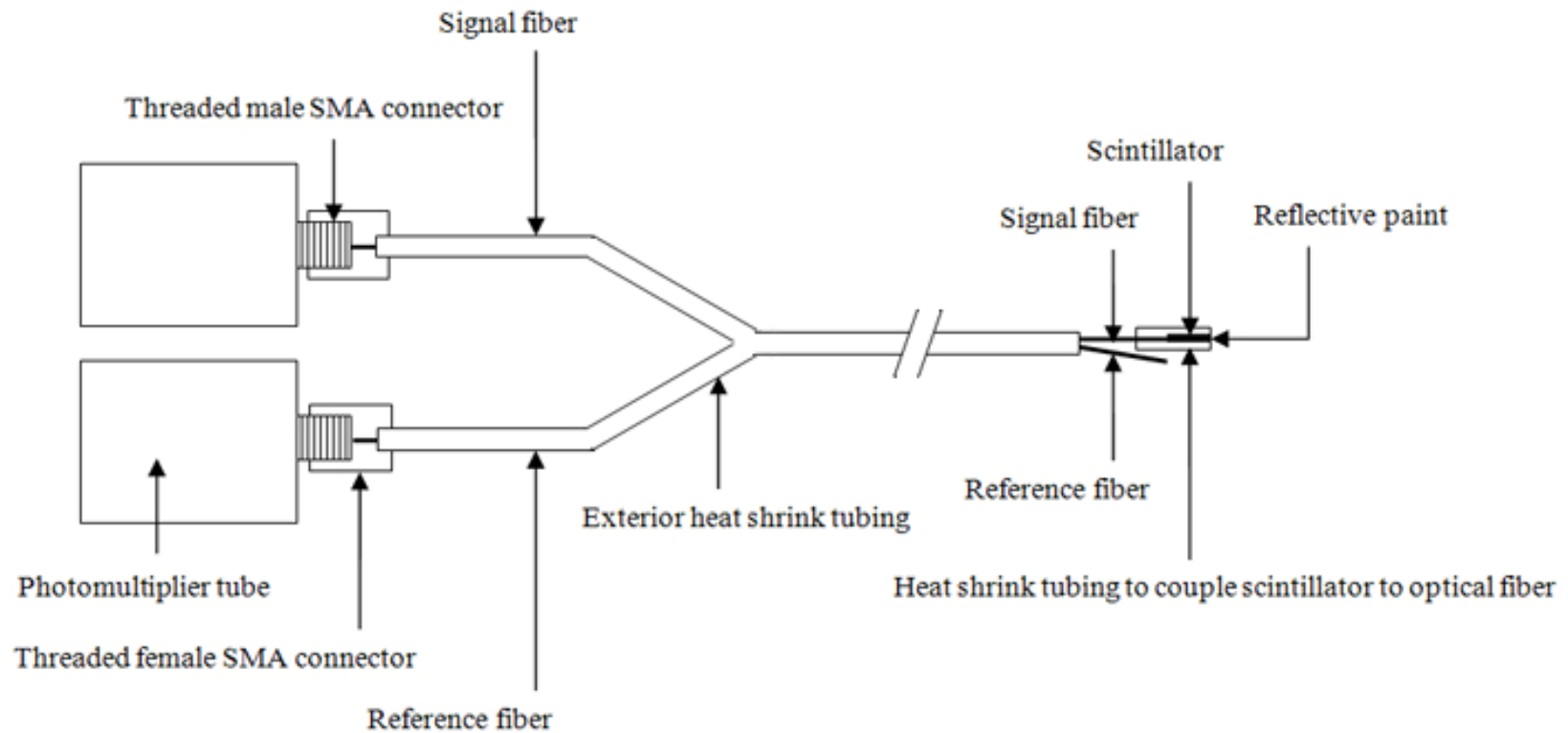


Figure 5-2. Schematic detailing the components of the dosimetry system. It should be noted that the exterior heat shrink tubing extends past the scintillator to restrict any ambient light from entering the assembly but is not shown to aid in visualization.



Figure 5-3. Axial slice of the physical phantom with an FOC dosimeter installed in the right kidney for dose measurements (displayed in prone position but phantom was oriented in supine position for measurements).

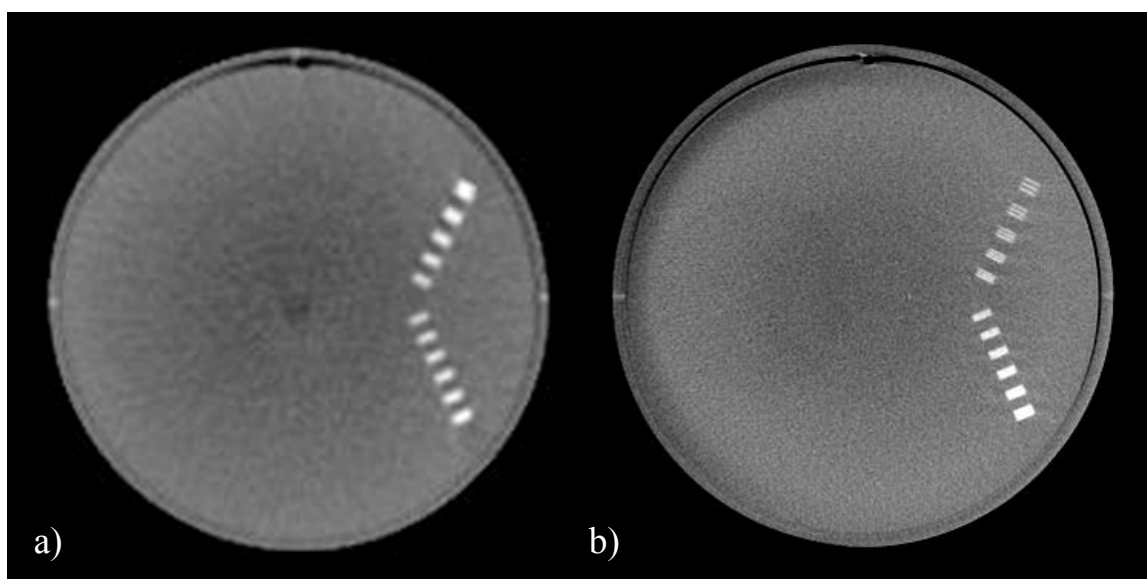


Figure 5-4. Example of reconstructed images of CTP592 resolution phantom from both a) XVI and b) OBI systems.

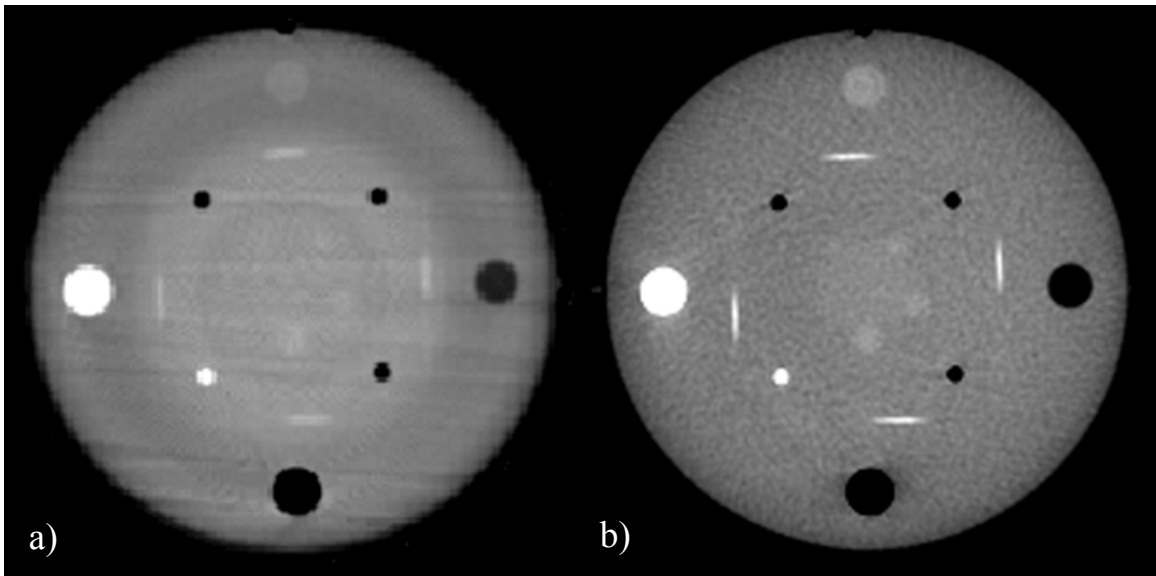


Figure 5-5. Example of reconstructed images of CTP401 low contrast phantom from both a) XVI and b) OBI systems.

CHAPTER 6
ESTIMATION OF ORGAN DOSES FROM KILOVOLTAGE CONE-BEAM CT IMAGING
USED DURING RADIOTHERAPY PATIENT POSITION VERIFICATION

Introduction

The use of gantry mounted kilovoltage cone-beam CT (CBCT) systems has gained much popularity in recent years for applications such as patient positioning, dose verification, and adaptive planning. Due to this increased popularity and demand, both Elekta and Varian now offer kilovoltage CBCT systems as an option on their medical linear accelerators, namely the X-ray Volumetric Imager (XVI[®], Elekta Oncology Systems, Crawley, UK) and the On-Board Imager (OBI[®], Varian Medical Systems, Palo Alto, CA). At our institution, both the XVI and OBI are currently used to acquire volumetric images at the time of treatment. These images are then registered with the planning CT in order to determine the appropriate shifts of the treatment table required to properly align the patient. However, the added benefit of improved patient positioning comes at the cost of additional radiation dose, which in a high fraction regimen with daily imaging can lead to a total dose on the order of a Gray or more for a number of organs.^{32, 39,}

96-98

Previously, in Chapter 5, we investigated organ doses delivered from both the XVI and OBI using factory installed protocols at three clinically relevant scan sites: head, chest, and pelvis. All organ doses were measured using an in-house adult male anthropomorphic phantom and a fiber optic coupled (FOC) dosimetry system, described in Chapters 2 and 3, respectively. While this study provided a direct measure of organ doses for estimating risk to the patient, repeating these measurements would be very time consuming, require specialized equipment, and in general would not be feasible for most clinics. Therefore, it was determined that a method of estimating CBCT organ doses from simple CT dose index (CTDI) phantom measurements

would have excellent utility; allowing clinics to estimate organ doses from their own protocols quickly and easily.

While several authors have performed CBCT dose measurements in cylindrical acrylic phantoms,^{34, 46, 94, 95, 106} very few have attempted to estimate organ doses from these measured values.^{45, 97, 98} Past estimates of CBCT organ doses have been made using the ImPACT CT dose calculator¹⁰⁷ (ImPACT, London, UK) with some success and its utility is further investigated in this study. Organ dose conversion coefficients are also developed which can be applied directly to measurements made in CTDI phantoms in order to estimate organ doses. The development and utility of these conversion coefficients is discussed in detail in the following sections.

Methods and Materials

CBCT Systems Evaluated

The imaging dose delivered from both the Elekta XVI and Varian OBI CBCT systems was evaluated in this study. A complete description of the operation of each system has been discussed in detail by Song *et al.*⁴⁶ and in Chapter 5, therefore only a brief description will follow. The two systems are similar in design with a kV x-ray source and flat-panel detector mounted to the gantry and sharing a common axis of rotation with the MV treatment beam. The XVI system utilizes collimator cassettes which are manually changed by the user depending on the FOV desired while the OBI makes use of a set of dynamic jaws to automatically adjust the collimation depending on the FOV selected. In addition, both systems utilize bow-tie filters for imaging with the exception of the XVI head scan. For each system, a total of three clinically relevant scan sites were investigated using current manufacturer installed protocols for the head, chest, and pelvis. Table 5-1 summarizes all relevant scan parameters.

Phantom Setup and Dosimetry

Cylindrical acrylic phantoms were chosen for this study due to their widespread availability and use in diagnostic radiology. Standardized by the U.S. Food and Drug Administration (FDA) and typically referred to as CTDI phantoms, these phantoms have a length of 15 cm with a diameter of 16 or 32 cm representing an adult head or body, respectively.⁴² Each phantom also has a total of five holes that run the length of the phantom in which to place an ion chamber: one in the center and four other peripheral locations 1 cm from the surface at 0°, 90°, 180°, and 270°. An image of both head and body CTDI phantoms was previously shown in Figure 1-4. During dose measurements, care was taken to align the center of each phantom to the machine isocenter using the treatment machine alignment lasers. The larger body phantom was used for all chest and pelvis protocols while the smaller head phantom was reserved for head protocols.

To perform dose measurements in the CTDI phantoms, a 100 mm pencil ion chamber (Capintec PC-4P, Ramsey, NJ) was used. The chamber and electrometer (Keithley 35050A, Cleveland, OH) were calibrated, traceable to an accredited dosimetry laboratory, for diagnostic energies and directly produced direct readings of exposure. Readings were converted to air kerma by multiplying by 0.876 cGy/R.

Cone Beam Dose Index (CBDI)

In conventional fan-beam CT, a 100 mm pencil chamber is used to collect the integrated dose profile, $D(z)$, along the longitudinal axis from a single axial slice in a CTDI phantom. This value is then normalized by the slice width, L , to estimate the multiple scan average dose (MSAD) from a series of contiguous slices for a scan length of 100 mm. This common dose metric is known as $CTDI_{100}$, where the subscript 100 refers to the length of the pencil chamber.⁴¹ The formal definition is shown in Equation 6-1.

$$\text{CTDI}_{100} = \frac{1}{L} \int_{-50\text{mm}}^{50\text{mm}} D(z) dz \quad (6-1)$$

Initially, one may think that the methodology discussed above for estimating CT dose could easily be extended to CBCT as a method of reporting radiation dose. However, due to differences in acquisition techniques, some modifications to this methodology are required. For instance, there is no need to consider the contribution of scatter from adjacent slices because CBCT is not a sequential, slice based technique like fan-beam CT but instead acquires a volumetric image in a single rotation. Additionally, the smallest longitudinal FOV from the CBCT protocols investigated in this study was 12.5 cm (see Table 5-1), exceeding the dimensions of the standard 100 mm pencil chamber. Therefore, the use of a pencil chamber in CBCT provides a measure of the average dose over the central 100 mm of the longitudinal FOV rather than the integrated dose profile of a single narrow slice like in fan-beam CT. To illustrate this point, an example of the dose profiles from the Elekta XVI chest protocol, as measured at the center and periphery of a CTDI body phantom using the fiber-optic coupled dosimeter, are shown in Figure 6-1. As can be seen, the dose profiles decrease towards the edges of the phantom due to a loss of scatter medium. The dashed vertical lines in the figure represent the edges of the theoretical 100 mm pencil chamber. By integrating the dose profiles shown in Figure 6-1 and then normalizing by the length of the theoretical pencil chamber (100 mm), we found that the average dose over the central 100 mm of the longitudinal FOV was 93.25% and 97.74% of the maximum dose at the center and periphery of the CTDI body phantom, respectively. This result confirms that the use of a 100 mm pencil chamber for CBCT slightly underestimates the maximum dose at the center of the dose profile, as previously discussed by other authors,^{45,97} but still provides a useful measure of the average dose across the central 100 mm of the FOV. As suggested by Amer *et al.*,⁴⁵ to differentiate this value from CTDI_{100} , the

integration of the dose profile over the central 100 cm of the longitudinal FOV is referred to as the cone beam dose index, CBDI_{100} . It should be noted that this value is not meant to represent the dose to a specific patient, but simply as a metric by which to quantify machine output.

The use of a farmer chamber (0.6 cc), rather than the 100 mm pencil chamber, has also been suggested by some authors for CBCT dosimetry as it provides a more accurate measurement of the maximum dose at the center of the imaging plane.^{44, 46, 108-110} Osei *et al.*¹⁰⁶ recently conducted a study comparing measured values of CBDI using both a farmer chamber and 100 mm pencil chamber and found that the readings from the farmer chamber were 2-5% higher than those from the pencil chamber. This finding supports the result discussed above from the integration of the dose profile in Figure 6-1. However, many farmer chambers employed in medical physics are used in radiation therapy and are not calibrated for kV energy beams, thus making it difficult to find a farmer chamber suitably calibrated for CBDI measurements. For this reason, a pencil chamber was chosen for all dose measurements in this study.

By performing equilibrium dose measurements of clinical protocols at both the central and peripheral locations in the CTDI phantom, an analog of the weighted CTDI (CTDI^w), which was developed to represent the average dose in the phantom, can be calculated for CBCT. To avoid confusion with CTDI^w , this analog will be referred to as the weighted cone beam dose index and is calculated as shown in Equation 6-2, where $\text{CBDI}_{100}^{\text{center}}$ and $\text{CBDI}_{100}^{\text{periphery}}$ represent the central and the average of the four peripheral dose measurements made in the CTDI phantom, respectively.

$$\text{CBDI}_{100}^w = \left(\frac{1}{3}\right)\text{CBDI}_{100}^{\text{center}} + \left(\frac{2}{3}\right)\text{CBDI}_{100}^{\text{periphery}} \quad (6-2)$$

The advantage of this metric is that it provides a single number that represents the average volumetric dose in the CTDI phantom, making it easy to quickly compare doses from different imaging protocols and equipment.

As previously mentioned, one of the primary goals of this study was to develop a methodology for estimating CBCT organ doses that could be performed using the phantoms and dosimeters currently available at most clinics. Several approaches were considered to reach this goal, but ultimately it was decided that a method for estimating organ doses based on CBDI_{100}^w would be the most intuitive and easiest to use. This is because CBDI_{100}^w , as discussed above, provides a single number that represents the average volumetric dose in the CTDI phantom for the particular protocol being investigated. Therefore, if organ doses for the corresponding protocol are known, factors referred to as organ dose conversion coefficients (ODCCs) can be developed to estimate organ doses from CBDI_{100}^w , as shown in Equation 6-3. This approach, which yields a single set of ODCCs per protocol, was thought to be simpler, and thus easier to implement clinically, than other methods considered based on specific weighting of the separate peripheral and central CBDI measurements. It should be noted that the organ doses in Equation 6-3 are from direct measurement and taken from data in Chapter 5,¹¹¹ expressed in units of mGy to tissue, and the CBDI_{100}^w values are expressed in units of mGy to air.

$$\text{ODCC} = \frac{\text{Organ dose (mGy)}_{\text{tissue}}}{\text{CBDI}_{100}^w \text{ (mGy)}_{\text{air}}} \quad (6-3)$$

In general, it is expected that interpretation of the ODCCs will be fairly intuitive. For example, it is anticipated that most organs should have an ODCC value near unity because the average volumetric dose in the CTDI phantom should be numerically similar to measured organ doses. It is also anticipated that deep organs will have a lower ODCC than peripheral organs due to the

decrease in dose with depth. Organ dose conversion coefficients developed from free-in-air measurements do not offer this intuitive advantage as free-in-air measurements will be considerably higher than in-phantom dose measurements. Following the methodology described above, ODCCs were developed for a number of in-field organs at each scan site, ultimately allowing organ doses to be estimated based on routine exposure measurements performed in cylindrical phantoms.

ImPACT Dose Calculation

The ImPACT CT patient dose calculator¹⁰⁷ uses Monte Carlo data¹¹² from a mathematical human phantom along with measured CTDI values for the particular CT system being investigated to estimate organ and effective doses. Data is entered through the ImPACT software interface where the user chooses the scanner model and inputs CTDI values, accelerating voltage, and selects the appropriate scan region on a graphical model of the mathematical phantom. The mathematical phantom used by the calculator is based on Cristy's¹¹³ adult hermaphrodite phantom with Kramer's¹¹⁴ modified neck region. In the case of CBCT, measured CDBI₁₀₀ values are substituted for CTDI₁₀₀ values as several other authors have done.^{45, 97} The current version of the calculator (version 1.0.2) has dosimetry data for over 60 single and multi-slice CT scanners built into its database. For scanners not included in the calculator's database (i.e. CBCT scanners), an empirically derived "ImPACT factor" can be calculated and used to match the new scanner to one that is included with the calculator. The ImPACT factor represents a matching parameter that provides a linear correlation between previously measured scanner data and effective dose. The equation derived by the ImPACT group for the calculation of the ImPACT factor is shown in Equation 6-4, where $CBDI_{100}^{air}$ is the cone beam dose index measured in air (no phantom) and a , b , and c are empirical factors developed by the ImPACT

group, shown in Table 6-1. It is important to note that the form of Equation 6-4 and the factors shown in Table 6-1 are not specific to CBCT systems, but can be used to match any scanner to existing data in the ImPACT calculator.

$$\text{ImPACT factor} = a * \frac{\text{CBDI}_{100}^{\text{center}}}{\text{CBDI}_{100}^{\text{air}}} + b * \frac{\text{CBDI}_{100}^{\text{periphery}}}{\text{CBDI}_{100}^{\text{air}}} + c \quad (6-4)$$

When the calculated ImPACT factor did not exactly match an existing scanner in the calculator (which was the case for the XVI and OBI), organ doses were calculated by interpolation between two scanners with the closest factors. The calculator also offers the user flexibility in defining the body region covered by the scan. Each region was carefully selected based on the protocol being investigated, with the longitudinal limits of the anatomy involved in the scan the same as those observed during organ dose measurements in Chapter 5.

Results

Measured values of CBDI_{100} for the XVI and OBI are shown in Table 6-2. All measurements were repeated 3 times to reduce statistical uncertainties and provide reproducibility metrics.

Organ doses for selected in-field organs, taken from Chapter 5, are shown in Table 6-3 along with organ dose estimates made using the ImPACT CT patient dose calculator. Organ dose conversion coefficients, calculated using Equation 6-3, are given in Table 6-4.

Discussion

The utility of the ImPACT CT patient dose calculator for estimating organ doses in CBCT was evaluated in this study. Table 6-3 shows organ dose measurements taken from Chapter 5 along with organ doses estimated using the ImPACT calculator. The majority of ImPACT estimated organ doses varied by less than 40% from the values measured in Chapter 5. While this level of variation may be acceptable for some applications, several other ImPACT estimated

organ doses varied by 100% or more. The source of these discrepancies can be traced back to several factors. For instance, the ImPACT calculator uses dosimetry data based on a mathematical phantom that represents the human body with simple geometric objects. The organ dose measurements, however, were performed using an anthropomorphic phantom constructed from tissue equivalent materials and based on a real human dataset with modifications to match the anthropometric dimensions and organ masses of a 50th percentile adult male as defined by the International Commission on Radiological Protection (ICRP).⁴⁷ The differences in the phantoms undoubtedly contribute to the observed discrepancies; however, it has been previously shown that realistic anthropomorphic phantoms provide more accurate dose estimates for human patients than mathematical phantoms such as those used by the ImPACT calculator that were originally developed for internal dosimetry applications.^{115, 116} The ImPACT calculator was also developed for fan-beam CT and assumes a full rotation of the x-ray tube around the patient. However, this is not the case with the head scans for either CBCT system examined in this study, which utilize partial rotation scans of approximately 200°. The partial rotation scans yield a dose gradient across the scan volume, causing large discrepancies between the measured organ doses and the ImPACT predicted values as seen in Table 6-3 for the head protocols. Lastly, it is worth mentioning that the dose to one organ in particular, the thymus, differed from measured values by more than 100% on both CBCT systems. The thymus is found in the chest cavity just superior to the heart, therefore it would be expected that the dose to the thymus would be similar to the dose to the heart. The measured organ doses support this prediction, while the ImPACT estimated organ doses show the thymus with a dose approximately two times greater than the dose to the heart for both systems. This discrepancy is likely due to an error with the ImPACT software. For all of the reasons discussed above, the ImPACT dose calculator is not

recommended for use with CBCT, further driving the development of organ dose conversion coefficients for CBCT.

As seen in Table 6-4, a number of in-field organs for each scan site were selected for dose estimation based on $CBDI_{100}^w$. Only in-field organs were chosen as the dose to organs out-of-field can vary widely depending on the scan isocenter. For instance, during a chest scan, if the isocenter is located in the inferior portion of the thoracic cavity, the entire liver may be in the imaging field, but if the isocenter is located in the superior portion of the thoracic cavity, the liver may be completely out of the imaging field. The organs selected for this study are centrally located in the desired scan region and as a result are in the imaging field for a wide range of typical isocenters. The end user is still cautioned in the use of these organ dose conversion coefficients as their accuracy depends on the organ being entirely in the imaging field. This can be ensured by considering the scan isocenter and longitudinal beam width of the scan to be performed.

As previously mentioned, to reduce dose and scanning time, both the XVI and OBI use partial rotation scans for their head protocols (see Table 5-1). When the patient is placed in a supine position, image acquisition for the XVI begins at the anterior surface and rotates around the left lateral side of the head, finishing posteriorly. For the OBI, image acquisition moves from left to right lateral (or vice-versa) while rotating around the posterior surface of the patient. This leads to an asymmetrical dose distribution around the periphery of the CTDI phantom, with the XVI delivering a maximum air kerma of 1.6 mGy at 90° and a minimum air kerma of 0.47 mGy at 270° while the OBI delivers a maximum air kerma of 7.99 mGy at 180° and a minimum air kerma of 1.8 mGy at 0° (angles are as viewed from the patient table and looking at the gantry). Using this data, along with Equation 6-2, $CBDI_{100}^w$ was calculated and is shown in Table 6-2 for

both the XVI and OBI. These values, along with Equation 6-3 were then used to calculate organ dose conversion coefficients which are shown in Table 6-4. As can be seen in Table 6-4, the organ dose conversion coefficients are less than unity for almost all of the organs, representing a situation in which the organ doses are less than $CBDI_{100}^w$. This is due to the fact that almost all of the organs are located near the anterior surface of the head and, as discussed before, image acquisition of the partial rotation scans used are centered around the lateral or posterior surfaces of the head for the XVI and OBI, respectively. Therefore, the dose on the anterior surface of the head is lower than the average volumetric dose in the CTDI phantom, represented by $CBDI_{100}^w$.

The chest and pelvis protocols for both imaging systems use full rotation scans during image acquisition. This leads to a more uniform dose distribution around the periphery of the CTDI phantom, as illustrated in Table 6-2. The organ dose conversion coefficients for each imager and protocol are also shown in Table 6-4. Most of the organ dose conversion coefficients for the chest exams are less than unity except for the breast. This was expected because the organs in the chest cavity are deep to the surface of the body, resulting in organ doses that are less than $CBDI_{100}^w$, which again, represents the average volumetric dose in the CTDI phantom. There is also a general trend that the XVI organ dose conversion coefficients are larger than the OBI organ dose conversion coefficients for the chest protocol. This can be explained due to a loss of scatter dose contribution due to the limited length of the CTDI phantom (15 cm). The XVI utilizes a longitudinal FOV of 26 cm for its chest protocol while the longitudinal FOV for the OBI is only 16 cm. Because of this, the measured CBDI values for the XVI will underestimate the equilibrium dose (as measured with an infinitely long phantom) to a greater extent than the OBI system.¹¹⁰ The magnitude of this effect has been explored by Amer *et al.*⁴⁵ This same effect is not seen during organ dose measurements in the anthropomorphic phantom as

the length of the phantom exceeds the beam width of both systems. Therefore, the net result is the organ dose conversion coefficients for the XVI generally being larger than those for the OBI. The exact opposite is true for the pelvis exam, where the OBI now uses a larger longitudinal FOV than the XVI and all of the OBI organ dose conversion coefficients are slightly larger than those for the XVI.

The organ dose conversion coefficients given in this study were developed using the current factory installed clinical protocols for the XVI and OBI systems. Future optimization of these protocols could lead to changes in the technical settings that may or may not affect the applicability of these coefficients. Changes that affect the overall tube-current time product (i.e. mA, ms/projections, total number of projections) are expected to scale linearly with dose and therefore the ODCC values should still be applicable. However, changes to the tube voltage or acquisition angles would change the dose distribution in the phantoms and would require further investigation.

Conclusions

This work reports on the methodology developed for estimating organ doses for two popular kilovoltage CBCT systems using readily available clinical equipment. Organ dose conversion coefficients are introduced and calculated by taking a ratio of organ doses previously measured in Chapter 5 and the weighted cone beam dose index measured using the same clinical protocols. For completeness, conversion coefficients were calculated for both the XVI and OBI systems at three clinically relevant scan sites: head, chest, and pelvis. Only in-field organs were included in this study as the dose to out-of-field organs is much lower and can vary greatly depending on the scan isocenter and patient anatomy. The utility of the ImPACT CT patient dose calculator was also investigated, and while it offered great flexibility in dose calculations, it was found that dose estimates made with the calculator showed a large range of variation from values

previously measured in Chapter 5, demonstrating its limitations for use with CBCT. The organ dose conversion coefficients introduced in this work, however, allow organ doses from CBCT to easily and accurately be estimated using simple measurements performed in CTDI phantoms.

Table 6-1. Empirical ImPACT factors and normalized CBDI values for use with Equation 6-4.

Empirical factors	XVI			OBI		
	Head	Chest	Pelvis	Head	Chest	Pelvis
<i>a</i>	0.4738	3.5842		0.4738	3.5842	
<i>b</i>	0.8045	0.6328		0.8045	0.6328	
<i>c</i>	0.0752	-0.0902		0.0752	-0.0902	
$CBDI_{100}^{center}$ [mGy _{air} /100mAs]	2.34	1.10	1.00	3.68	1.48	2.11
$CBDI_{100}^{periphery}$ [mGy _{air} /100mAs]	2.92	1.87	1.70	3.51	2.78	3.70
$CBDI_{100}^{air}$ [mGy _{air} /100mAs]	3.42	4.27	4.31	6.62	8.09	10.58
$CBDI_{100}^w$ [mGy _{air} /100mAs]	2.73	1.62	1.47	3.57	2.34	3.17
ImPACT factor	1.09	1.11	0.99	0.77	0.78	0.85

Table 6-2. Measured CBDI values (in mGy_{air}) ± 1σ. Angles used to define peripheral measurements are viewed from the foot of the patient table looking toward the gantry.

	XVI			OBI		
	Head	Chest	Pelvis	Head	Chest	Pelvis
$CBDI_{100}^{center}$	0.84 ± 0.01	11.34 ± 0.04	16.38 ± 0.04	5.34 ± 0.04	3.89 ± 0.03	14.38 ± 0.32
$CBDI_{100}^{periphery}$	1.05 ± 0.01	19.26 ± 0.06	28.01 ± 0.12	5.09 ± 0.03	7.27 ± 0.02	25.17 ± 0.13
Edge (0°)	1.05 ± 0.02	19.45 ± 0.00	28.85 ± 0.13	1.80 ± 0.04	7.32 ± 0.04	25.43 ± 0.41
Edge (90°)	1.60 ± 0.01	19.01 ± 0.19	28.18 ± 0.22	4.79 ± 0.03	7.28 ± 0.03	25.49 ± 0.09
Edge (180°)	1.10 ± 0.02	18.50 ± 0.11	26.67 ± 0.04	7.99 ± 0.10	7.22 ± 0.04	25.05 ± 0.18
Edge (270°)	0.47 ± 0.01	20.08 ± 0.13	28.32 ± 0.40	5.77 ± 0.08	7.26 ± 0.04	24.70 ± 0.23
$CBDI_{100}^w$	0.98 ± 0.01	16.62 ± 0.05	24.13 ± 0.08	5.17 ± 0.03	6.14 ± 0.02	21.57 ± 0.14

Table 6-3. Measured organ doses, in mGy_{tissue}, taken from Chapter 5, along with organ dose estimates made using the ImPACT CT patient dose calculator, also in mGy_{tissue}.

	XVI			OBI		
	Hyer <i>et al.</i>	ImPACT	% difference	Hyer <i>et al.</i>	ImPACT	% difference
Head scan						
Brain	0.70	0.77	10.5%	3.01	3.78	25.6%
Lens	1.07	0.80	-25.6%	0.59	3.84	551.2%
Extrathoracic region	0.60	0.05	-91.2%	1.06	0.08	-92.9%
Oral mucosa	0.69	0.77	12.1%	1.39	3.78	172.0%
Salivary glands	0.78	0.77	-0.9%	2.42	3.78	56.2%
Chest scan						
Lung	14.29	19.30	35.1%	4.31	6.81	58.0%
Thymus	14.29	28.65	100.5%	4.83	10.66	120.7%
Heart	13.87	14.65	5.6%	4.50	5.07	12.8%
Breast	16.80	21.30	26.8%	5.34	7.95	48.8%
Pelvis scan						
Bladder	15.67	19.56	24.8%	15.30	21.63	41.4%
Prostate	27.63	19.56	-29.2%	27.25	21.63	-20.6%
Gonads	29.00	21.56	-25.7%	34.61	20.78	-40.0%

Table 6-4. Organ dose conversion coefficients, in $\text{mGy}_{\text{tissue}}/\text{mGy}_{\text{air}}$, for each protocol calculated using Equation 6-3.

	XVI	OBI
Head scan		
Brain	0.71	0.58
Lens	1.09	0.11
Extrathoracic region	0.61	0.20
Oral mucosa	0.70	0.27
Salivary glands	0.79	0.47
Chest scan		
Lung	0.86	0.70
Thymus	0.86	0.79
Heart	0.83	0.73
Breast	1.01	0.87
Pelvis scan		
Bladder	0.65	0.71
Prostate	1.14	1.26
Gonads	1.20	1.60

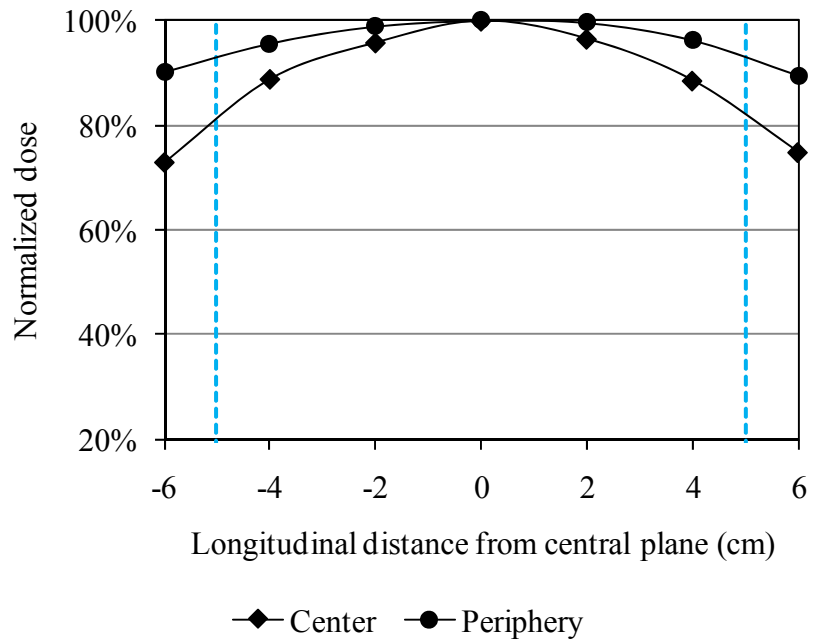


Figure 6-1. Dose profiles from XVI chest protocol as measured at the center and periphery of a CTDI body phantom. Dashed vertical lines mark the boundaries of the 100 mm pencil chamber when centered in the phantom.

CHAPTER 7 CONCLUSION

Results of this Work

The overall goal of this work was to develop the tools and methods necessary to quantify organ doses in radiation therapy from kilovoltage cone-beam computed tomography (CBCT). This is an important issue as current literature on this topic is very limited and does not address the latest scanning techniques and protocols used by the manufacturers. To facilitate organ dose measurements in CBCT and reach the overall goal of this work, several tools were developed including an anthropomorphic phantom representing a 50th percentile adult male and a fiber-optic coupled (FOC) dosimetry system. These tools were used for the direct measurement of organ doses delivered from both the Elekta XVI and Varian OBI cone-beam CT (CBCT) systems. For each system, organ doses were measured using the latest manufacturer installed clinical protocols for scanning the head, chest, and pelvis. Results shown in Chapter 5 indicate that the total organ dose could exceed 1 Gy to a number of organs during a fractionated radiotherapy treatment with daily imaging. While this dose is considerably less than the treatment dose, it is still of concern as the volume of tissue imaged with CBCT is much larger than the volume of tissue treated with the megavoltage beam. The measured organ doses along with tissue weighting factors from ICRP 103⁴⁸ were also used to calculate a reference male effective dose. The effective dose provides a single parameter to quickly and easily compare the patient dose from different imaging systems and scan protocols.

The cone-beam dose index (CBDI) was also measured for the same clinical protocols using standard CTDI head and body phantoms along with a 100 mm pencil chamber. A ratio of measured organ doses to the weighted CBDI was then taken in order to develop organ dose conversion coefficients (ODCCs), given in Chapter 6. These conversion coefficients allow organ

doses to be easily estimated without the need to repeat time consuming anthropomorphic phantom organ dose measurements for future changes in technical settings of scan protocols.

As a result of this dissertation, organ doses from current clinical protocols are now available in the literature along with a method to estimate organ doses from simple measurements of the weighted CDBI. This research also paves the way for future dosimetry studies in diagnostic radiology with the construction of the anthropomorphic phantom and FOC dosimetry system. Some proposed future studies are discussed in the next section.

Opportunities for Future Work and Development

Anthropomorphic Phantom Development

The phantom built for this study represents a 50th percentile adult male as defined by ICRP publication 89.⁴⁷ The methods described in Chapter 2 that were used to build this phantom can also be used to construct a phantom of any size from a segmented image set. The construction of an additional male and female phantom has already been carried out by our research group using these techniques and the development of a “fat suit” is currently underway. The “fat suit” is constructed in axial slices using a newly developed adipose tissue-equivalent substitute (ATES) and is designed to wrap around the exterior of the existing 50th percentile male phantom in order to represent subcutaneous fat and match the anthropometric dimensions of a 90th percentile adult male. Another interesting project is the development of physical phantoms that represent pregnant females at different stages of gestational development. These phantoms could be used to estimate doses to the fetus by direct measurement and are currently being explored by our research group. Incorporating breasts made of a breast tissue-equivalent substitute onto the female phantom is also currently being investigated.

Lastly, constructing a phantom in coronal slices rather than axial slices has been discussed. This would eliminate the problems associated with holding the phantom together on the patient

table during CT studies. Coronal slices would also allow FOC dosimeters to be inserted with the sensitive element oriented parallel to the axis of rotation of the CT scanner, reducing the observed effects of angular dependence. The drawback of constructing a coronal phantom as compared to an axial phantom is the increased size of each slice. With our current engraving system, it is not possible to create molds of the size required for a coronal phantom. It is anticipated that future equipment upgrades may overcome this issue.

Fiber-optic Coupled (FOC) Dosimetry System

After performing the organ dose study in Chapter 5, it was painfully obvious that more channels on the dosimetry system were needed. Currently, only two dosimeters can be read-out simultaneously with the PMT array. With more than 100 measurement points required to characterize the dose to all organs, the process was very slow. A new system capable of reading out 20-30 dosimeters simultaneously would make future organ dose studies much more efficient; requiring far fewer scans to acquire all of the data needed while still not being too cumbersome to operate. To add this many channels to the current system is not financially feasible as PMTs sell for approximately \$2200 each and one dosimeter requires a total of two PMTs (one for the reference fiber and one for the signal fiber). A viable low-cost alternative to the expensive PMT array is a CCD camera. Several authors have investigated using CCD cameras for reading out FOC dosimeters with promising results at both kV and MV energies.^{89,92} Our group is currently investigating the best camera for our application along with methods to couple dosimeters to the CCD camera.

Characterizing the FOC dosimeter for other types and energies of radiation is also desired. To date, the FOC dosimeter has only been fully characterized at diagnostic energies, as discussed in Chapter 3. Some work at megavoltage energies was also performed, as discussed in Chapter 4. To overcome the issues presented in Chapter 4, our group is currently investigating methods to

better discriminate against Cerenkov radiation produced at megavoltage energies. These methods are mainly focused on spectral discrimination using a color CCD camera. Work has also begun in characterizing the dosimeter for neutron fields and preliminary results are positive.

CBCT Dosimetry

One of the main advantages of the anthropomorphic phantom used in this work is that it also has a computational twin phantom, previously shown in Figure 2-1. This allows dose measurements performed in the physical phantom to serve as a direct comparison to simulated doses in the computational phantom for the experimental validation of Monte Carlo codes. Ultimately, it is hoped that simulations of each CBCT system can be created and validated using the data given in this work. Once the Monte Carlo simulations are ready, organ dose studies for patients of different sizes can be completed. Currently, the ALRADS (Advanced Laboratory for Radiation Dosimetry Studies) group at the University of Florida has 50 adult phantoms representing males and females of 10th through 90th percentile height and weight.¹¹⁷ Simulations performed using this phantom library would provide dose data for patients of nearly any size. Simulations could also be performed to account for different scan isocenters or to investigate future changes in the scan parameters.

Data from these Monte Carlo simulations could eventually be incorporated into an organ dose database for CBCT. It would be desirable for the database to be integrated into a spreadsheet that displays dose information based on user inputs such as CBCT system used (XVI or OBI), technical scan settings, scan isocenter, and the patient's height and weight. It is believed that this organ dose database would have excellent utility in radiation therapy, allowing pre-calculated organ doses for patients of nearly any size to be quickly retrieved. Ultimately, software could be written to couple this organ dose database with treatment planning software allowing the imaging dose from CBCT to be taken into account during treatment planning.

Final Thoughts

The research presented in this dissertation quantifies imaging doses delivered from kilovoltage CBCT systems used in radiation therapy, namely the Elekta XVI and Varian OBI. Despite the fact that it is becoming common for patients to receive a CBCT at every treatment fraction, current literature on this topic is very limited. This work addresses this problem by developing the tools and methods necessary to accurately quantify organ doses from CBCT imaging. Organ dose measurements were performed for clinically relevant scans and the results have been published in the literature.¹¹⁸ It is hoped that the tools developed in this study find many other useful applications and continue to contribute to the field of medical physics.

LIST OF REFERENCES

1. K. W. Kinzler and B. Vogelstein, *The genetic basis of human cancer*, 2nd ed. (McGraw-Hill, New York, 2002).
2. K. S. Saladin, *Anatomy & physiology: The unity of form and function*, 3rd ed. (McGraw-Hill, New York, 2004).
3. American Cancer Society, "Cancer Facts & Figures 2009," Atlanta: American Cancer Society (2009).
4. E. B. Podgorsak, *Radiation oncology physics: A handbook for teachers and students*. (International Atomic Energy Agency, Vienna, 2005).
5. P. Cheung, K. Sixel, G. Morton, D. A. Loblaw, R. Tirona, G. Pang, R. Choo, E. Szumacher, G. Deboer and J. P. Pignol, "Individualized planning target volumes for intrafraction motion during hypofractionated intensity-modulated radiotherapy boost for prostate cancer," *Int J Radiat Oncol Biol Phys* **62**, 418-425 (2005).
6. T. Kron, "Reduction of margins in external beam radiotherapy," *J Med Phys* **33** (2008).
7. P. J. Rossi, E. Schreiber, A. B. Jani, V. A. Master and P. A. Johnstone, "Boost first, eliminate systematic error, and individualize CTV to PTV margin when treating lymph nodes in high-risk prostate cancer," *Radiation Oncol* **90**, 353-358 (2009).
8. B. Schaly, G. S. Bauman, W. Song, J. J. Battista and J. Van Dyk, "Dosimetric impact of image-guided 3D conformal radiation therapy of prostate cancer," *Phys Med Biol* **50**, 3083-3101 (2005).
9. W. Song, B. Schaly, G. Bauman, J. Battista and J. Van Dyk, "Image-guided adaptive radiation therapy (IGART): Radiobiological and dose escalation considerations for localized carcinoma of the prostate," *Med Phys* **32**, 2193-2203 (2005).
10. D. J. Little, L. Dong, L. B. Levy, A. Chandra and D. A. Kuban, "Use of portal images and BAT ultrasonography to measure setup error and organ motion for prostate IMRT: implications for treatment margins," *Int J Radiat Oncol Biol Phys* **56**, 1218-1224 (2003).
11. E. J. Hall and A. J. Giaccia, *Radiobiology for the radiologist*, 6th ed. (Lippincott Williams & Wilkins, Philadelphia, 2005).
12. J. M. Balter and Y. Cao, "Advanced technologies in image-guided radiation therapy," *Semin Radiat Oncol* **17**, 293-297 (2007).
13. J. M. Balter and M. L. Kessler, "Imaging and alignment for image-guided radiation therapy," *J Clin Oncol* **25**, 931-937 (2007).

14. L. A. Dawson and D. A. Jaffray, "Advances in image-guided radiation therapy," *J Clin Oncol* **25**, 938-946 (2007).
15. C. C. Ling, E. Yorke and Z. Fuks, "From IMRT to IGRT: frontierland or neverland?," *Radiother Oncol* **78**, 119-122 (2006).
16. L. Xing, B. Thorndyke, E. Schreibmann, Y. Yang, T. F. Li, G. Y. Kim, G. Luxton and A. Koong, "Overview of image-guided radiation therapy," *Med Dosim* **31**, 91-112 (2006).
17. L. E. Antonuk, "Electronic portal imaging devices: a review and historical perspective of contemporary technologies and research," *Phys Med Biol* **47**, R31-65 (2002).
18. A. L. Boyer, L. Antonuk, A. Fenster, M. Van Herk, H. Meertens, P. Munro, L. E. Reinstein and J. Wong, "A review of electronic portal imaging devices (EPIDs)," *Med Phys* **19**, 1-16 (1992).
19. L. A. Dawson and M. B. Sharpe, "Image-guided radiotherapy: rationale, benefits, and limitations," *Lancet Oncol* **7**, 848-858 (2006).
20. M. van Herk, "Different styles of image-guided radiotherapy," *Semin Radiat Oncol* **17**, 258-267 (2007).
21. D. Verellen, M. De Ridder and G. Storme, "A (short) history of image-guided radiotherapy," *Radiother Oncol* **86**, 4-13 (2008).
22. D. Verellen, M. D. Ridder, N. Linthout, K. Tournel, G. Soete and G. Storme, "Innovations in image-guided radiotherapy," *Nat Rev Cancer* **7**, 949-960 (2007).
23. C. Amies, A. Bani-Hashemi, J. C. Celi, G. Grousset, F. Ghelmansarai, D. Hristov, D. Lane, M. Mitschke, A. Singh, H. Shukla, J. Stein and M. Wofford, "A multi-platform approach to image guided radiation therapy (IGRT)," *Med Dosim* **31**, 12-19 (2006).
24. L. A. Feldkamp and L. C. Davis, "Practical conebeam algorithm," *J Opt Soc Am A* **1**, 612-619 (1984).
25. J. Pouliot, A. Bani-Hashemi, J. Chen, M. Svatos, F. Ghelmansarai, M. Mitschke, M. Aubin, P. Xia, O. Morin, K. Bucci, M. Roach, 3rd, P. Hernandez, Z. Zheng, D. Hristov and L. Verhey, "Low-dose megavoltage cone-beam CT for radiation therapy," *Int J Radiat Oncol Biol Phys* **61**, 552-560 (2005).
26. M. Broderick, G. Menezes, M. Leech, M. Coffey and R. Appleyard, "A comparison of kilovoltage and megavoltage cone beam CT in radiotherapy," *J Radiother Pract* **6**, 173-178 (2007).
27. C. W. Cheng, J. Wong, L. Grimm, M. Chow, M. Uematsu and A. Fung, "Commissioning and clinical implementation of a sliding gantry CT scanner installed in an existing treatment room and early clinical experience for precise tumor localization," *Am J Clin Oncol* **26**, e28-36 (2003).

28. K. Kuriyama, H. Onishi, N. Sano, T. Komiyama, Y. Aikawa, Y. Tateda, T. Araki and M. Uematsu, "A new irradiation unit constructed of self-moving gantry-CT and linac," *Int J Radiat Oncol Biol Phys* **55**, 428-435 (2003).
29. C. M. Ma and K. Paskalev, "In-room CT techniques for image-guided radiation therapy," *Med Dosim* **31**, 30-39 (2006).
30. M. V. Herk, D. Jaffray, A. Betgen, P. Remeijer, J. Sonke, M. Smitsmans, L. Zijp and J. Lebesque, "First clinical experience with cone-beam CT guided radiation therapy; Evaluation of dose and geometric accuracy," *Int J Radiat Oncol Biol Phys* **60**, S196 (2004).
31. C. A. McBain, A. M. Henry, J. Sykes, A. Amer, T. Marchant, C. M. Moore, J. Davies, J. Stratford, C. McCarthy, B. Porritt, P. Williams, V. S. Khoo and P. Price, "X-ray volumetric imaging in image-guided radiotherapy: the new standard in on-treatment imaging," *Int J Radiat Oncol Biol Phys* **64**, 625-634 (2006).
32. N. Wen, H. Guan, R. Hammoud, D. Pradhan, T. Nurushev, S. Li and B. Movsas, "Dose delivered from Varian's CBCT to patients receiving IMRT for prostate cancer," *Phys Med Biol* **52**, 2267-2276 (2007).
33. O. Morin, A. Gillis, M. Aubin, J. F. Aubry, J. Chen, H. Chen, M. Descovich and J. Pouliot, "Adaptive radiation therapy using megavoltage cone-beam CT," *IFMBE Proceedings* **14**, 1780-1784 (2006).
34. M. K. Islam, T. G. Purdie, B. D. Norrlinger, H. Alasti, D. J. Moseley, M. B. Sharpe, J. H. Siewerdsen and D. A. Jaffray, "Patient dose from kilovoltage cone beam computed tomography imaging in radiation therapy," *Med Phys* **33**, 1573-1582 (2006).
35. M. A. Hill, "The variation in biological effectiveness of X-rays and gamma rays with energy," *Radiat Prot Dosimetry* **112**, 471-481 (2004).
36. J. Lehmann, J. Perks, S. Semon, R. Harse and J. A. Purdy, "Commissioning experience with cone-beam computed tomography for image-guided radiation therapy," *J Appl Clin Med Phys* **8**, 2354 (2007).
37. W. D. Renner, K. Norton and T. Holmes, "A method for deconvolution of integrated electronic portal images to obtain incident fluence for dose reconstruction," *J Appl Clin Med Phys* **6**, 22-39 (2005).
38. International Commission on Radiological Protection, "Recommendations of the International Commission on Radiological Protection," *ICRP Publication 60* (1991).
39. M. W. Kan, L. H. Leung, W. Wong and N. Lam, "Radiation dose from cone beam computed tomography for image-guided radiation therapy," *Int J Radiat Oncol Biol Phys* **70**, 272-279 (2008).

40. J. T. Bushberg, J. A. Seibert, E. M. Leidholdt and J. M. Boone, *The essential physics of medical imaging*, 2nd ed. (Lippincott Williams and Wilkins, Philadelphia, 2002).
41. C. McCollough, D. Cody, S. Edyvean, R. Geise, B. Gould, N. Keat, W. Huda, P. Judy, W. Kalender, M. McNitt-Gray, R. Morin, T. Payne, S. Stern, L. Rothenberg, P. Shrimpton, J. Timmer and C. Wilson, "The measurement, reporting, and management of radiation dose in CT," AAPM Report 96 - TG 23 (2008).
42. Food and Drug Administration, "Diagnostic x-ray systems and their major components," 21 CFR 1020.33 (1984).
43. J. M. Boone, "The trouble with CTD100," *Med Phys* **34**, 1364-1371 (2007).
44. R. Fahrig, R. Dixon, T. Payne, R. L. Morin, A. Ganguly and N. Strobel, "Dose and image quality for a cone-beam C-arm CT system," *Med Phys* **33**, 4541-4550 (2006).
45. A. Amer, T. Marchant, J. Sykes, J. Czajka and C. Moore, "Imaging doses from the Elekta Synergy X-ray cone beam CT system," *Br J Radiol* **80**, 476-482 (2007).
46. W. Y. Song, S. Kamath, S. Ozawa, S. A. Ani, A. Chvetsov, N. Bhandare, J. R. Palta, C. Liu and J. G. Li, "A dose comparison study between XVI and OBI CBCT systems," *Med Phys* **35**, 480-486 (2008).
47. International Commission on Radiological Protection, "Basic anatomical and physiological data for use in radiological protection - reference values," ICRP Publication 89, *Annals of the ICRP* **32**, 1-277 (2002).
48. International Commission on Radiological Protection, "2007 recommendations of the International Commission on Radiological Protection," ICRP Publication 103, *Annals of the ICRP* **37**, 1-332 (2007).
49. L. M. Hurwitz, T. T. Yoshizumi, P. C. Goodman, D. P. Frush, G. Nguyen, G. Toncheva and C. Lowry, "Effective dose determination using an anthropomorphic phantom and metal oxide semiconductor field effect transistor technology for clinical adult body multidetector array computed tomography protocols," *J Comput Assist Tomogr* **31**, 544-549 (2007).
50. R. J. Staton, A. K. Jones, C. Lee, D. E. Hintenlang, M. M. Arreola, J. L. Williams and W. E. Bolch, "A tomographic physical phantom of the newborn child with real-time dosimetry. II. Scaling factors for calculation of mean organ dose in pediatric radiography," *Med Phys* **33**, 3283-3289 (2006).
51. J. F. Winslow, D. E. Hyer, R. F. Fisher, C. J. Tien and D. E. Hintenlang, "Construction of anthropomorphic phantoms for use in dosimetry studies," *J Appl Clin Med Phys* **10**, 195-204 (2009).
52. D. R. White, "The formulation of tissue substitute materials using basic interaction data," *Phys Med Biol* **22**, 889-899 (1977).

53. D. R. White, R. J. Martin and R. Darlison, "Epoxy resin based tissue substitutes," *Br J Radiol* **50**, 814-821 (1977).
54. A. K. Jones, D. E. Hintenlang and W. E. Bolch, "Tissue-equivalent materials for construction of tomographic dosimetry phantoms in pediatric radiology," *Med Phys* **30**, 2072-2081 (2003).
55. R. F. Fisher, University of Florida, 2006.
56. J. L. Hurtado, C. Lee, D. Lodwick, T. Goede, J. L. Williams and W. E. Bolch, "Hybrid computational phantoms representing the 50th percentile male and female adult: construction and applications for retrospective dosimetry," *Health Phys* (2009).
57. C. Lee, D. Lodwick, D. Hasenauer, J. L. Williams and W. E. Bolch, "Hybrid computational phantoms of the male and female newborn patient: NURBS-based whole-body models," *Phys Med Biol* **52**, 3309-3333 (2007).
58. C. Lee, D. Lodwick, J. L. Williams and W. E. Bolch, "Hybrid computational phantoms of the 15-year male and female adolescent: applications to CT organ dosimetry for patients of variable morphometry," *Med Phys* **35**, 2366-2382 (2008).
59. J. B. Sessions, J. N. Roshau, M. A. Tressler, D. E. Hintenlang, M. M. Arreola, J. L. Williams, L. G. Bouchet and W. E. Bolch, "Comparisons of point and average organ dose within an anthropomorphic physical phantom and a computational model of the newborn patient," *Med Phys* **29**, 1080-1089 (2002).
60. International Commission on Radiation Units and Measurement, "Tissue substitutes in radiation dosimetry and measurement," ICRU Report 44 (1989).
61. D. R. White, C. Constantinou and R. J. Martin, "Foamed epoxy resin-based lung substitutes," *Br J Radiol* **59**, 787-790 (1986).
62. M. Cristy and K. Eckermann, "Specific absorbed fractions of energy at various ages from internal photon sources," Oak Ridge National Laboratory, ORNL/TM-8381/VI-VII (1987).
63. A. K. Jones, T. A. Simon, W. E. Bolch, M. M. Holman and D. E. Hintenlang, "Tomographic physical phantom of the newborn child with real-time dosimetry I. Methods and techniques for construction," *Med Phys* **33**, 3274-3282 (2006).
64. L. Struelens, F. Vanhavere and K. Smans, "Experimental validation of Monte Carlo calculations with a voxelized Rando-Alderson phantom: a study on influence parameters," *Phys Med Biol* **53**, 5831-5844 (2008).
65. J. M. Edmund and C. E. Anderson, "Temperature dependence of the $\text{Al}_2\text{O}_3:\text{C}$ response in medical luminescence dosimetry," *Radiat Meas* **42**, 177-189 (2007).

66. L. A. Benevides and D. E. Hintenlang, "Characterization of metal oxide semiconductor field effect transistor dosimeters for application in clinical mammography," *Med Phys* **33**, 514-520 (2006).
67. T. Aoyama, S. Koyama and C. Kawaura, "An in-phantom dosimetry system using pin silicon photodiode radiation sensors for measuring organ doses in x-ray CT and other diagnostic radiology," *Med Phys* **29**, 1504-1510 (2002).
68. L. A. Benevides, A. L. Huston, B. L. Justus, P. Falkenstein, L. F. Brateman and D. E. Hintenlang, "Characterization of a fiber-optic-coupled radioluminescent detector for application in the mammography energy range," *Med Phys* **34**, 2220-2227 (2007).
69. A. K. Jones and D. Hintenlang, "Potential clinical utility of a fibre optic-coupled dosimeter for dose measurements in diagnostic radiology," *Radiat Prot Dosimetry* **132**, 80-87 (2008).
70. B. L. Justus, P. Falkenstein, A. L. Huston, M. C. Plazas, H. Ning and R. W. Miller, "Gated fiber-optic-coupled detector for in vivo real-time radiation dosimetry," *Appl Opt* **43**, 1663-1668 (2004).
71. F. Lacroix, L. Archambault, L. Gingras, M. Guillot, A. S. Beddar and L. Beaulieu, "Clinical prototype of a plastic water-equivalent scintillating fiber dosimeter array for QA applications," *Med Phys* **35**, 3682-3690 (2008).
72. M. R. Arnfield, "Radiation-induced light in optical fibers and plastic scintillators: Application to brachytherapy dosimetry," *IEEE Trans Nucl Sci* **43**, 2077-2084 (1996).
73. G. Ayotte, L. Archambault, L. Gingras, F. Lacroix, A. S. Beddar and L. Beaulieu, "Surface preparation and coupling in plastic scintillator dosimetry," *Med Phys* **33**, 3519-3525 (2006).
74. J. Elsey, D. R. McKenzie, J. Lambert, N. Suchowerska, S. L. Law and S. C. Fleming, "Optimal coupling of light from a cylindrical scintillator into an optical fiber," *Appl Opt* **46**, 397-404 (2007).
75. C. J. Marckmann, M. C. Aznar, C. E. Andersen and L. Botter-Jensen, "Influence of the stem effect on radioluminescence signals from optical fibre $\text{Al}_2\text{O}_3:\text{C}$ dosimeters," *Radiat Prot Dosimetry* **119**, 363-367 (2006).
76. W. E. Moloney, University of Florida, 2008.
77. D. Letourneau, J. Pouliot and R. Roy, "Miniature scintillating detector for small field radiation therapy," *Med Phys* **26**, 2555-2561 (1999).
78. L. B. Leybovich, A. Sethi and N. Dogan, "Comparison of ionization chambers of various volumes for IMRT absolute dose verification," *Med Phys* **30**, 119-123 (2003).

79. G. Bharanidharan, D. Manigandan, K. Devan, V. Subramani, N. Gopishankar, T. Ganesh, R. Joshi, G. Rath, J. Velmurugan, P. Aruna and S. Ganesan, "Characterization of responses and comparison of calibration factor for commercial MOSFET detectors," *Med Dosim* **30**, 213-218 (2005).
80. M. Soubra, J. Cygler and G. Mackay, "Evaluation of a dual bias dual metal oxide-silicon semiconductor field effect transistor detector as radiation dosimeter," *Med Phys* **21**, 567-572 (1994).
81. P. W. Hoban, M. Heydariyan, W. A. Beckham and A. H. Beddoe, "Dose rate dependence of a PTW diamond detector in the dosimetry of a 6 MV photon beam," *Phys Med Biol* **39**, 1219-1229 (1994).
82. B. Lee, K. W. Jang, D. H. Cho, W. J. Yoo, S. H. Shin, H. S. Kim, J. H. Yi, S. Kim, H. Cho, B. G. Park, J. H. Moon and S. Kim, "Measurement of two-dimensional photon beam distributions using a fiber-optic radiation sensor for small field radiation therapy," *IEEE Trans Nucl Sci* **55**, 2632-2636 (2008).
83. A. S. Beddar, T. J. Kinsella, A. Ikhlef and C. H. Sibata, "A miniature "scintillator-fiber-optic-PMT" detector system for the dosimetry of small fields in stereotactic radiosurgery," *IEEE Trans Nucl Sci* **48**, 924-928 (2001).
84. A. S. Beddar, T. R. Mackie and F. H. Attix, "Water-equivalent plastic scintillation detectors for high-energy beam dosimetry: I. Physical characteristics and theoretical consideration," *Phys Med Biol* **37**, 1883-1900 (1992).
85. A. S. Beddar, T. R. Mackie and F. H. Attix, "Water-equivalent plastic scintillation detectors for high-energy beam dosimetry: II. Properties and measurements," *Phys Med Biol* **37**, 1901-1913 (1992).
86. B. Lee, K. W. Jang, D. H. Cho, W. J. Yoo, S. H. Shin, G.-R. Tack, S.-C. Chung, S. Kim, H. Cho, B. G. Park, J. H. Moon and S. Kim, "Characterization of one-dimensional fiber-optic scintillating detectors for electron-beam therapy dosimetry," *IEEE Trans Nucl Sci* **55**, 2627-2631 (2008).
87. G. Bartesaghi, V. Conti, M. Prest, V. Mascagna, S. Scazzi, P. Cappelletti, M. Frigerio, S. Gelosa, A. Monti, A. Ostinelli, A. Mozzanica, R. Bevilacqua, G. Giannini, P. Totaro and E. Vallazza, "A scintillating fiber dosimeter for radiotherapy," *Nucl. Instrum. Methods Phys. Res. A* **A572**, 228-231 (2007).
88. J. M. Fontbonne, G. Iltis, G. Ban, A. Battala, J. C. Vernhes, J. Tillier, N. Bellaize, C. L. Brun, B. Tamain, K. Mercier and J. C. Motin, "Scintillating fiber dosimeter for radiation therapy accelerator," *IEEE Trans Nucl Sci* **49**, 2223-2227 (2002).
89. L. Archambault, A. S. Beddar, L. Gingras, F. Lacroix, R. Roy and L. Beaulieu, "Water-equivalent dosimeter array for small-field external beam radiotherapy," *Med Phys* **34**, 1583-1592 (2007).

90. A. S. Beddar, T. R. Mackie and F. H. Attix, "Cerenkov light generated in optical fibres and other light pipes irradiated by electron beams," *Phys Med Biol* **37**, 925-935 (1992).
91. L. Archambault, A. S. Beddar, L. Gingras, R. Roy and L. Beaulieu, "Measurement accuracy and cerenkov removal for high performance, high spatial resolution scintillation dosimetry," *Med Phys* **33**, 128-135 (2006).
92. A. M. Frelin, J. M. Fontbonne, G. Ban, J. Colin, M. Labalme, A. Batalla, A. Isambert, A. Vela and T. Leroux, "Spectral discrimination of Cerenkov radiation in scintillating dosimeters," *Med Phys* **32**, 3000-3006 (2005).
93. D. A. Jaffray, "Emergent technologies for 3-dimensional image-guided radiation delivery," *Semin Radiat Oncol* **15**, 208-216 (2005).
94. S. Kim, T. T. Yoshizumi, G. Toncheva, S. Yoo and F. F. Yin, "Comparison of radiation doses between cone beam CT and multi detector CT: TLD measurements," *Radiat Prot Dosimetry* **132**, 339-345 (2008).
95. C. Walter, J. Boda-Heggemann, H. Wertz, I. Loeb, A. Rahn, F. Lohr and F. Wenz, "Phantom and in-vivo measurements of dose exposure by image-guided radiotherapy (IGRT): MV portal images vs. kV portal images vs. cone-beam CT," *Radiother Oncol* **85**, 418-423 (2007).
96. J. R. Perks, J. Lehmann, A. M. Chen, C. C. Yang, R. L. Stern and J. A. Purdy, "Comparison of peripheral dose from image-guided radiation therapy (IGRT) using kV cone beam CT to intensity-modulated radiation therapy (IMRT)," *Radiother Oncol* **89**, 304-310 (2008).
97. L. J. Sawyer, S. A. Whittle, E. S. Matthews, H. C. Starritt and T. P. Jupp, "Estimation of organ and effective doses resulting from cone beam CT imaging for radiotherapy treatment planning," *Br J Radiol* **82**, 577-584 (2009).
98. J. R. Sykes, A. Amer, J. Czajka and C. J. Moore, "A feasibility study for image guided radiotherapy using low dose, high speed, cone beam X-ray volumetric imaging," *Radiother Oncol* **77**, 45-52 (2005).
99. J. Gu, B. Bednarz, X. G. Xu and S. B. Jiang, "Assessment of patient organ doses and effective doses using the VIP-Man adult male phantom for selected cone-beam CT imaging procedures during image guided radiation therapy," *Radiat Prot Dosimetry* **131**, 431-443 (2008).
100. P. S. Cho, R. H. Johnson and T. W. Griffin, "Cone-beam CT for radiotherapy applications," *Phys Med Biol* **40**, 1863-1883 (1995).
101. C. M. Ma, C. W. Coffey, L. A. DeWerd, C. Liu, R. Nath, S. M. Seltzer and J. P. Seuntjens, "AAPM protocol for 40-300 kV x-ray beam dosimetry in radiotherapy and radiobiology," *Med Phys* **28**, 868-893 (2001).

102. C. Kawaura, T. Aoyama, S. Koyama, M. Achiwa and M. Mori, "Organ and effective dose evaluation in diagnostic radiology based on in-phantom dose measurements with novel photodiode-dosimeters," *Radiat Prot Dosimetry* **118**, 421-430 (2006).
103. C. Lee, D. Lodwick, J. Hurtado, D. Pafundi and W. E. Bolch, "Development of a series of hybrid computational phantoms and their applications to assessment of photon and electron specific absorbed fractions," 2008 Annual Meeting of the European Association of Nuclear Medicine, Munich, Germany, October 11-15 (2008).
104. S. Seguchi, T. Aoyama, S. Koyama, C. Kawaura and K. Fujii, "Evaluation of exposure dose to patients undergoing catheter ablation procedures--a phantom study," *Eur Radiol* **18**, 2559-2567 (2008).
105. Joshua Levy - The Phantom Laboratory, (2009).
106. E. K. Osei, B. Schaly, A. Fleck, P. Charland and R. Barnett, "Dose assessment from an online kilovoltage imaging system in radiation therapy," *J Radiol Prot* **29**, 37-50 (2009).
107. ImPACT Group [www.impactscan.org/ctdosimetry], London, UK: St George's Hospital, (updated August 28, 2009; accessed September 15, 2009).
108. R. L. Dixon, "A new look at CT dose measurement: beyond CTDI," *Med Phys* **30**, 1272-1280 (2003).
109. R. L. Dixon and A. C. Ballard, "Experimental validation of a versatile system of CT dosimetry using a conventional ion chamber: beyond CTDI100," *Med Phys* **34**, 3399-3413 (2007).
110. S. Mori, M. Endo, K. Nishizawa, T. Tsunoo, T. Aoyama, H. Fujiwara and K. Murase, "Enlarged longitudinal dose profiles in cone-beam CT and the need for modified dosimetry," *Med Phys* **32**, 1061-1069 (2005).
111. D. E. Hyer, R. F. Fisher and D. E. Hintenlang, "Characterization of a water-equivalent fiber-optic coupled dosimeter for use in diagnostic radiology," *Med Phys* **36**, 1711-1716 (2009).
112. D. G. Jones and P. C. Shrimpton, "Normalised organ doses for X-ray computed tomography calculated using Monte Carlo techniques," Report No. SR250, Oxford: NRPB (1993).
113. M. Cristy, "Mathematical phantoms representing children of various ages for use in estimates of internal dose," Oak Ridge National Laboratory, ORNL/NUREG/TM-367 (1980).
114. R. Kramer and G. Drexler, "On the calculation of the effective dose equivalent," *Radiat Prot Dosimetry* **3**, 13-24 (1982).

115. R. Kramer, H. J. Khoury and J. W. Vieira, "Comparison between effective doses for voxel-based and stylized exposure models from photon and electron irradiation," *Phys Med Biol* **50**, 5105-5126 (2005).
116. C. Lee and W. E. Bolch, "Age-dependent organ and effective dose coefficients for external photons: a comparison of stylized and voxel-based paediatric phantoms," *Phys Med Biol* **51**, 4663-4688 (2006).
117. P. B. Johnson, S. R. Whalen, M. Wayson, B. Juneja, C. Lee and W. E. Bolch, "Hybrid patient-dependent phantoms covering statistical distributions of body morphometry in the U.S. adult and pediatric population," *Proc. of the IEEE* **97**, 2060-2075 (2009).
118. D. E. Hyer, C. F. Serago, S. Kim, J. G. Li and D. E. Hintenlang, "An organ and effective dose study of XVI and OBI cone-beam CT systems," *J Appl Clin Med Phys* (2010). *In Press*

BIOGRAPHICAL SKETCH

Daniel Ellis Hyer was born in Westlake, Ohio to John and Dee Hyer. He is one of two children, along with his brother, John. He attended high school in Madison, Ohio, at Madison High School. He then went on to college at the Georgia Institute of Technology, earning his bachelor's degree in mechanical engineering in 2006, summa cum laude, and his master's degree in medical physics in 2007. With an interest in performing research in medical physics, Dan continued his studies at the University of Florida, where he earned his doctorate in nuclear engineering sciences in 2010.